UNIVERSITÁ DEGLI STUDI DI PADOVA

DIPARTIMENTO DI FISICA E ASTRONOMIA GALILEO GALILEI

Corso di Laurea Magistrale in Fisica

Quantum dot/enzyme bioconjugation and investigation of optoelectronic properties

RELATORE: Prof. Filippo Romanato
CORRELATORI: Prof. Carmen Bartic
Dr. Olivier Deshaume

LAUREANDO: Andrea Bertolucci

---

7 ottobre 2014

Contents

Introduction

Glucose is the major energy source in cellular metabolism and it plays an important role in the natural growth of cells. Glucose deficiency or excess can produce detrimental influence on cellular functions.

The glucose level in blood is usually used as a clinical indicator of diabetes. A rapid and accurate determination of glucose in human blood and urine is therefore essential in the diagnosis and management of diabetes, which is affecting about 150 million people in the world. Millions of diabetics need to test their blood glucose levels daily, making glucose the most commonly tested analyte. Moreover, determination of glucose concentration takes a relevant place in controlling various food and biotechnological processes.

It is thus necessary to a find fast, precise and cheap methods to estimate glucose concentration in human serum.

New techniques developed in the last decades involve metal and semiconductors nanoparticles as direct sensors for organic molecules, avoiding indirect sensing mediated through chemicals assays.

In particular semiconductor nanoparticles, also known as quantum dots (QDs), have attracted great interest in both fundamental researches and technical applications. They are tiny crystalline particles that exhibit size-dependent optical and electronic properties. Thanks to their typical dimensions in the range of 1-100 nm, these nanocrystals bridge the gap between small molecules and large crystals, displaying discrete electronic transitions reminiscent of isolated atoms and molecules.

Moreover, quantum dots are emerging as a new class of fluorescent agent for biological imaging and bioanalysis applications, thanks to emerging properties like multicolor emission with a single light source and a higher emission quantum yield and higher resistance to photobleaching compared with organic dyes. Therefore they have been used for staining fixed and living cells, and for imaging living animals. The QDs probes used today are photostable, bright, and size-tunable, and they are the culmination of a series of technological advances in chemistry and colloid science since 1993, when Bawendi and coworkers reported the first synthesis of highly monodisperse, crystalline cadmium selenide nanoparticles in a hot coordinating solvent.

On the other hand, enzymes are an important type of bio-macromolecules with high catalytic efficiency and high substrate-specificity and they play a prominent role in biological systems. Glucose oxidase (GOx) is an enzyme most commonly used with glucose, due to its high specificity for that type of sugar molecule. It has been widely employed for the optical and electrochemical determination of glucose. However, as well as many other type of enzymes, GOx suffers of instability and it is easily denaturable. Therefore research on the improvement of enzymatic properties of GOx, including activity, stability, and active temperature range, has attracted increasing attention.

Since bio-macromolecules exhibit nanoscale dimensions comparable to the dimensions of metal or semiconductor nanoparticles, it is particularly interesting to combine the unique electronic, photonic, and catalytic properties of NPs with the nature-evolved selective binding and catalytic functions of biomolecules , leading to hybrid systems where the native and the synthetic components are integrated. Such hybrids may reveal new material functions: the QDs may introduce new electronic, photonic or optoelectronic properties into the biomolecules, or, alternatively, the biomolecules may affect the structure or the properties of the QDs.

Moreover, the increased surface area of the nanoparticles can provide a better matrix for the immobilization of enzymes, and this could lead to the immobilization of a larger amount of enzymes on the particles. The multipoint combination of the enzyme molecules onto the nanoparticle surfaces can improve the enzyme-substrate interaction effectively by avoiding the eventual aggregation of free enzymes, which would lead to an enhancement of the enzymatic activity. In addition, enzymes attached on nanomaterial surfaces can reduce protein unfolding and turbulence, and thus ensure the enhanced stability of the enzymes in the solution.

By taking advantage of the unique optical features of QDs and the efficient and specific bioreactions, QDs-biomolecules hybrid systems have a great potential in the determination of specific analytes. In the past few years, extensive research efforts were directed towards the development of these hybrid assemblies and their application to construct biosensors, nanoscale circuitry or nanodevices.

More specifically, in this project we will focus on how the enzyme influences nanoparticles (NPs) photoluminescence. In order to achieve the desired results, the following steps are required.

First NPs-enzyme hybrid system will be synthesized, accordingly to protocols reported in literature. Two different functionalizations and two different types of particles will be used. The goal is to understand their global properties, as well as how these properties change when different parameters that can affect the measurements are changed.

After that, the products will be optically characterized through absorbance and fluorescence analysis. To test the behavior of conjugated system with active enzymes, fluorescence measurements of particles mixed in glucose solution will be acquired. The analyzed results will be compared with the state-of-the-art results reported in literature, and a comprehensive explanation of all phenomena involved will be finally proposed.

This thesis work was carried within the framework of Erasmus project at Katholieke Universiteit Leuven, under the supervision of prof. Carmen Bartic, prof. Margriet Van Bael and Dr. Olivier Deschaume.

Chapter 1

Excitons in solids

The optical properties of matter results from the quantum transitions electrons perform in the course of light-matter interactions. This chapter contains an introduction to the electron properties in solids in terms of quantum particles in a periodic potential, the concept of quasiparticles and the band structure.

1.1 Bloch waves

Consider a one-dimensional Schrödinger equation for a particle with mass m,

$$-\frac{\hbar^2}{2m}\frac{d^2}{dx^2}\psi_k(x) + U(x)\psi_k(x) = E\psi_k(x) \tag{1.1.1}$$

with a periodic potential,

$$U(x) = U(x + na) \tag{1.1.2}$$

where n is an integer number. Thus we have translational symmetry of potential, i.e. invariance of U with respect to coordinate shift over an integer number of periods.

To give a primary insight into the properties of wave functions satisfying the Schrödinger equation with a periodic potential, consider the replacement, $x \to x + a$. Then we arrive at equation,

$$-\frac{\hbar^2}{2m}\frac{d^2}{dx^2}\psi_k(x + a) + U(x)\psi_k(x + a) = E\psi_k(x + a), \tag{1.1.3}$$

where periodicity of the potential (1.1.2) has been implied.

One can see that $\psi(x)$ and $\psi(x + a)$ do satisfy the same second-order differential equation. This means that either $\psi(x)$ is periodic, or at least it differs from a periodic function by a complex coefficient whose square of modulus equals 1. The solution of Eq. (1.1.1) with a periodic potential is

$$\psi_k(x) = e^{ikx}u_k(x), u_k(x) = u_k(x + a), \tag{1.1.4}$$

i.e. the wave function is a plane wave e^{ikx} with amplitude modulated in accordance with the periodicity of the potential $U(x)$. The k subscript for u_k means the function u_k is different for different wavenumbers. An important property of the wave function (1.1.4) is its periodicity with respect to wave number. In fact, substituting $x \to x + a$ and $k \to k + 2\pi/a$ returns $\psi(x)$ to its original value.

In a three-dimensional case the periodic potential is

$$U(\overline{r}) = U(\overline{r} + \overline{T}), \tag{1.1.5}$$

where $\overline{T} = n_1\overline{a_1} + n_2\overline{a_2} + n_3\overline{a_3}$ is a translation vector, and $\overline{a_i}$ are elementary translation vector defined a

$$\overline{a_1} = a_1\hat{i},\ \overline{a_2} = a_2\hat{j},\ \overline{a_3} = a_3\hat{k},$$

with a_1, a_2, a_3 being the periods and $\hat{i}, \hat{j}, \hat{k}$ the unit vectors in the x, y, z directions respectively. The solution of a three-dimensional Schrödingier equation

$$-\frac{\hbar^2}{2m}\nabla^2\psi_{\overline{k}}(\overline{r}) + U(\overline{r})\psi_{\overline{k}}(\overline{r}) = E\psi_{\overline{k}}(\overline{r}) \tag{1.1.6}$$

in the case of a periodic potential has the form

$$\psi_{\overline{k}}(\overline{r}) = e^{i\overline{k}\cdot\overline{r}}u_k(\overline{r}),\ u_k(\overline{r}) = u_k(\overline{r} + \overline{T}). \tag{1.1.7}$$

This statement is known as Bloch theorem and addresses the properties of the Schrödingier equation for electrons in a crystal lattice. Therefore solutions for equations (1.1.4) and (1.1.7) are known as Bloch waves.

1.1.1 One-dimensional Bloch waves

Periodicity of $u_k(x)$ in the Bloch function (1.1.4) along with the periodicity of the phase coefficient e^{ikx} with respect to kx with period 2π makes wave numbers differing in integer number $2\pi/a$, i.e.

$$k_1 - k_2 = \frac{2\pi}{a}n,\ n = \pm1, \pm2, \pm3, ..., \tag{1.1.8}$$

appear to be equivalent. This is a direct consequence of the translational symmetry of the space. Therefore, the whole multitude of k values consists of equivalent intervals each with width $2\pi/a$. Every interval contains the full set of nonequivalent k values and is called the Brillouin zone. The energy spectrum and the dispersion curve differ from those of a free particle (Fig. 1.1). The dispersion curve has discontinuities at points

$$k_n = \frac{\pi}{a}n;\ n = \pm1, \pm2, \pm3, ...\tag{1.1.9}$$

At these k values the wave function is a standing wave which arises due to multiple reflections from the periodic structure. For every k_n satisfying Eqs. (1.1.11), two standing waves exist with different potential energies. This leads to the emergence of forbidden energy intervals for which no propagating wave exists. Because of these discontinuities it is convenient to consider Brillouin zones starting from the first one around $k = 0$, i.e.

$$-\frac{\pi}{a} < k < \frac{\pi}{a}. \tag{1.1.10}$$

Because of the equivalence of wave numbers differing in integer number of $2\pi/a$ it is possible to move all branches of the dispersion curve towards the first Brillouin zone by means of a shift along the k-axis by the integer number $2\pi/a$. Therefore, the original dispersion curve (Fig. 1.1(a)) can be modified to yield the reduced zone scheme (Fig. 1.1b). The whole wealth of particle dynamics in a periodic potential can be treated in terms of events within the first Brillouin zone, the energy being a multivalue function

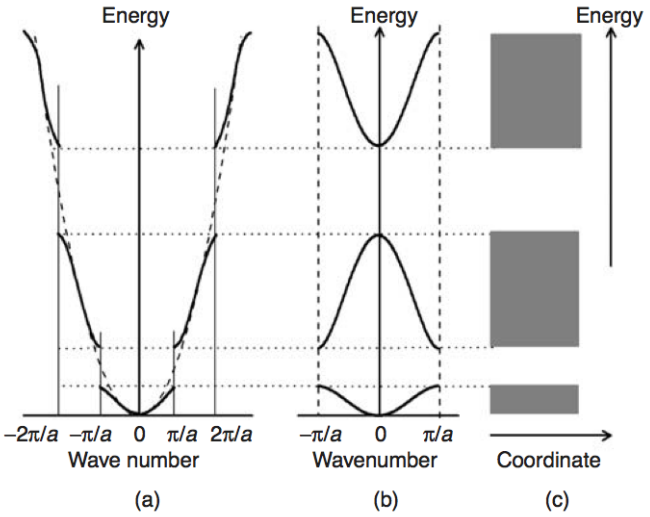

Figure 1.1: Original (a) and reduced (b) representation of the dispersion law of a particle in a one-dimensional periodic potential, and the corresponding energy bands in space (c). The dashed line in (a) is the parabolic dispersion law for a particle in free space [1]

of the wave number. Representation of the dispersion law in Fig. 1.1(b) is referred to as the band structure.

The value,

$$p = \hbar k \tag{1.1.11}$$

is called the *quasi-momentum*. It differs from the momentum by a specific conservation law. It conserves with an accuracy of $2\pi\hbar/a$, which is, again, a direct consequence of the translational symmetry of space.

The relation 1.1.11 gives rise to Brillouin zones for momentum. For Figure 1.1(b) the first Brillouin zone for momentum is the interval

$$-\hbar\frac{\pi}{a} < p < \hbar\frac{\pi}{a}.$$

Standing waves at points in Eq. 1.1.9 result in zero values of the derivative

$$\left.\frac{dE(p)}{dp(k)}\right|_{k_n} = 0, \tag{1.1.12}$$

i.e. in the center and at the edges of the first Brillouin zone. Therefore the expansion of the $E(k)$ function near a given extremum point $E_0(k_0)$,

$$E(k) = E(0) + (k-k_0)\left.\frac{dE}{dk}\right|_{k=k_0} + \frac{1}{2}(k-k_0)^2\left.\frac{d^2E}{dk^2}\right|_{k=k_0} + ... \tag{1.1.13}$$

can be reduced to a parabolic $E(k)$ law

$$E(k) = \frac{1}{2}k^2\left.\frac{d^2E}{dk^2}\right|_{k=k_0} \tag{1.1.14}$$

by putting $E_0 = 0$, $k_0 = 0$ and omitting the higher-order derivatives in the law. In turn, the parabolic dispersion law means that the effective mass of the particle under consideration can formally be introduced in the vicinity of every extremum of $E(k)$ as

$$\frac{1}{m^*} = \frac{1}{\hbar^2}\frac{d^2E}{dk^2} \equiv \frac{d^2E}{dp^2} = const. \tag{1.1.15}$$

From the relation $E = p^2/2m = \hbar^2k^2/2m$, for a free particle we have everywhere

$$\frac{1}{\hbar^2}\frac{d^2E}{dk^2} = \frac{d^2E}{dp^2} \equiv m^{-1}.$$

The effective mass (1.1.15) determines the reaction of a particle to the external force, $\overline{F}$, via a relation

$$m^*\overline{a} = \overline{F} \tag{1.1.16}$$

where $\overline{a}$ is the acceleration. Equation 1.1.16 coincides formally with Newton's second law. In the vicinity of every extremum, the Schrödinger equation with periodic potential 1.1.1 reduces to the equation

$$-\frac{\hbar^2}{2m^*}\frac{d^2\psi_k(x)}{dx^2} = E\psi_k(x) \tag{1.1.17}$$

which describes the free motion of a particle with effective rather than original mass.

Summarizing the properties of a particle in a periodic potential:

- ◇ A particle is described by a plane wave modulated by a period of the potential;
- ◇ The particle state is characterized by the quasi-momentum. The latter has a set of equivalent intervals, the Brillouin zones, each containing the complete multitude of non-equivalent values;
- ◇ The energy spectrum consists of wide continuous bands separated from each other by forbidden gaps. As a plane wave, a particle in a periodic potential exhibits quasi-free motion without an acceleration. With respect to the external force, the particle's behavior is described in terms of the effective mass. The latter is, basically, a complicated function of energy, but can be considered a constant in the vicinity of a given extremum of the E(k) curve. Generally, the renormalization of mass is nothing else but a result of the interaction of a particle with a given type of periodic potential.

1.2 Density of states

Considering an electron confined in a cube of edge L with Schrödinger equation

$$-\frac{\hbar^2}{2m}\left(\frac{\partial^2}{dx^2} + \frac{\partial^2}{dy^2} + \frac{\partial^2}{dz^2}\right)\psi_k(\overline{r}) = E\psi_{\overline{k}}(\overline{r}). \tag{1.2.1}$$

As seen for electron in a periodic potential, wave functions that satisfy periodic boundary condition

$$\psi(x + L, y, z) = \psi(x, y, z) \tag{1.2.2}$$

and similarly for y and z coordinates, are of the form of a traveling plane wave:

$$\psi_{\overline{k}}(\overline{r}) = e^{i\overline{k}\cdot\overline{r}} \tag{1.2.3}$$

with component of the wavevector $\overline{k}$ satisfying

$$k_x = \pm n_x \frac{2\pi}{L},\ n_x = 0, 1, 2, ... \tag{1.2.4}$$

and similarly for k_y and k_z.

Substituting (1.2.3) in (1.2.1) we have the energy $E_{\overline{k}}$ of the orbital with wavevector $\overline{k}$

$$E_{\overline{k}} = \frac{\hbar^2}{2m}\overline{k}^2 = \frac{\hbar^2}{2m}(k_x^2 + k_y^2 + k_z^2). \tag{1.2.5}$$

In the ground state of a system on N free electrons, the occupied orbitals may be represented as points inside a sphere in $\overline{k}$ space. The energy at the surface of the sphere is the Fermi energy; the wave vectors at the Fermi surface have a magnitude k_F such that:

$$E_F = \frac{\hbar^2}{2m}k_F^2 \tag{1.2.6}$$

From (1.2.4) we see that there is one allowed wavevector (one every distinct triplet of quantum numbers k_x, k_y and k_z) for the volume element $(2\pi/L)^3$ of $\overline{k}$ space. Thus in the sphere of volume $4\pi k_F^3/3$ the total number of orbitals is

$$N = 2\frac{4\pi k_F^3/3}{(2\pi/L)^3} = \frac{V}{3\pi^2}k_F^3 \tag{1.2.7}$$

where the factor 2 comes from the two allowed values of the spin for each allowed value of $\overline{k}$. Then (1.2.7) gives

$$k_F = \left(\frac{3\pi^2 N}{V}\right)^{1/3} \tag{1.2.8}$$

which depends only on the particle concentration.

Using (1.2.6) and (1.2.8)

$$E_F = \frac{\hbar^2}{2m}\left(\frac{2\pi^2 N}{V}\right)^{2/3}. \tag{1.2.9}$$

We now derive a new quantity called *density of states* from the total number of orbitals of energy $\leq E$:

$$N = \frac{V}{3\pi^2}\left(\frac{2mE}{\hbar^2}\right)^{3/2} \tag{1.2.10}$$

so that the density of state (Fig. 1.2) is

$$D(E) \equiv \frac{dN}{dE} = \frac{V}{2\pi^2}\left(\frac{2m}{\hbar^2}\right)^{3/2} E^{1/2} \tag{1.2.11}$$

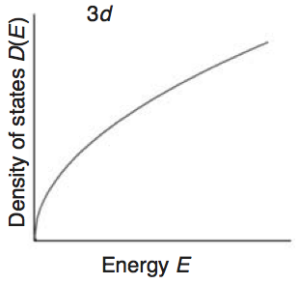

Figure 1.2: Free electron density of state for a 3d system [2]

1.3 Electron band structure in solids

The dispersion law for the first Brillouin zone of a particle in a periodic potential shown in Figure 1.1 provides an idea of the band structure for a hypothetical one-dimensional crystal. The electronic properties of solids are determined by occupation of the bands and by the absolute values of the forbidden gap between the completely occupied and the partly unoccupied, or free bands. If a crystal has a partly occupied band, it exhibits metallic properties, because electrons in this band provide electrical conductivity. If all the bands at $T = 0$ are either occupied or completely free, the material will show dielectric properties. Electrons within the occupied band cannot provide any conductivity because of Pauli's exclusion principle: only one electron may occupy any given state. Therefore, under an external field an electron in the completely occupied band cannot change its energy because all neighboring states are already filled. The highest occupied band is usually referred to as the *valence band* and the lowest unoccupied band is called the *conduction band*. The difference between the top of the valence band, E_v, and the bottom of the conduction band, E_c, is called the band gap energy, E_g:

$$E_g = E_c - E_v \tag{1.3.1}$$

Depending on the absolute E_g value, solids that show dielectric properties (i.e., zero conductivity) at $T = 0$, are classified into dielectrics and semiconductors. If E_g is less than 3-4 eV, the conduction band has a non-negligible population at elevated temperatures, and these types of solids are called *semiconductors*. The band structures of the two representative semiconductors, cadmium sulfide and silicon, are given in Figure 1.3. For CdS crystals the minimal gap between E_c and E_v occurs at the same k value. Crystals of this type are called *direct-gap semiconductors*. For the Si crystal, the minimal energy gap corresponds to the different k values for E_c and E_v. These types of crystals are usually referred to as *indirect-gap semiconductors*.

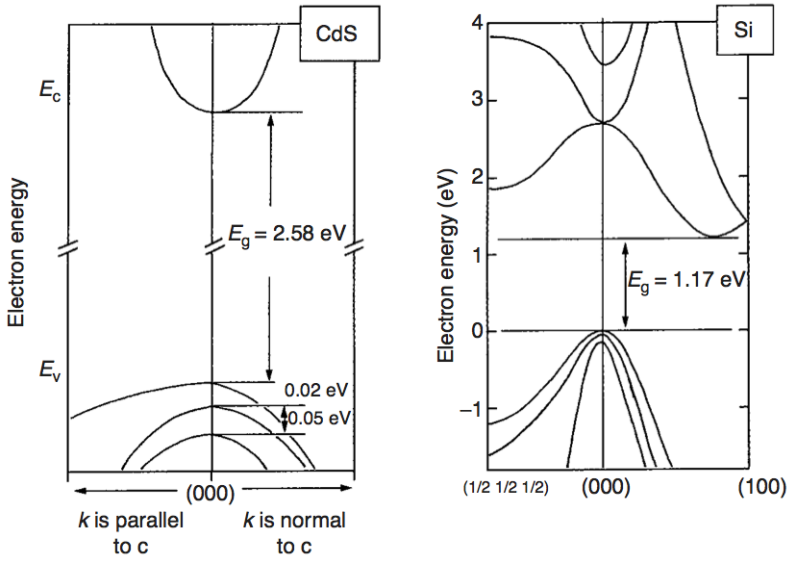

Figure 1.3: Band structures of two representative semiconductors, CdS and Si. In CdS the top of the valence band and the bottom of the conduction band correspond to the same wave number, i.e., CdS is a *direct-gap* semiconductor. In Si the extrema of the conduction and the valence band correspond to the different wave numbers, i.e. Si is an *indirect-gap* semiconductor. [3]

1.4 Excitons

When speaking about an electron in the conduction band, one implies a particle whose properties result from interactions in a many-body system consisting of a large number of positive nuclei and negative electrons. It is the standard approach to replace consideration of the large number of interacting particles by the small number of non-interacting quasiparticles. These quasiparticles are described as elementary excitations of the system consisting of a number of real particles. An electron in the conduction band is the primary elementary excitation of the electron subsystem of a crystal. The further elementary excitation is a *hole*, which is a quasiparticle relevant to an ensemble of electrons in the valence band from which one electron is removed. This excitation is characterized by the positive charge $+e$, spin $1/2$, effective mass m_h^*, and the quasi-momentum. In this representation, the kinetic energy of the hole has an opposite sign compared to that of the electron kinetic energy.

Using concepts of elementary excitation, we can consider the ground state of a crystal as a vacuum state (neither an electron in the conduction band nor a hole in the valence band exists), and the first excited state (one electron in the conduction band and one hole in the valence band) in terms of creation of one electron-hole-pair (e-h-pair). A transition from the ground to the first excited state occurs due to photon absorption with energy and momentum conservation

$$\begin{aligned} \hbar\omega &= E_g + E_{e,kin} + E_{h,kin} \\ \hbar\overline{k_\gamma} &= \hbar\overline{k_e} + \hbar\overline{k_h} \end{aligned} \tag{1.4.1}$$

Here $E_{e,kin}$ ($E_{h,kin}$) and $\overline{k_e}$ ($\overline{k_h}$) are electron (hole) kinetic energy and wave vector, respectively. The reverse process, i.e., a downward radiative transition which is equivalent to annihilation of an e-h-pair and creation of a photon is possible as well. These

Crystals of group IV elements			Crystals of III-V compounds		
Crystal	Band gap energy E_g	λ of light equivalent to E_g	Crystal	Band gap energy E_g	λ of light equivalent to E_g
Si*	1.14 eV	1.1 μm	GaN	3.50 eV	354 nm
Ge*	0.67 eV	1.85 μm	GaP*	2.26 eV	550 nm
			GaAs	1.43 eV	870 nm
			InAs	0.42 eV	2.95 μm
			InSb	0.18 eV	6.9 μm
Crystals of II-VI compounds			Crystals of I-VII compounds		
Crystal	Band gap energy E_g	λ of light equivalent to E_g	Crystal	Band gap energy E_g	λ of light equivalent to E_g
ZnS	3.68 eV	337 nm	LiF	12 eV	100 nm
ZnSe	2.80 eV	440 nm	NaCl	>4eV	<300 nm
ZnTe	2.25 eV	550 nm	CuCl	3.2 eV	390 nm
CdS	2.58 eV	480nm	CuBr	2.9 eV	420 nm
CdSe	1.84 eV	670 nm	Crystals of IV-VI compounds		
CdTe	1.6 eV	770 nm	PbS	0.41 eV	3.0 μm
HgTe	0.15 eV	8.2 μm	PbSe	0.28 eV	4.4 μm
* Indirect-gap materials					

Table 1.1: Band gap energy and relevant wavelength for semiconductor and dielectric crystals [4].

events and concepts have a lot in common with real vacuum, electrons and positrons. The only difference is that the positron mass is exactly equal to the electron mass m_0, whereas in a crystal the hole effective mass m_h^* is usually larger than the electron mass m_e^*.

The band gap energy corresponds to the minimal energy which is sufficient for the creation of one pair of free charge carriers, i.e., electron and hole. This statement can serve as the definition of E_g.

Electrons and holes as charged particles interact via Coulomb potential and form an extra quasiparticle, which corresponds to the hydrogen-like bound state of an electron-hole pair and denoted as *exciton*. Interacting holes and electrons can be described by a Hamiltonian

$$H = -\frac{\hbar^2}{2m_e^*}\nabla_e^2 - \frac{\hbar^2}{2m_h^*}\nabla_h^2 + \frac{e^2}{\epsilon|\overline{r_e} - \overline{r_h}|}. \tag{1.4.2}$$

This is the same as the Hamiltonian of the hydrogen atom with m_e^* and m_h^* instead of a free electron mass m_0 and a proton mass $m_p = 1836m_0$, respectively and with the dielectric constant of the crystal $\epsilon > 1$. Therefore, similarly to the hydrogen atom, an exciton is characterized by the exciton Bohr radius

$$a_B^* = 4\pi\epsilon_0\frac{\epsilon\hbar^2}{\mu_{eh}e^2} = \epsilon\frac{\mu_H}{\mu_{eh}} \times 0.053\,nm \approx \epsilon\frac{m_0}{\mu_{eh}} \times 0.053\,nm \tag{1.4.3}$$

where μ_H is the electron-proton reduced mass defined as

	Exciton Rydberg $Ry^*(meV)$	Electron effective $mass m_e/m_0$	Hole effective $mass m_h/m_0$	Exciton Bohr $radius a_B^*(nm)$
Ge	4.1	$\perp$ 0.19	0.54(hh)	24.3
		$\parallel$ 0.92	0.15(lh)	
Si	15	$\perp$ 0.081	0.3(hh)	4.3
		$\parallel$ 1.6	0.043(lh)	
GaAs	4.6	0.066	0.47(hh)	12.5
			0.07(lh)	
CdTe	10	0.1	0.4	7.5
CdSe	16	0.13	$\perp$ 0.45	4.9
			$\parallel$ 1.1	
CdS	29	0.14	$\perp$ 0.7	42.8
			$\parallel$ 2.5	
ZnSe	19	0.15	0.8(hh)	3.8
			0.145(lh)	
CuBr	108	0.25	1.4(hh)	1.2
CuCl	190	0.4	2.4(hh)	0.7
GaN	28	0.17	0.3(hh)	2.1
			0.14(lh)	
PbS	2.3	$\perp$ 0.080	$\perp$ 0.075	18
		$\parallel$ 0.105	$\parallel$ 0.105	
PbSe	2.05	$\perp$ 0.040	$\perp$ 0.034	46
		$\parallel$ 0.070	$\parallel$ 0.068	

Table 1.2: Electron, hole and exciton parameters; hh and lh stand for heavy and light hole respectively; $\perp(\parallel)$ means traverse (longitudinal) values [4].

$$\mu_H^{-1} = m_0^{-1} + m_{proton}^{-1} \approx m_0^{-1} \tag{1.4.4}$$

which to great accuracy equals the electron mass m_0 because $m_0 \ll m_{proton}$, and μ_{eh} is the electron-hole reduced mass

$$\mu_{eh}^{-1} = m_e^{*-1} + m_h^{*-1}. \tag{1.4.5}$$

Also, similarly to a hydrogen atom, the exciton Rydberg energy can be written as

$$Ry^* = \frac{e^2}{2\epsilon a_B^*} = \frac{1}{4\pi\epsilon_0}\frac{\mu_{eh}}{\mu_H}\frac{1}{\epsilon^2} \times 13.60\,eV \approx \frac{\mu_{eh}}{m_0}\frac{1}{\epsilon^2} \times 13.60\,eV. \tag{1.4.6}$$

The reduced electron-hole mass is smaller than the electron mass m_0, and the dielectric constant ϵ is several times larger than that of a vacuum. This is why the exciton Bohr radius is significantly larger and the exciton Rydberg energy is significantly smaller than the relevant values for the hydrogen atom ($a_B = 0.053\,nm$, $Ry = 27.2\,eV$).

An exciton exhibits the translational center-of-mass motion as a single uncharged particle with mass $M = m_e^* + m_h^*$. The dispersion relation can be expressed as

$$E_n(\overline{K}) = E_g - \frac{Ry^*}{n^2} + \frac{\hbar^2\overline{K}^2}{2M},\ n = 1, 2, 3, ... \tag{1.4.7}$$

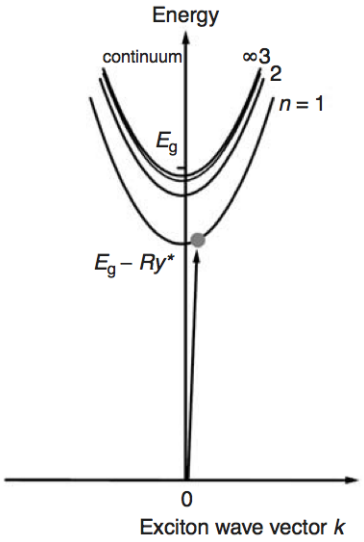

Figure 1.4: Dispersion curves of an exciton and the optical transition corresponding to photon absorption and exciton creation. Dispersion curves correspond to the hydrogen-like set of energies $E_n = E_g - Ry^*/n^2$ at $k = 0$ and a parabolic $E(k)$ dependence for every E_n, describing the translational center-of mass motion. For $E > E_g$, the exciton spectrum overlaps with the continuum of unbound electron-hole states. Exciton creation can be presented as intersection of the exciton and the photon dispersion curves corresponding to simultaneous energy and momentum conservation. The photon dispersion curve is a straight line in agreement with the formula $E = pc$ [1].

where $\overline{K}$ is the exciton wave vector. Equation (1.4.7) includes the hydrogen-like set of energy levels, the kinetic energy of the translational motion and the band gap energy. The exciton energy spectrum consists of subbands (Fig. 1.4) which converge to the dissociation edge corresponding to the free electron-hole-pair. Similarly to the free e-h-pair, an exciton can be created by photon absorption. Taking into account that a photon has a negligibly small momentum, exciton creation corresponds to a discrete set of energies

$$E_n = E_g - \frac{Ry^*}{n^2},\ n = 1, 2, 3, ... \tag{1.4.8}$$

An exciton gas can be described as a gas of bosons with an energy distribution function obeying the Bose-Einstein statistics, i.e. there is no limit to the number of excitons occupying a single state. For a given temperature T, the concentration of excitons n_{exc} and of the free electrons and holes $n = n_e = n_h$, are related via the ionization equilibrium equation known as the Saha equation:

$$n_{exc} = n^2 \left(\frac{2\pi\hbar}{k_B T} \frac{1}{\mu_{eh}} \right)^{3/2} e^{\frac{Ry^*}{k_B t}} \tag{1.4.9}$$

For $k_B T \gg Ry^*$ most of the excitons are ionized and the properties of the electron subsystem of the crystal are determined by the gas of free electrons and holes. At $k_B T \leq Ry^*$ a significant number of electron-hole-pairs exist in the bound state. As a result of creation of excitons and free electron-hole-pairs, the absorption spectrum of direct-gap semiconductor monocrystals contains a pronounced resonance peak at energy $\hbar\omega = E_g - Ry^*$, a set of smaller peaks at energies E_n (1.4.8), and a smooth

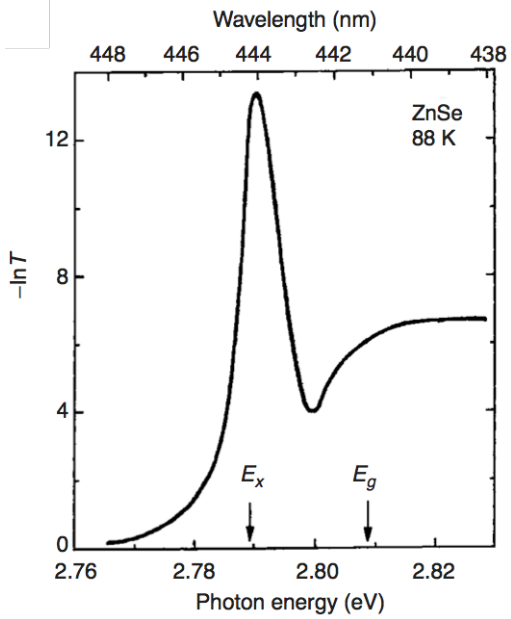

Figure 1.5: Absorption spectrum of a ZnSe single crystal near the fundamental absorption edge at a temperature equal to 88 K. Zinc selenide possesses band-gap energy $E_g = 2.809\,eV$ at $T = 80K$ and exciton Rydberg energy $Ry^* = 18\,meV$. At $k_BT \gg Ry^*$ the spectrum contains a pronounced peak for exciton adsorption corresponding to $n = 1$, whereas the higher sub-bands are smeared due to thermal broadening. At $k_BT > Ry^*$ the exciton band is not pronounced, however enhancement of absorption at $\hbar\omega < E_g$ due to electron-hole Coulomb interaction occurs. [1]

continuous absorption for $\hbar\omega \geqslant E_g$. For $\hbar\omega \geqslant E_g$ the absorption coefficient increases monotonically, the dependence of absorption coefficient versus frequency following the density of states dependence $D(E) = const\sqrt{E - E_g}$ as a first approximation. In reality, absorption is enhanced because of the electron-hole Coulomb interaction.

1.5 Quantum confinement effects in solids

Considering the de Broglie wavelength for electron $\lambda_e = h/\sqrt{2mE}$, assuming the effective mass inherent in real crystals and using the room temperature $k_BT = 26.7\,meV$ value as measure for the electron kinetic energy we obtain

$$\lambda_e = \frac{h}{\sqrt{2m_e^* k_B T}} \tag{1.5.1}$$

For an electron in a vacuum Eq. (1.5.1) gives $\lambda_e = 7.3\,nm$. For an electron in various materials the λ_e values are given in Table 1.3, along with the lattice constants a_L for the same crystals. One can see λ_e is more than one order of magnitude bigger than a_L. Therefore it is possible to perform spatial confinement of an electron (as well as hole and exciton) motion in one, two or all three directions while keeping the crystal lattice structure non-perturbed or rather slightly perturbed.

In a thin film whose thickness is less than the electron de Broglie wavelength the electron motion will be confined in the direction normal to the film plane, remaining infinite in the other two dimensions. Such a film is referred to as a *quantum well*. The motion of quasiparticles can also be confined in two directions if a crystal has a

Material	Electron mass	λ_e (nm)	a_L (nm)
SiC	0.41 m_0	11	0.308
Si	0.08 m_0	26	0.543
GaAs	0.067 m_0	28	0.564
Ge	0.19 m_0	16	0.564
ZnSe	0.15 m_0	19	0.567
InSb	0.014 m_0	62	0.647
CdTe	0.1 m_0	23	0.647
In vacuum	m_0	7.3	

Table 1.3: Lattice constants and electron de Broglie wavelength at room temperature for different semiconductor crystals

needle-like or rod-like shape with cross-sectional size smaller than λ_e. These are usually referred to as *quantum wires*. Finally, crystalline nanoparticles (nanocrystals) can offer confinement for electron motion in all three directions provided that their size is no more than a few nanometers. These are referred to as *quantum dots*.

For a cubic quantum dot with infinite potential barriers only a discrete set of completely localized states is allowed. The wave function is

$$\psi(\overline{r}) = 2\sqrt{\frac{2}{L_x L_y L_z}} sin(k_n^{(x)} x) sin(k_m^{(y)} y) sin(k_l^{(z)} z),\ n, m, l = 1, 2, 3, ... \tag{1.5.2}$$

The energy spectrum of an electron in a cubic box with $L_x = L_y = L_z = L$ is

$$E = \frac{\pi^2 \hbar^2}{2 m_e^* L^2}(n^2 + m^2 + l^2),\ n.m.l = 1, 2, 3, ... \tag{1.5.3}$$

Chapter 2

Quantum dots

In nanocrystals, the translational symmetry is totally broken and only a finite number of electrons and holes can be created within the same nanocrystal. Therefore, the concepts of the electron-hole gas and quasi-momentum fail in nanocrystals.

From the viewpoint of molecular physics, nanocrystals can be considered as a kind of large molecule. Similarly to molecular ensembles, nanocrystals dispersed in a transparent host environment (liquid or solid) exhibit a variety of guest-host phenomena known for molecular structures. Moreover, every nanocrystal ensemble has broadened absorption and emission spectra due to distribution of sizes, defect concentration, shape fluctuations, environmental inhomogeneities and other features.

Description of semiconductor nanocrystals and their optical properties is related to the size ranges of the particle which lead to different models and theoretical approach. The characteristic parameters involved in such a classification are the crystal lattice constant, a_L, the exciton Bohr radius, a_B^*, and the photon wavelength λ corresponding to the lowest optical transition.

If the size a of a nanocrystal is comparable to a_L, i.e. close to 1 nm, an adequate description can be provided only in terms of the quantum-chemical (molecular) approach with the specific number of atoms and configuration taken into account. This size interval can be classified as a *cluster range*. The main distinctive feature of clusters is the absence of a monotonic dependence of the optical transition energies and probabilities versus number of atoms. The size as a characteristic of clusters is by no means justified.

In the case when $a_L \ll a \ll \lambda$ a nanocrystal can be treated as a quantum box for electron excitations. The solid-state approach in terms of the effective mass approximation predicts a monotonic evolution of the optical properties of nanocrystals with size towards the properties of the parent bulk single crystals. The exciton Bohr radius value, a_B^* , divides this range into two subranges, $a \ll a_B^*$ and $a \gg a_B^*$, providing an interpretation of size-dependent properties in terms of either electron and hole, or a hydrogen-like exciton confined motion. This range can be classified as the *quantum dot range*.

As the size of a nanocrystal reaches a value of the order of 100 nm, it becomes comparable to the photon wavelength relevant to resonant optical transitions.

2.1 Particle-in-a-box theory of electron-hole state

2.1.1 Particle in a spherically symmetric potential

The model of a spherical potential box is crucially important for electrons in quantum dots.

In the case of a spherically symmetric potential $U(r)$ in spherical coordinates r, θ and φ, where $r = \sqrt{x^2 + y^2 + z^2}$ and

$$x = r\sin(\theta)\cos(\varphi),\ y = r\sin(\theta)\sin(\varphi),\ z = r\cos(\theta), \tag{2.1.1}$$

the Hamiltonian is

$$H = -\frac{\hbar^2}{2mr^2}\frac{\partial}{\partial r}\left(r^2\frac{\partial}{\partial r}\right) - \frac{\hbar^2}{2mr^2}\frac{1}{\sin(\theta)}\left[\frac{\partial}{\partial\theta}\left(\sin(\theta)\frac{\partial}{\partial\theta}\right) + \frac{1}{\sin(\theta)}\frac{\partial^2}{\partial\varphi^2}\right] + U(r) \tag{2.1.2}$$

Because of the spherical symmetry of the potential, the wave function can be separated into function of r, θ and φ:

$$\Psi = R(r)\Theta(\theta)\Phi(\varphi) \tag{2.1.3}$$

and can be written in the form

$$\Psi_{n,l,m}(r,\theta,\varphi) = \frac{u_{n,l}(r)}{r}Y_{lm}(\theta,\varphi), \tag{2.1.4}$$

where Y_{lm} are the spherical Bessel functions, and $u(r)$ satisfies an equation

$$-\frac{\hbar^2}{2m}\frac{d^2u(r)}{dr^2} + \left[U(r) + \frac{\hbar^2}{2mr^2}l(l+1)\right]u(r) = Eu(r) \tag{2.1.5}$$

The state of the system is characterized by the three quantum numbers, namely, the principal quantum number n, the orbital number l, and the magnetic number m. The orbital quantum number determines the angular momentum value $\overline{L}$:

$$\overline{L}^2 = \hbar^2 l(l+1),\ l = 0, 1, 2, 3, ... \tag{2.1.6}$$

The magnetic quantum number determines the L component parallel to the z-axis

$$L_z = \hbar m,\ m = 0, \pm1, \pm2, ..., \pm l. \tag{2.1.7}$$

Every state with a certain l value is $(2l+1)$ - degenerate according to $2l+1$ values of m. The states corresponding to different l values are usually denoted as *s*-, *p*-, *d*-, *f* - and *g*-states, and further in alphabetical order. States with zero angular momentum ($l = 0$) are referred to as *s*-states, states with $l = 1$ are denoted as *p*-states and so on. The parity of states corresponds to the parity of the l value, because the radial function is not sensitive to inversion (r remains the same after inversion), and the spherical function after inversion transforms as follows:

$$Y_{lm}(\theta,\varphi) \to (-1)^l Y_{lm}(\theta,\varphi). \tag{2.1.8}$$

The specific values of energy are determined by a $U(r)$ function. Considering the simplest case, corresponding to a spherically symmetric potential well with an infinite barrier, i.e.,

$$U(r) = \begin{cases} 0 & \text{for } r \le a \\ \infty & \text{for } r > a \end{cases} \tag{2.1.9}$$

l	$n=1$	$n=2$	$n=3$
0	$3.142(\pi)$	$6.283(2\pi)$	$9.425(3\pi)$
1	4.493	7.725	10.904
2	5.764	9.905	12.323
3	6.998	10.417	
4	8.183	11.705	
5	9.356		
6	10.513		
7	11.657		

Table 2.1: Roots of the Bessel functions χ_{nl}

In this case energy values are expressed as follows:

$$E_{nl} = \frac{\hbar^2 \chi_{nl}^2}{2ma^2}, \tag{2.1.10}$$

where χ_{nl} are roots of the spherical Bessel functions with n being the number of the root and l being the order of the function. Table 2.1 lists χ_{nl} values for several n,l values. Note that for $l = 0$ these values are equal to πn ($n = 1, 2, 3, ...$) and Eq. (2.1.10) converges with the relevant expression in the case of a one-dimensional box $E_n = n^2\pi^2\hbar^2/(2ma^2)$.

2.1.2 Weak confinement

In larger quantum dots, when the dot radius, a, is small but still a few times larger than the exciton Bohr radius, a_B^* , quantization of the exciton center-of-mass motion occurs. Starting from the dispersion law of an exciton in a crystal (Eq. (1.4.7)), we have to replace the kinetic energy of a free exciton by a solution relevant to a particle in a spherical box (Eq. (2.1.10)). The energy of an exciton is then expressed in the form

$$E_{nlm} = E_g - \frac{Ry^*}{n^2} + \frac{\hbar^2 \chi_{lm}^2}{2Ma^2},\ n, l, m = 1, 2, 3, ... \tag{2.1.11}$$

with the roots of the Bessel function χ_{lm} (Tab. 2.1). Here $M = m_e^* + m_h^*$ is the exciton mass which equals the sum of the electron m_e^* and hole m_h^* effective masses. An exciton in a spherical quantum dot is characterized by the quantum number n describing its *internal* states arising from the Coulomb electron-hole interaction (1S; 2S, 2P; 3S, 3P, 3D; . . .), and by the two additional numbers, m and l, describing the states connected with the center-of-mass motion in the presence of the *external* potential barrier featuring spherical symmetry (1s, 1p, 1d . . . , 2s, 2p, 2d . . . , etc.). To distinguish the *internal* and the *external* states, we shall use capital letters for the former and lower case for the latter. For the lowest 1S1s state ($n = 1$, $m = 1$, $l = 0$) the energy is expressed as

$$E_{1S1s} = E_g - Ry^* + \frac{\pi^2\hbar^2}{2Ma^2} \tag{2.1.12}$$

or in an equivalent way

$$E_{1S1s} = E_g - Ry^* \left[1 - \frac{\mu}{M}\left(\frac{\pi a_B^*}{a}\right)^2\right] \tag{2.1.13}$$

where $\mu = m_e^* m_h^*/(m_e^* + m_h^*)$ is the electron-hole reduced mass. Therefore the first exciton resonance in a spherical quantum dot experiences a high-energy shift by the value

$$\Delta E_{1S1s} = \frac{\mu}{M}\left(\frac{\pi a_B^*}{a}\right)^2 Ry^*. \tag{2.1.14}$$

Note this value remains small as compared to Ry^* since we consider the case $a \gg a_B^*$. This is the quantitative justification of the term *weak confinement*.

2.1.3 Strong confinement

The strong confinement limit corresponds to the condition $a \ll a_B^*$. That means that the confined electron and hole have no bound state corresponding to the hydrogen-like exciton. Supposing the absence of interactions between an electron and a hole as a reasonable starting approximation we consider quantization of an electron and a hole motion separately and apply the Eq (2.1.10) independently to an electron and a hole. The "free" electron and hole in a spherical potential box have the energy spectra

$$E_{lm}^e = E_g + \frac{\hbar^2 \chi_{lm}^2}{2m_e^* a^2},\ E_{lm}^h = -\frac{\hbar^2 \chi_{lm}^2}{2m_h^* a^2} \tag{2.1.15}$$

if we consider the top of the valence band E_V as the origin of the energy scale, i.e. $E_V = 0$.

However an electron and a hole are confined in space similarly to, or even more compact than, spatial extension of the exciton ground state in the ideal infinite parent crystal so the Coulomb potential and the confinement potential should be examined. The problem leads to the two-particle Schrödinger equation with Hamiltonian

$$H = -\frac{\hbar^2}{2m_e^*}\nabla_e^2 - \frac{\hbar^2}{2m_h^*}\nabla_h^2 - \frac{e^2}{\epsilon|\overline{r_e} - \overline{r_h}|} + U(r). \tag{2.1.16}$$

The appearance of the $U(r)$ potential does not allow independent consideration of the center-of-mass motion and the motion of a particle with reduced mass. The problem is solved via variational approach and leads to an energy of the ground electron-hole pair state (1s1s) of the form [5, 6, 7]

$$E_{1s1s} = E_g + \frac{\pi^2\hbar^2}{2\mu a^2} - 1.786\frac{e^2}{\epsilon a}, \tag{2.1.17}$$

in which the term proportional to $e^2/\epsilon a$ describes the effective Coulomb electron-hole interaction in a medium with dielectric permittivity ϵ. Comparing this term with the exciton Rydberg energy $Ry^* = \frac{e^2}{2\epsilon a_B^*}$ and bearing in mind that our consideration is still for the strong confinement limit ($a \ll a_B^*$), one can see that Coulomb interaction by no means vanishes in small quantum dots.

The exciton lowest state energy measured as a deviation from the bulk band gap energy E_g in the strong confinement limit can be written in a more general way as a raw expansion

$$E_{1s1s} - E_g = \left(\frac{a_B^*}{a}\right)^2 Ry^* \left[A_1 + \frac{a}{a_B^*}A_2 + \left(\frac{a}{a_B^*}\right)^2 A_3 + ...\right] \tag{2.1.18}$$

with the small parameter $a/a_B \ll 1$. The first coefficient A_1 for various states is described by the roots of the Bessel function (Table 2.1). The second coefficient A_2

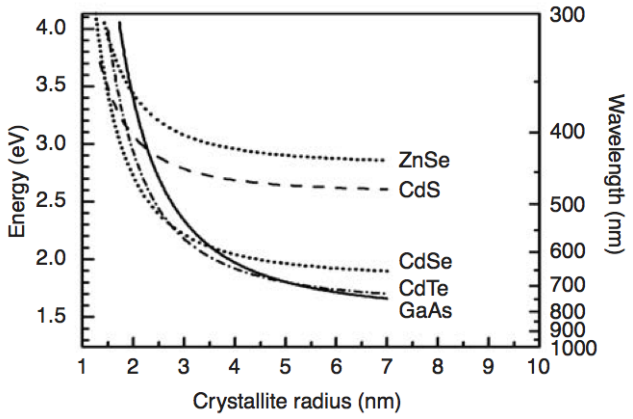

Figure 2.1: Size-dependent photon energy and light wavelength of the first absorption resonance for nanocrystals of various semiconductor materials (ZnSe, CdS, CdSe, CdTe, GaAs) calculated using Eq.(2.1.18)

corresponds to the Coulomb term and takes the following values: $A_2 = -1.786$ for the 1s1s-state, $A_2 = -1.884$ for the 1p1p-state, and values between -1.6 and -1.8 for other configurations [7]. The A_3 coefficient for the 1s1s-state was found to be $A_3 = -0.248$ [8].

From Figure 2.1 one can see that materials with a narrow band gap (GaAs, CdTe, CdSe) promise wide-band tunability of the absorption edge through hundreds of nanometers i.e. the width of the whole visible range of the electromagnetic wave spectrum. The small size cut-off ($a = 1.5$ nm) in the plots corresponds approximately to the reasonable applicability of the "particle-in-a-box" model.

2.2 Optical properties

Consider, for strong confinement approximation, i.e. without Coulomb interaction between electron and hole, the spontaneous emission for an excited exciton. The general equation for the electric dipole transition probability from an excited state $|b>$ to the ground state $|a>$ is given by the Fermi's golden rule:

$$A_{ba}(ED) = \frac{1}{\tau_{rad}} = \frac{1}{4\pi\epsilon_0}\frac{4n\omega^3}{3\hbar c^3}\left(\frac{E_{loc}}{E}\right)^2 \frac{1}{g_b}\sum_{a_n,b_m} |<a_n|\mu_c|b_m>|^2 \tag{2.2.1}$$

where $A_{ba}(ED)$ is the transition probability (s^{-1}) and is the inverse of the (radiative) life time τ_{rad}, n is the refractive index, ω is the transition frequency, $(E_{loc}/E)^2$ is the local field correction factor and g_b is the degeneracy of the excited state. The summation is over all levels in the ground state $|a_n>$ and excited state $|b_m>$ for the transition dipole moments μ connecting the levels. For an allowed electric dipole transition the transition dipole moment $\mu = e \cdot r$ and with $r = 10^{-10}$ m (approximately the Bohr radius of an hydrogen atom) and $n = 1.7$ this gives $A(ED) = 10^8 s^{-1}$ in the visible spectral region. For QDs this equation is often rewritten as:

$$A_{ba}(ED) = \frac{2e^2\omega\epsilon_1^{1/2} f}{3m_0c^3} \tag{2.2.2}$$

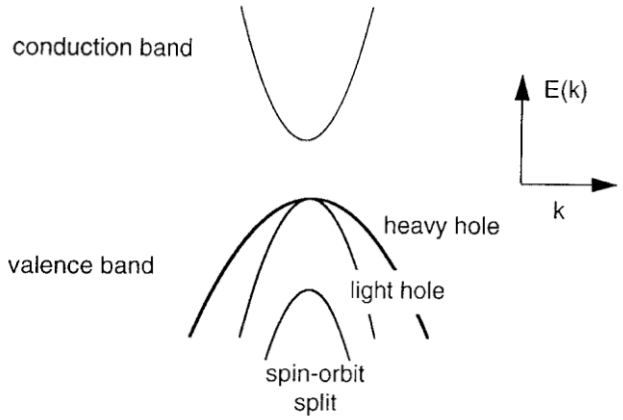

Figure 2.2: Band structure with light and heavy hole and spin-orbit splitting for II-VI semiconductors nanocrystals

where the oscillator strength f is given by

$$f = \frac{2P^2}{m_0 E_{1S_h 1S_e}} \tag{2.2.3}$$

P is the momentum transition moment of the exciton and is known as the Kane inter band parameter and m_0 is the free mass of the electron [9]. For CdSe $2P^2/2m_0 \sim 17.5\,eV$. If we take 0.4 eV confinement energy in addition to the bulk band-gap, then $f \sim 9$ for the first exciton of CdSe [10]. In addition to radiative decay, non-radiative decay processes influence the decay kinetics of excitons in QDs. An important non-radiative relaxation process is the trapping of an exciton or charge carriers at a defect or impurity site in the QD or at the QD surface.

Because of the three-dimensional spatial confinement in QDs, the solution of the Schrödinger equation results in describing the electron and hole wave functions with angular momenta L_e and L_h, respectively. However, this approach ignores the complexities of the II-VI semiconductors with diamond, zincblende and wurtzite lattices in which the lowest conduction minimum is formed from s-type orbitals and the valence band is formed from p-type orbitals. The sixfold degenerate valence band is split by spin-orbit coupling into a band-edge fourfold degenerate $J = 3/2$ band and a twofold degenerate $J = 1/2$ band. In a semiconductor with wurtzite structure, the $J = 3/2$ band is further split into light- and heavy-hole subbands with J projections $M_j = \pm 1/2$ and $\pm 3/2$, respectively (see Fig. 2.2).

For dot hole levels arising from these bands the envelope function angular momentum, L_h and the unit cell angular momentum, J, are not good quantum numbers. Only the total angular momentum, $F = L_h + J$, and parity are conserved. So a commonly used notation [11] labels the electron states, which are not affected by the valence band complications, as nL_e ($1S_e$, $2S_e$, $1P_e$) and the hole states as nL_F ($1S_{1/2}$, $1S_{3/2}$, $1P_{1/2}$), where n is the principal quantum number (1,2,3 etc.). The first level of electrons is $1S_e$ while for holes it's a $1S_{3/2}$ state. For optical transitions in ideal spherical QDs, the selection rules are $\Delta n = 0$, $\Delta L = 0, \pm 2$ (conservation of parity) and $\Delta F = 0, \pm 1$.

Figure 2.3 shows observed excited state energy spacings (relative to $1S_{3/2}1S_e$) as a function of the energy of the $1S_{3/2}1S_e$ state. The dashed lines represent the evolution of observed transitions with size. The solid lines are the prediction [12]. Avoided

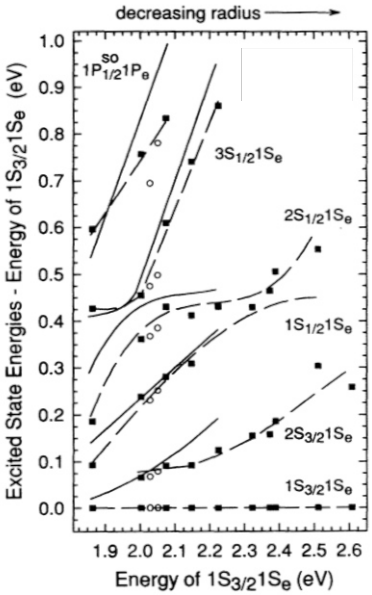

Figure 2.3: Excited state plotted relative to $1S_{3/2}1S_e$. The x axis is size dependent energy of $1S_{3/2}1S_e$. White and black dots represents experimental data fitted with dashed line. Solid line are represent computed energy levels [12].

transitions have been observed, like $2S_{1/2}1_e$ and $3S_{1/2}1_e$. Inclusion in theory of band anisotropy could make these transitions allowed by a mixing of the states. Alternative possibilities for breaking the parity selection rule are polar shape asymmetry, permanent dipole moment or quadupolar transitions [10].

The emission spectrum of a nanocrystal ensemble with narrow size distribution displays a band Stokes-shifted with respect to the excitation band edge (Figure 2.4). Like the optical absorption bands, the fluorescence spectra are blue-shifted as the nanocrystal diameter is reduced. The pronounced Stokes shift is due to the relaxation of excited electrons via acoustic phonon emission from the second or third excited state to the band edge state ($1S_e$), from where radiative recombination occurs. The ensemble emission spectrum of nanocrystals is very symmetric, in contrast to conventional dyes that suffer from a long IR vibronic tail. However, the full width at half maximum (FWHM) of $\sim$ 30 nm hides the true atomic-like nature of the nanocrystals. The broadening of the ensemble spectrum is due to the size dispersion inherent to the synthesis (inhomogeneous broadening) and spectral diffusion.

Now we want to take in account the Coulomb interaction of electron-hole. In the effective mass approximation the $1S_e$ electron interacts with the $1S_{3/2}$ hole giving rise to an 8-fold degenerate state. The degeneracy is lifted by electron-hole exchange interaction, the crystal field and crystal shape asymmetry into five states. These are then labelled according to the total angular momentum projection

$$G = m_F + m_s \tag{2.2.4}$$

giving one level with $G = \pm 2$, two with $G = \pm 1$ and two with $G = 0$. m_F and m_s are the projections along the z-axis of the hole total angular momentum F and the electron spin s, respectively. The dot size dependence of the band edge splitting is given for spherical QDs in Fig. 2.5. Letters U and L refers to upper and lower states and $G = \pm 2$ state corresponds to the exciton ground state for all dot sizes R, and is optically passive, i.e. dark.

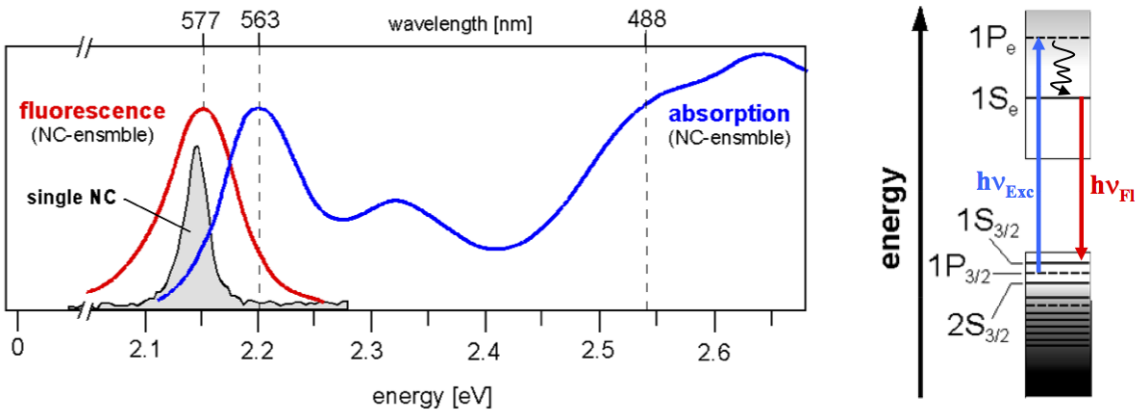

Figure 2.4: (Left) Comparison of the room temperature optical absorption and photoluminescence spectra of a CdSe QDs ensemble with narrow size distribution, as well as the luminescence of individual QDs. (Right) Energy levels involved in the optical absorption and fluorescence of a CdSe QDs [13].

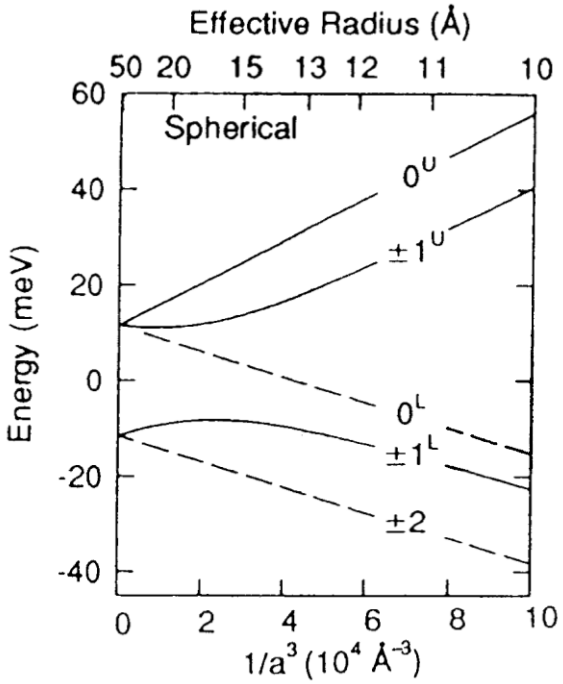

Figure 2.5: The size dependence of the exciton band edge energy for spherical QDs. Solid lines are for optically active levels while dashed lines correspond to passive levels [14].

Mixing of the e and h spin momentum states following on e-h exchange interaction does alter the optical transition probabilities. The wave functions of the $|G| = 2$ exciton state however does appear to remain unaltered by this interaction, and it is in fact optically passive (dark) in the dipole approximation, since any emitted or absorbed photon during a transition cannot have an angular momentum projection of ± 2, but only ± 1. The $\pm 1^L$, 0^L and the ± 2 exciton states all represent the optically passive (dark) exciton states, while the $\pm 1^U$ and the 0^U remain as the three states that carry nearly all of the optical intensity.

2.3 Quantum dot properties control

As seen before, size of quantum dot is the most important parameter that allow to tune absorbance and emission spectra in a wide range of optical bandwidth. However this is not the only factor because nanocrystals have a diverse and growing range of parameters that can modulate their electronic band gaps (Figure 2.6) including size, shape, and composition.

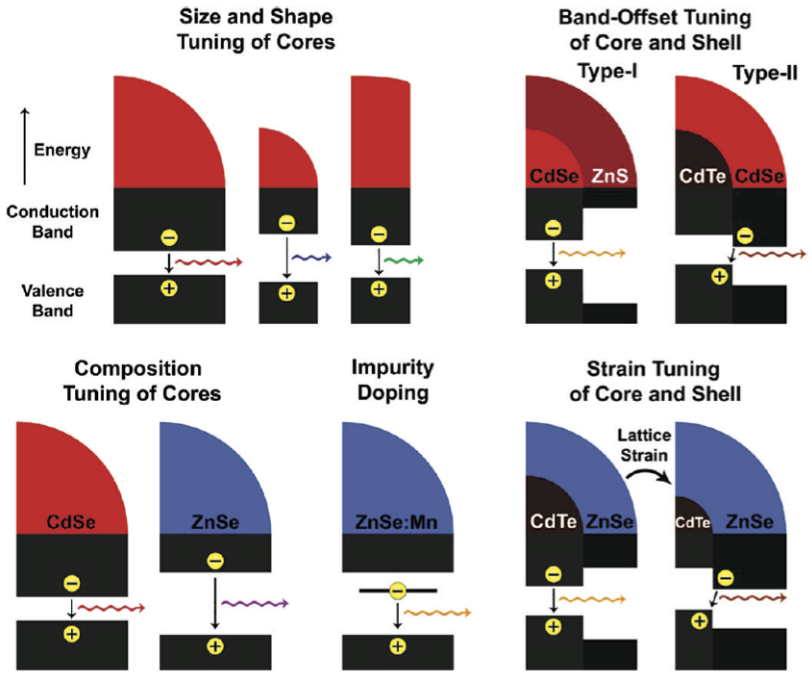

Figure 2.6: Mechanisms of band gap engineering in semiconductor nanocrystals through size, shape, composition, impurity doping, heterostructure band offset, and lattice strain [15].

2.3.1 Surface properties

As the crystal becomes smaller the number of atoms on the surface increases and this can impact the optical properties. The atoms on the surface of a crystal facet are incompletely bonded within the crystal lattice, thus disrupting the crystalline periodicity and leaving one or more "dangling orbital" on each atom pointed outward from the crystal. Most nanocrystals are highly faceted (Figure 2.7A-C), and each surface contains a periodic array of unpassivated orbitals with two-dimensional translational symmetry,

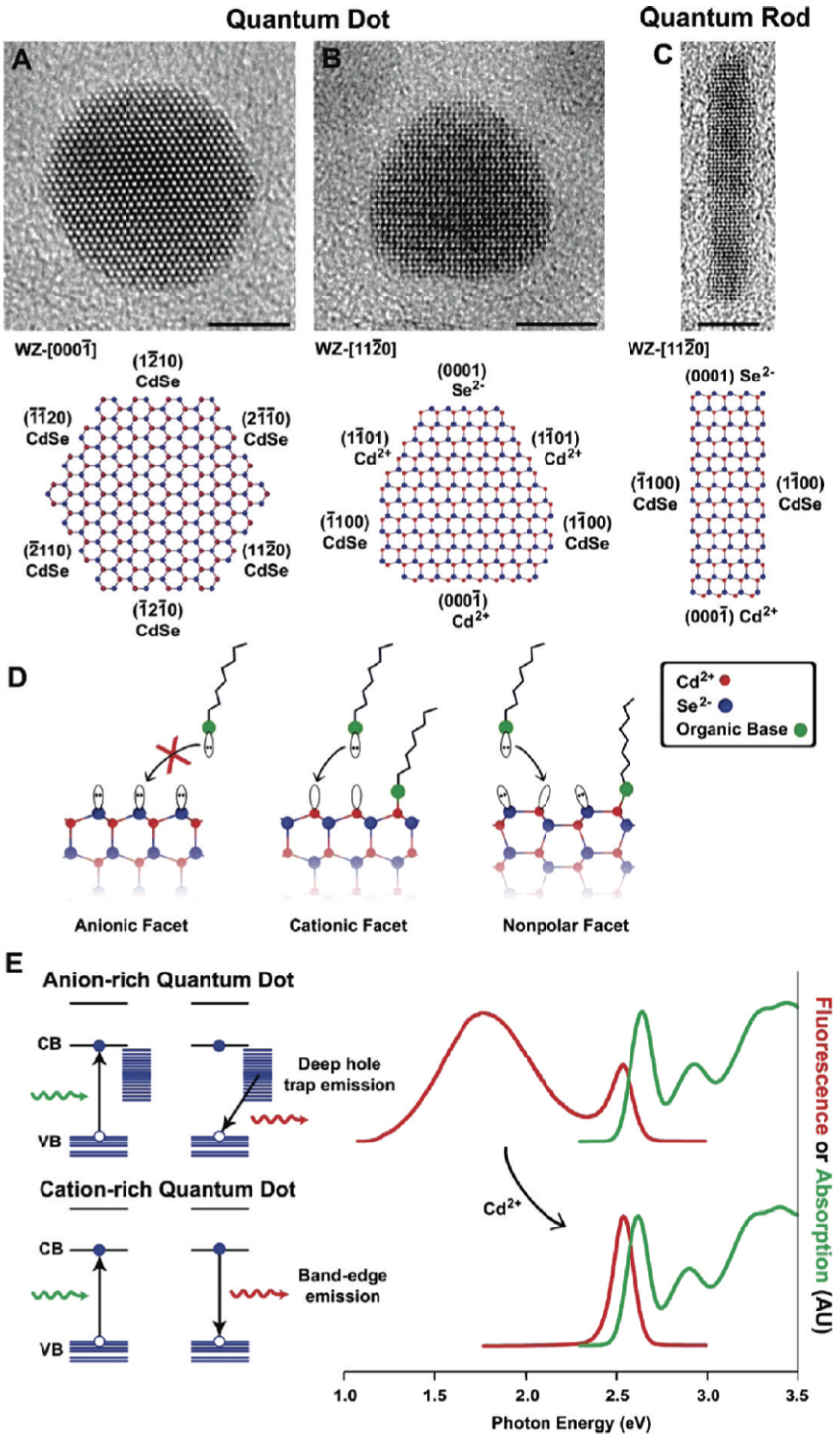

Figure 2.7: Surface properties of CdSe nanocrystals. Panels (A) and (B) depict transmission electron micrographs of quasi-spherical quantum dots with two orientations on the substrate, and panel (C) depicts a quantum rod. All scale bars are 5 nm. In the atomic models, the crystalline orientations and lattice facets are identified by their Wurtzite (WZ) Miller indices, and the polarity of each facet is noted as Cd^{2+} for cationic, Se^{2-} for anionic, and CdSe for nonpolar. Panel (D) illustrates the terminal dangling orbitals on each type of facet, and panel (E) shows the effects of surface hole traps on the fluorescence of small 2.1 nm nanocrystals [15].

which may form a band structure similar to that of the three-dimensional crystal itself. If these surface energy states are within the semiconductor band gap, they can trap charge carriers at the surface, thereby reducing the overlap between the electron and hole, increasing the probability of nonradiative decay events. In practice, however, most semiconductor nanocrystals are not used in vacuum, but suspended in solution and coated with organic ligands such as trioctylphosphine oxide (TOPO) or hexadecylamine (HDA). Thereby, the dangling bonds on the exposed facets are passivated by bonding with atoms or molecules (Figure 2.7D), minimizing intraband gap surface states and reducing surface atomic reconstruction. For colloidal particle suspensions, molecules such as TOPO and HDA adsorb to the nanocrystal surface through dative ligand-metal bonds between the basic moiety on the ligand and metal atoms on the nanocrystal surface, solubilizing the crystals in nonpolar solvents through hydrophobic interactions with the alkyl chains on the ligands. Polar end groups and hydrophilic polymers may be similarly used to solubilize nanocrystals in polar solvents.

The fluorescence emission can be significantly modulated by alterations to the nanocrystal surface. For example, very small colloidal CdSe nanocrystals often display two fluorescence emission bands, one at the band edge and another at lower energy resulting from recombination at intraband gap defect sites on the surface (Figure 2.7E). Deep trap emission arises from the presence of Se^{2-} rich facets, which poorly bind to most basic ligands, making these nanocrystals especially prone to surface trapping of holes which primarily reside on the selenium sp^3 orbitals. Indeed, nanocrystals with surfaces terminated mostly by anions typically have little or no fluorescence emission due to the overwhelming number of surface trap states for nonradiative recombination. The addition of excess Cd^{2+} ions can passivate these selenium states, yielding cationic surfaces that can strongly bind to basic ligands, and electrostatically shield holes from surface traps. Surface modifications may also introduce defects on the nanocrystal surface. Small amounts of oxidizing agents such as hypochlorous acid or hydrogen peroxide can etch away fragments of the nanocrystal surface, leaving behind unpassivated orbitals and atomic vacancies.

2.3.2 Type-I core@shell

Type-I core@shell quantum dots are nanocrystallites coated with higher band gap inorganic materials that has been shown to improve the photoluminescence quantum yields by passivating surface nonradiative recombination sites. Some examples of these quantum dot structures include CdS on CdSe and CdSe on CdS, ZnS grown on CdS, ZnS on CdSe and the inverse structure, CdS/HgS/CdS quantum dot quantum wells, ZnSe overcoated CdSe, and SiO2 on Si. In the following sections only CdSe@ZnS and CdSe@CdS are investigated.

Figure 2.8 shows the room-temperature photoluminescence spectra (PL) of CdSe dots ranging from 23 to 55 Å core diameter before (dashed lines) and after (solid lines) overcoating with ZnS. The PL quantum yield increases from 5 to 15% for bare dots to values ranging from 30 to 50% for dots passivated with ZnS. In smaller CdSe dots the surface-to-volume ratio is very high, and the PL for TOPO capped dots is dominated by broad deep trap emission due to incomplete surface passivation. Overcoating with ZnS suppresses deep trap emission by passivating most of the vacancies and trap sites on the crystallite surface, resulting in PL which is dominated by band-edge recombination. The evolution of the PL for the same 40 Å diameter dots with ZnS coverage is displayed in Figure 2.9. As the coverage of ZnS on the CdSe surface increases, we see a dramatic increase in the fluorescence quantum yield followed by a steady decline after ∼1.3

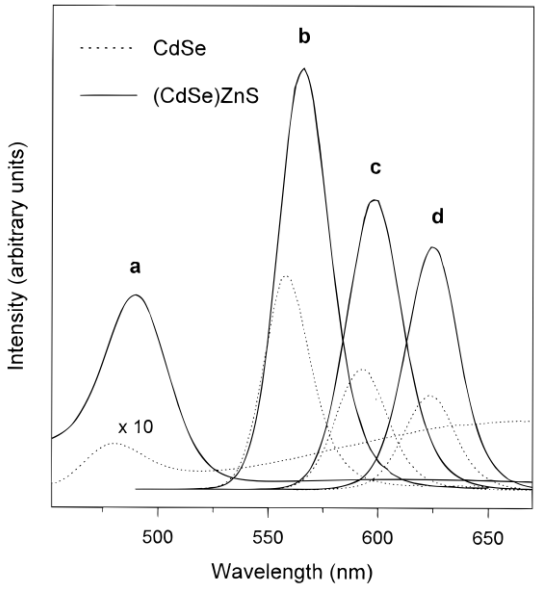

Figure 2.8: Photoluminescence (PL) spectra for bare (dashed lines) and ZnS overcoated (solid lines) dots with the following core sizes: (a) 23, (b) 42, (c) 48, and (d) 55 Å in diameter. The PL spectra for the overcoated dots are much more intense owing to their higher quantum yields: (a) 40, (b) 50, (c) 35, and (d) 30 [16].

monolayers of ZnS. The definition of a monolayer here is a shell of ZnS that measures 3.1 Å (the distance between consecutive planes along the [002] axis in bulk wurtzite ZnS). The spectra are red-shifted and show an increased broadening at higher coverage.

A theoretical explanation of the electronic structure is given using a simplified model of noninteracting particles in a spherical box. The potential energy inside the CdSe core is zero and the barrier height is 0.9 eV for both the electron and hole to tunnel into the ZnS shell [16]. In this picture the electron (hole) must tunnel through a 4 eV (10 eV) barrier to extend into the surrounding organic matrix. The Coulomb attraction between the electron and hole is treated in first-order perturbation theory. Solutions for the composite particles are obtained by solving the continuity relations for the electron and hole wave functions (2.3.1) and the probability currents (2.3.2) at the CdSe/ZnS interface [16]:

$$R_{1S,CdSe}(k_1 r_1) = R_{1S,ZnS}(\kappa_2 r_1) \tag{2.3.1}$$

$$\frac{1}{m^*_{CdSe}} \frac{d}{dr} R_{1S,CdSe}(k_1 r_1)|_{r=r_1} = \frac{1}{m^*_{ZnS}} \frac{d}{dr} R_{1S,ZnS}(\kappa_2 r_1)|_{r=r_1} \tag{2.3.2}$$

where $R_{1S,CdSe}$ and $R_{1S,ZnS}$ are the lowest energy radial wave functions for the electron or hole in the CdSe core and ZnS shell, respectively, r_1 is the radius of the CdSe core, m^*_{CdSe} and m^*_{ZnS} represent the hole or electron bulk effective masses in CdSe and ZnS, respectively, and k_1 and κ_2 are the wave vectors in CdSe and ZnS, respectively.

Figure 2.10 shows the radial probabilities of the electron and hole in the lowest energy $1S_{3/2}$-$1S_e$ eigenstates for bare (TOPO capped) ∼20 Å radius CdSe dots (a) and for the same dots with a 4 Å ZnS (b) or 4 Å CdS (c) shell. In the bare dots the wave function of the lighter electron spreads over the entire particle and tunnels only slightly into the surrounding organic matrix whereas the heavier hole has a higher

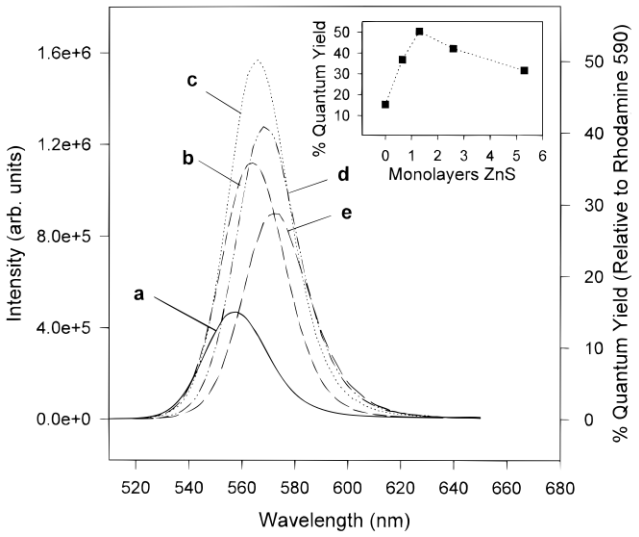

Figure 2.9: PL spectra for a series of ZnS overcoated dots with $42 \pm 10\%$ Å diameter CdSe cores. The spectra are for (a) 0, (b) 0.65, (c) 1.3, (d) 2.6, and (e) 5.3 monolayers ZnS coverage. The position of the maximum in the PL spectrum shifts to the red, and the spectrum broadens with increasing ZnS coverage. (inset) The PL quantum yield is plotted as a function of ZnS coverage. The PL intensity increases with the addition of ZnS reaching, 50% at ∼1.3 monolayers, and then declines steadily at higher coverage [16].

probability at the center of the dot and does not extend into the surrounding matrix. When a shell of ZnS surrounds the CdSe particle, the electron wave function tunnels into the ZnS shell while the hole wave function has a negligible probability of spreading into the ZnS layer. The increased delocalization of the electron lowers its confinement energy and consequently the energy of the excited state. Beyond a certain thickness of the ZnS shell the electron and hole wave functions cannot spread out further, and the confinement energies remain constant. In CdS the barrier height for the electron (0.2 eV) is smaller than the total energy of the electron, and thus its wave function extends well into the CdS shell. The hole, however, must tunnel through a 0.55 eV barrier into the CdS shell and therefore has lower probability of penetrating into the surrounding CdS matrix than the electron but extends into the CdS more than it does for a ZnS shell.

As to the PL quantum yield, it reaches its maximum value when the coverage is ∼1.3 monolayers, indicating that most of the surface vacancies and non radiative recombination site are passivated. At higher coverage the growth is epitaxial and heterogeneous as dislocations or other defects are created to accommodate the mismatch in lattice constants between ZnS and CdSe. The decrease in quantum yield at higher coverage is therefore attributed to the formation of defects in the ZnS shell.

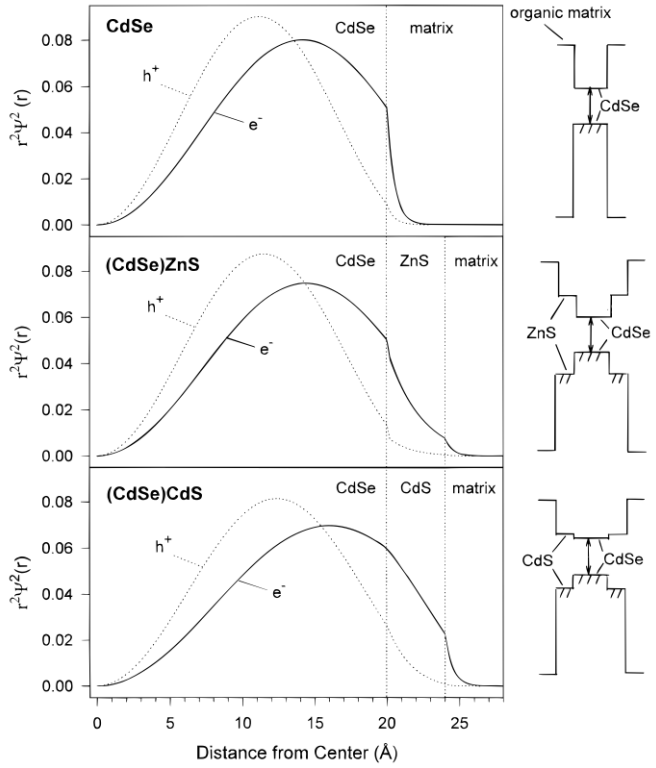

Figure 2.10: Radial probability functions for the lowest energy ($1S_{3/2}$-$1S_e$) electron and hole wave functions in (A) bare 20 Å diameter CdSe dots, (B) (CdSe)ZnS dots with a 20 Å diameter core and a 4 Å ZnS shell, and (C) (CdSe)CdS dots with an identical core and a 4 Å CdS shell. The sketches to the right show the approximate band offsets between the various components [16].

2.3.3 Type-II core@shell

As seen before a type-I QD has shell band-gap that is bigger than core one. As a result, both electrons and holes are confined in the cores. A type-II QD, in contrast, has both the valence and conduction bands in the core lower or higher than in the shell. As a result, one carrier is mostly confined to the core, while the other is mostly confined to the shell (Fig. 2.11(top)). This spatial separation of carriers leads to new properties different from type-I QD. Potential energy diagrams for CdTe/CdSe and CdSe/ZnTe QDs are shown in Figure 2.11(bottom). A simple modeling of the radial wave functions for the electron and hole in their lowest energy levels shows the expected separation of carriers. For CdTe/CdSe QDs, the hole is mostly confined to the CdTe core, while the electron is mostly in the CdSe shell. In CdSe/ZnTe QDs, the band offsets are reversed, so that the electron resides mostly in the CdSe core, while the hole is mostly in the ZnTe shell.

Type-II emission originates from the radiative recombination of the electron-hole pair across the core-shell interface. The energy of the emission thus depends on the band offsets of the two materials making up the core and the shell. Type-II QDs can thus emit at energies that are smaller than the band gap of either material.

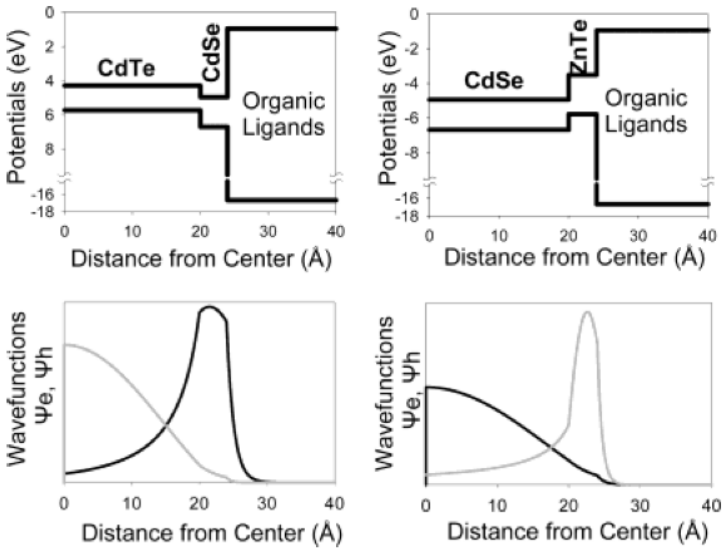

Figure 2.11: Potential diagrams (top) and modeled electron (gray) and hole (black) radial wave functions (bottom) for CdTe/CdSe(core/shell) QD (left) and CdSe/ZnTe(core/shell) QD (right). Potentials are referenced to the vacuum level. A 20-Å core radius and a 4-Å shell thickness are used in the modeling [17].

2.3.4 Strain tuning

Colloidal semiconductor quantum dots such as (CdSe)ZnS (core)shell materials have a large mismatch in bond length between the core and shell materials (12%), generating a strain field in the nanocrystal. Growth of a material on a substrate with a different bond length can only proceed to a critical thickness before a lattice defect (commonly a misfit dislocation) arises near the interface to ease the strain, allowing the materials to relax to their native bond lengths and introducing carrier traps in the process. However an isolated nanocrystal can deform to adapt to the overgrowth of a straining shell and the large surface area allows the stress to be distributed over a large fraction of the constituent atoms. Deformation of a semiconductor forces the material to adopt an unnatural bond length. Because the energies of the conduction and valence band edges derive from the bond strength in the crystal, changes in the bond length alter the electronic band gap. This change is described by the deformation potential, α, defined as

$$\alpha = \frac{\partial E_g}{\partial (lnV)}$$

where $\partial(lnV)$ is the fractional volume change. For II-VI and III-V materials, α is negative ($\alpha_{CdSe} = -2.9$), meaning that compression of the crystal widens the band gap (Figure 2.12).

Because such heterostructures can be grown coherently as a single crystalline domain, homogeneous lattice strain results in significant bond length alterations that can modify electronic band energies. Compressive strain will shift both the conduction and valence bands to higher energy, and tensile strain will shift the bands to lower energy. Thereby, the coherent growth of compressive shells (e.g., ZnSe or CdS) on CdTe core colloids yields dramatic changes to the relative energy bands in the heterostructure, resulting in type-II band alignments with widely tunable band gaps for these normally type-I heterostructures.

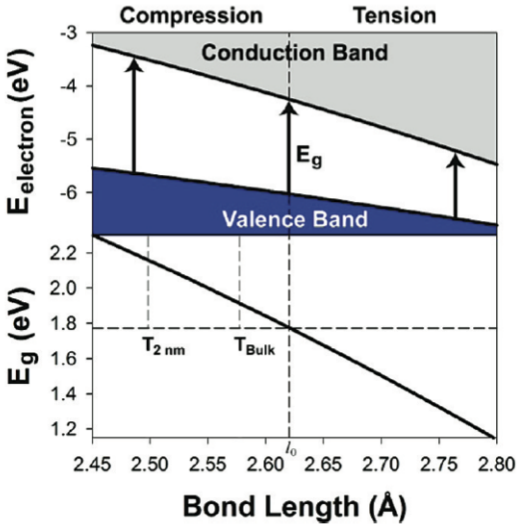

Figure 2.12: Change in the energy of the valence band edge, conduction band edge, and band gap as a function of CdSe bond length. The equilibrium bond length is noted on the x-axis ($l_0 = 2.62\,\text{Å}$) in addition to the bond length that results in a phase transition in bulk (T_{Bulk}) and for small 2 nm nanocrystals (T_{2nm}).

Strain also plays a critical role in warping (or bending) charge carrier wave functions at heterostructural interfaces. Because the strain field in a lattice-mismatched (core)shell quantum dot is inhomogeneous in the shell, the band edge is believed to deform over the radial direction, giving rise to inhomogeneous charge carrier distributions. This is likely the cause of the different fluorescence behaviors of (CdSe)CdTe and (CdSe)ZnTe nanocrystals. Both of these heterostructures are type-II with the hole sequestered in the shell and the electron in the core, but heterostructures with CdTe shells have quantum yields (20-40%) dramatically larger than that (<1%) with ZnTe shells. It is important to realize that the lattice mismatch between CdSe and CdTe is 7%, whereas the lattice mismatch is only 0.6% for ZnTe. The high strain in the CdTe shell will shift the hole wave function toward the core material, increasing the overlap between the electron and hole and thus the probability of carrier recombination. The near absence of strain for ZnTe shells substantially increases the wave function localization at the nanocrystal surface, where surface traps increase the probability of nonradiative relaxation. Indeed, in true unstrained type-II band alignments, the probability of band-edge recombination efficiency should be very low, and engineering the strain in such heterostructures may be important for modulating recombination versus carrier separation.

Chapter 3

Surface functionalization

Despite advances in nanoparticle synthesis and semiconductor modeling, the surfaces of quantum dots are poorly understood, particularly with respect to how the surface atoms and coordinating ligands impact the optical properties of the underlying nanocrystal. The innately high surface area-to-volume ratio of nanocrystals requires the surface to contain a large fraction of the constituent atoms, which are incompletely bonded. Typically, organic surfactants adsorbed to this interface complete the dangling orbitals of surface atoms, effectively passivating the nanoparticle surface. For semiconductor nanoparticles, the extent of passivation is particularly important, significantly affecting the photoluminescence properties, especially quantum yield.

For organically-passivated nanoparticles, two independent interfaces play crucial roles in dictating nanoparticle properties (Fig. 3.1). The nanocrystal-organic surfactant interface plays an important role in nanocrystal structure and optoelectronics. The interface between the organic molecules stabilizing the QD dispersion and the surrounding medium largely influences the colloidal properties of the nanoparticles, such as the hydrodynamic size, charge and intermolecular/interparticle interactions. These interfaces can be intimately linked, particularly if a single molecule is responsible for both surfaces. For example, hydrophilic thiols bind to QD surface atoms and simultaneously stabilize QD dispersions in polar solvents, and as such, are responsible for the surface-related optical properties of the QDs and also for surface charge and possible aggregation. On the other hand, QDs with hydrophobic organic ligands can be encapsulated in a variety of surfactants for stabilization in polar solvents, allowing the optical properties to be dictated by the original underlying ligands, and the colloidal properties can be independently tuned by the encapsulating surfactant.

For this reasons a brief review on nanoparticle surface functionalization techniques is reported.

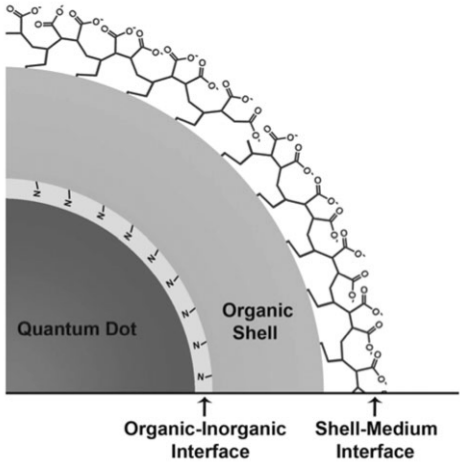

Figure 3.1: Schematic illustration of QDs dispersed in aqueous medium. The QD surface is directly bonded to organic coordinating molecules. These ligands, and any surrounding polymeric coating, dictate the thickness of the organic shell, which provides a protective barrier from aqueous solutes. The outward facing organic molecules influence the colloidal properties of the QD, such as surface charge and hydrodynamic diameter [18].

3.1 Stabilization against aggregation

The ligand molecules bound to the nanoparticle surface not only control the growth of the particles during synthesis, but also prevent the aggregation of the nanoparticles. The repulsive force between particles can, in principle, be due to electrostatic repulsion, steric exclusion or a hydration layer on the surface. Depending on the particle system, i.e. the core material and the solvent in which the particles are dispersed, the choice of the right ligand may yield to stable particles. First, the ligand molecules have to be bound to the particle surface by some attractive interaction, either chemisorption, electrostatic attraction or hydrophobic interaction, most commonly provided by a head group of the ligand molecule. Various chemical functional groups possess a certain affinity to inorganic surfaces, the most famous example being thiol (-SH) to gold. As to the interaction of the ligand molecule with the solvent, polar or charged ligand molecules provide solubility in polar or aqueous solvents, while nanoparticles with apolar ligand molecules such as hydrocarbon chains are only soluble in apolar organic solvents, e.g. hexane, toluene or chloroform. Certain amphiphilic ligand molecules, e.g. poly(ethylene) glycol (PEG), possess amphiphilic properties, and nanoparticles with those or other ligand molecules can be soluble in a number of solvents, with intermediate polarity.

In organic solvents, the nanoparticle surface is covered by hydrophobic ligand molecules that prevent the aggregation of the particle cores. However, the bonds between the inorganic nanoparticle surface and, e.g. an electron-donating end group of a ligand molecule, such as thiol, amine or phosphine, undergo dynamic binding and unbinding processes. This yields to the important consequence that the ligand molecules can detach, e.g. by excessive washing or mass action by another incoming ligand, which can compromise the stability of the nanoparticles that might ultimately aggregate and precipitate. In particular, in the case of fluorescent quantum dots, irradiation with light can enhance oxidation of the inorganic particle surface, and photo-oxidation may eventually result in aggregation caused by desorption of the stabilizing ligands. Figure

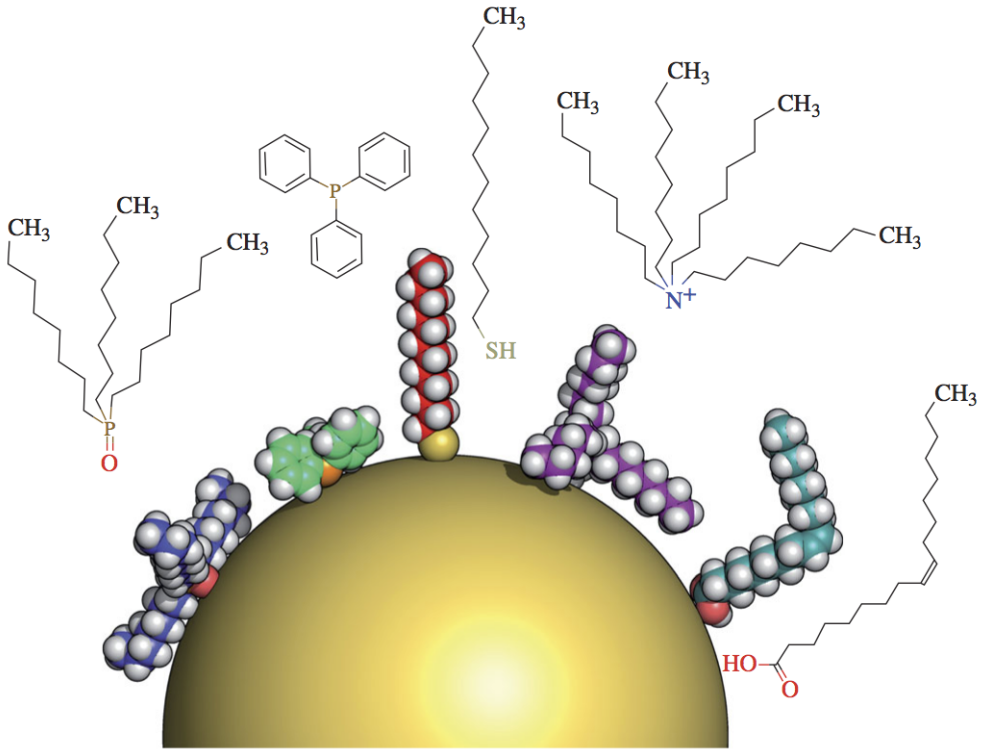

Figure 3.2: A nanoparticle of 5 nm core diameter with different hydrophobic ligand molecules both drawn to scale. The particle is idealized as a smooth sphere; the schematic molecule structures above are not drawn to scale. Left to right: trioctylphosphine oxide (TOPO), triphenylphosphine (TPP), dodecanethiol (DDT), tetraoctylammonium bromide (TOAB) and oleic acid (OA). The spatial conformation of the molecules is only shown schematically as derived from their chemical structure and space-filling models [19].

3.2 displays some commonly used hydrophobic ligand molecules drawn to scale along with a particle of 5 nm diameter.

In aqueous solutions, the ligand-nanoparticle interaction is basically the same, but a number of different effects that are important for stability arise. Most commonly, hydrophilic nanoparticles are stabilized by electrostatic repulsion by the equally charged ligand molecules on the particle surface. However, in the presence of high salt concentrations, the electric field is shielded, and the nanoparticles can come close to each other until the attractive forces, such as induced dipole interaction, i.e. van der Waals force, or hydrogen bonds, eventually cause the particles to agglomerate. Depending on the isoelectric point (pI) and the pH of the solution, nanoparticles can also lose or change the sign of their charge. In aqueous solutions, strongly charged ligand molecules, containing e.g. carboxylic or sulphonic acid groups, are found to stabilize the particles for longer time and also at more elevated salt concentrations.

3.2 Phase transfer

Since many types of colloidal nanoparticles are synthesized in organic solvents, for certain possible applications they have to be transferred to aqueous solutions, e.g. to be compatible with biological systems. In general, for phase transfer in both directions, three strategies can be used: ligand exchange, ligand modification and additional layers

of molecules that stabilize the particles in the desired phase.

3.2.1 Ligand exchange

In the ligand-exchange strategy, the molecules stabilizing the particles in the original first phase are replaced by other, more strongly binding ligands that allow the transfer to the second phase and provide colloidal stability there, e.g. by exchanging hydrophobic by hydrophilic ligands. Commonly used ligand molecules include thiol groups that bind strongly to inorganic surfaces of nanoparticles, e.g. Au and Ag or CdSe, replacing the weaker bound ligands that the nanoparticles usually have from synthesis (Figures 3.2 and 3.3). Examples include the transfer of TOP/TOPO-coated CdSe/ZnS quantum dots to an aqueous solution by replacing the phosphine-based hydrophobic ligands with a hydrophilic thiol-based molecule, often mercaptocarboxylic acids (e.g. mercaptoacetic acid (MAA), mercaptopropionic acid (MPA), mercaptoundecanoic acid (MUA), etc.). Variations include derivatives with multiple moieties, e.g. mercaptosuccinic acid (two carboxliyc groups) and lipoic acid (or dihydrolipoic acid, respectively, with two sulphhydryl groups).

In addition, ligand exchange protocols with amphiphilic molecules have been reported that allows one to dissolve the same particles in both polar and apolar solvents. Examples include small molecules that can change their orientation depending on the surrounding solvent or polymers that can be either non-ionic or ionic like poly(ethylenimine) (PEI) and poly(acrylic acid), in which the positively or negatively charged moieties can bind to the inorganic particle surface and render the surface of the whole particle polar. In those approaches, ligand exchange takes place in the same phase in which the nanoparticles are already present, but the new ligand molecules are then able to disperse the particles in other solvents.

An important issue with respect to ligand exchange and phase transfer is the stability of the optical properties in the case of fluorescent quantum dots. Especially when brought to the aqueous phase, both the particle surface and possibly the thiol group of the ligands are prone to oxidation. Often the fluorescence quantum yield is reduced and desorption of the ligand molecules can eventually yield to aggregation. This effect can be further enhanced by irradiation of the particles with light.

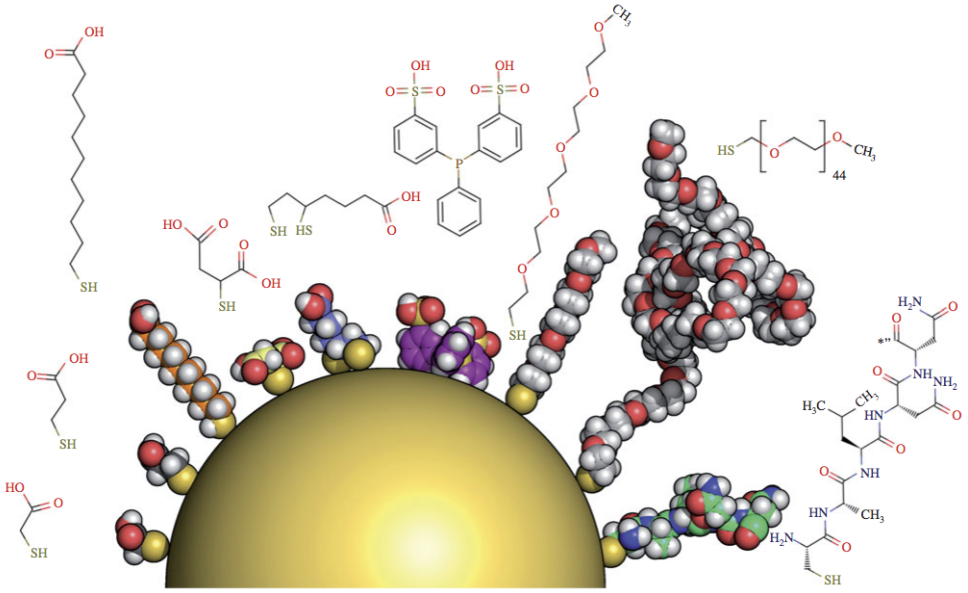

Figure 3.3: A nanoparticle of 5 nm core diameter with different hydrophilic ligand molecules drawn to scale. The particle is idealized as a smooth sphere; the schematic structures of the molecules above are not to drawn to scale. Left to right: mercaptoacetic acid (MAA), mercaptopropionic acid (MPA), mercaptoundecanoic acid (MUA), mercaptosuccinic acid (MSA), dihydrolipid acid (DHLA), bis-sulphonated triphenylphosphine, mPEG$_5$-SH, mPEG$_4$5-SH (2000 g mol$^{?1}$) and a short peptide of the sequence CALNN [19].

3.2.2 Ligand modification

An alternative approach to phase transfer is ligand modification: the ligand molecule stabilizing the nanoparticles in the original first phase is rendered hydrophilic or hydrophobic to transfer and stabilize the particles in the second phase. The concept of ligand modification may provide efficient phase transfer because the particles are modified with a new ligand in the same phase they are already in. However, it is restricted to certain systems that are compatible with each other and for which the colloidal stability of the nanoparticles is maintained during the reaction.

3.2.3 Additional coating layers

The third strategy for phase transfer is an additional molecular layer on the particles that adsorbs on the original ligand molecules and changes the surface properties accordingly. In this way, a ligand bilayer is formed that allows one to transfer hydrophobic nano particles to water and vice versa. The molecules acting as phase-transfer agents have to be amphiphilic, comprise a hydrophobic and a hydrophilic part, commonly one or more aliphatic chains and a polar, often charged, end group.

The additional layer conserves the native environment of the inorganic nanoparticles because the original ligand molecules are not replaced. This may be beneficial e.g. to prevent sensitive core materials from oxidation. Owing to the additional layer bound by hydrophobic interactions, this coating strategy can be applied regardless of the material of the inorganic particle core.

Naturally, by any additional layer, the nanoparticle size is increased, and owing to the nature of organic molecules, these organic shells appear to be rather soft.

3.2.4 Polymer coatings

Although there are a number of well-established variations of phase transfer by ligand exchange, in particular mercaptocarboxylic acid-based ligands for the transfer of nanoparticles from the organic to the aqueous phase, this approach suffers from several drawbacks: (i) small ligands with one head group binding to the nanoparticle surface can easily desorb and impair the stabilization of the particles, especially in solutions free of excess unbound ligands, and (ii) although thiol-containing ligands bind relatively strongly to various metal particles and quantum dots, in general the ligand molecule has to be carefully matched to the given core material, which is reflected in the large variety of reported protocols. In contrast, an additional amphiphilic coating layer that adsorbs by hydrophobic interaction to the hydrophobic ligand molecules of the nanoparticles has the advantage that it does not depend on the inorganic core material (and possibly not even on the exact type of ligand molecules) since the adsorption is predominantly based on hydrophobic interaction of hydrocarbon chains and Van der Waals forces throughout the molecules. In the case of amphiphilic polymers, many contact points between the ligand molecules and the polymer prevent facile desorption of the polymer molecule from the particle, e.g. by thermal fluctuations. Finally, the coated particles have the same physical and chemical surface properties independently of their core material.

One common example includes a poly(acrylic acid)-based polymer with hydrophobic side chains.

Another closely related class of amphiphilic polymers is based on poly(maleic anhydride) copolymers that are synthesized by copolymerization of maleic anhydride with olefins, resulting in alternating copolymers. When coming into contact with water (or an opening agent like ethanolamine), the maleic anhydride rings hydrolyse and open, forming two carboxylic groups each (Fig 5.5).

The comb-like amphiphilic polymers used for the synthesis of nanoparticles are made up of either an alternating or random sequence of building blocks that consist commonly of aliphatic chains as hydrophobic elements and charged groups as hydrophilic parts. Hydrophobic side chains cover or intercalate the hydrophobic ligand molecules of the nanoparticles, while the hydrophilic backbone is exposed to the outside aqueous environment. Even though the attraction between the polymer and the particle is due to rather weak Van der Waals forces between the aliphatic chains, the hydrophobic interaction and the large number of contact points by the several side chains of the polymer result in a very stable coating.

3.3 Particle functionalization

3.3.1 Functional gropus

Ligand particles stabilizing the nanoparticles against aggregation can simply consist of an inert molecular chain (hydrocarbon chain or PEG) or have functional groups that are, in most cases, terminating linear molecules. In the case of water-soluble nanoparticles, these functional groups are often carboxylic acids stabilizing the nanoparticles by electrostatic repulsion, and can be exploited for the conjugation of other molecules to the particles. Typical functional groups used with quantum dots are -COOH, -OH, -NH_2. Functional groups present on the nanoparticle surface can be converted to other functional groups by bifunctional molecules. Commonly found carboxylic groups can be reacted with primary amines by means of a condensation reaction

to yield amide bonds. For this, a water-soluble carbodiimide (e.g. 1-Ethyl-3-(3-dimethylaminopropyl)carbodiimide; EDC) is commonly used (see Fig. 5.7). After forming an intermediate compound with the carboxylic moiety, the activated group is reactive towards primary amines. In the case of primary amines present on the particle surface, active ester compounds (N-hydroxy-succinimide; NHS) can be used to equally form amide bonds.

Common to all chemical surface modification schemes involving functional groups that are present on the nanoparticle surface is that they predominantly depend on the ligand shell or surface coating, not on the actual inorganic core material. Therefore, provided that the nanoparticles are stable under the reaction condition and subsequent purification, the same chemical routes for functionalization apply for Au nanoparticles, quantum dots or magnetic particles as well as for silica nanoparticles.

3.3.2 Bioconjugation

Bioconjugation of colloidal nanoparticles is the extension of the described concepts of ligand exchange and chemical functionalization to biomolecules. Nature offers a large variety of organic molecules of different composition, size and complexity that serve to provide structure and function to biological processes and organisms. Examples include, on the one hand, small molecules like lipids, vitamins, peptides, sugars and larger ones such as natural polymers including proteins, enzymes, DNA and RNA.

Conjugation of inorganic nanoparticles to biomolecules generates hybrid materials that can be used to make the nanoparticles interact specifically with biological systems. Nanoparticle-biomolecule conjugates bring together the unique properties and functionality of both materials, e.g. fluorescence or magnetic moment of the inorganic particles and e.g. the ability of biomolecules for highly specific binding by molecular recognition. The strategy for the conjugation of biomolecules to nanoparticles generally falls into four classes:

- ◇ ligand-like binding to the surface of the inorganic particle core, commonly by chemisorption of e.g. thiol groups,
- ◇ electrostatic adsorption of positively charged biomolecules to negatively charged nanoparticles or vice versa,
- ◇ covalent binding by conjugation chemistry, exploiting functional groups on both particle and biomolecules, and
- ◇ non-covalent, affinity-based receptor-ligand systems.

Chapter 4

Glucose oxidase

Peptides and proteins are polymeric compounds of amino acids, linked into sequences by amide bonds. Short sequences, peptides usually consisting of up to 50-100 amino acids, are commercially available by custom synthesis, while proteins are usually found in the form of larger poly-amino acids exhibiting a tertiary and possibly quaternary structure. Special classes of proteins comprise enzymes. Enzymes are highly specialized molecules with reactive centres that catalyse biochemical reactions and are responsible for metabolism.

Proteins are generally made up by a sequence of 20 different standard amino acids (in addition to other naturally occurring or synthetic amino acids) that are linked together by amide bonds and possess different side-chain residues. Naturally, each peptide or protein has one carboxylic and one primary amino group respectively, while the amino acid side chains introduce additional functional groups or other properties, depending on their molecular structure. The amino acid sequence determines the unique properties of each of a large number of possible structures, i.e. 20^n for a sequence of n amino acids, in terms of charge, polarity and hydrophobicity. These, in turn, determine the secondary and tertiary structure that a protein is folding into and that ultimately results in the functionality of the biomolecule. In many cases, the specific function of a protein (enzyme, antibody) is determined by the geometric and physicochemical properties of the outer surface, given by the motifs of the folded amino acid sequence. Often the inside of a protein is hydrophobic, while hydrophilic amino acid side chains tend to point outwards into solution, while for instance membrane proteins generally have a partially hydrophobic surface. Cysteine residues, even if far apart in the sequence, can come spatially close to each other in folded proteins and form stabilizing disulphide bonds. The thiol group of a terminal cysteine residue can also be exploited as the anchor group for the attachment of a peptide to the surface of nanoparticles.

This clearly makes peptides and proteins interesting objects to be combined with inorganic nanoparticles, both for basic research and applications that make use of the specific functions of these biomolecules.

Among all type of enzymes used by biopharmaceutical companies, glucose oxidase has seen large-scale technological applications since the early 1950's. Glucose oxidase (GOx) has been purified from a range of different fungal sources, mainly from the genus *Aspergillus* and *Penicillium*, of which *A. niger* is the most commonly utilized for the production of GOx.

GOx is a dimeric glycoprotein consisting of two identical polypeptide chain subunits that are covalently linked together via disulfide bonds, with total molecular weight of 160kDa (GOx from *A. niger*) (Fig. 4.1).

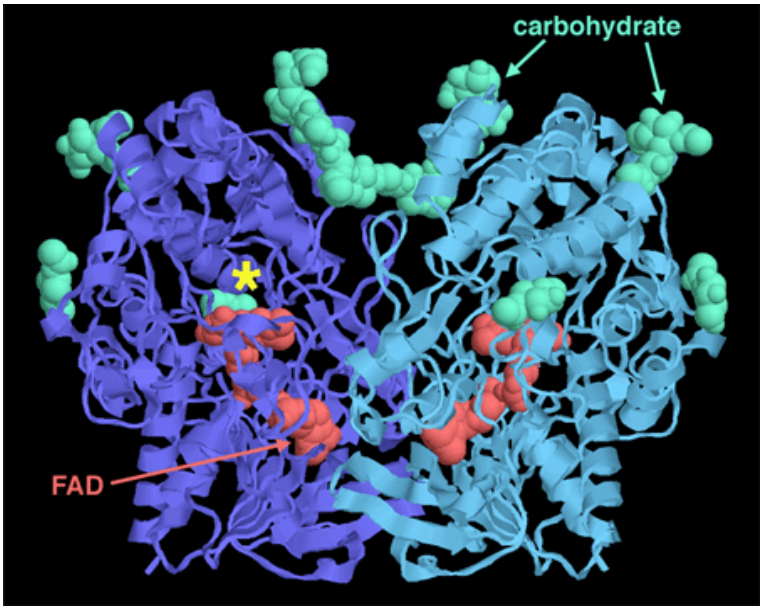

Figure 4.1: GOx structure from the Protein Data Bank (http://www.rcsb.org). The two polypeptide subunits are shown in purple and blue. The oxidation reaction is performed by the FAD cofactors bound deep inside the enzyme, shown in red. The active site where glucose binds is just above the FAD, in a deep pocket shown with a star. Notice that the enzyme, like many proteins that act outside of cells, is covered with carbohydrate chains, shown in green.

The catalytic center is constituted by two flavoprotein cofactor. Flavoproteins represent a large group of proteins involved in a wide variety of cellular processes, including electron transport and oxidation reactions. Flavoproteins contain derivatives of riboflavin, most notably flavin mononucleotide (FMN) and flavin adenine dinucleotide (FAD) (Fig. 4.2A), which is capable of adopting a number of different redox states, from fully oxidised (FAD_{OX}) to the fully reduced ($FADH^-$, $FADH_2$) (Fig. 4.2B,C).

GOx catalyses the oxidation of β-D-glucose to D-glucono-δ-lactone and H_2O_2 using molecular oxygen as an electron acceptor. This reaction can be divided into a reductive and an oxidative step (Fig. 4.3). In the reductive half reaction, GOx catalyzes the oxidation of β-D-glucose to D-glucono-δ-lactone, which is non-enzymatically hydrolyzed to gluconic acid. Subsequently the flavine adenine dinucucleotide ring of GOx is reduced to $FADH_2$. In the oxidative half reaction, the reduced GOx is reoxidized by oxygen to yield H_2O_2. The H_2O_2 is cleaved by catalase (CAT) to produce water and oxygen.

Since enzyme activity is dependent on the ionization state of the amino acids in the active site, pH plays an important role in maintaining the proper conformation of an enzyme. Most proteins are only active within a narrow pH range, usually in the range of 5-9. The optimal for GOx varies from 5.0 to 7.0. GOx from most fungi and yeast have pH optima in the acidic to neutral range such as *A. niger*.

With respect to the fluorescence properties of GOx, Fig. 4.4 shows the absorption and emission spectra for $FADH^-$ and $FADH_2$, compared with those for FAD_{OX}.

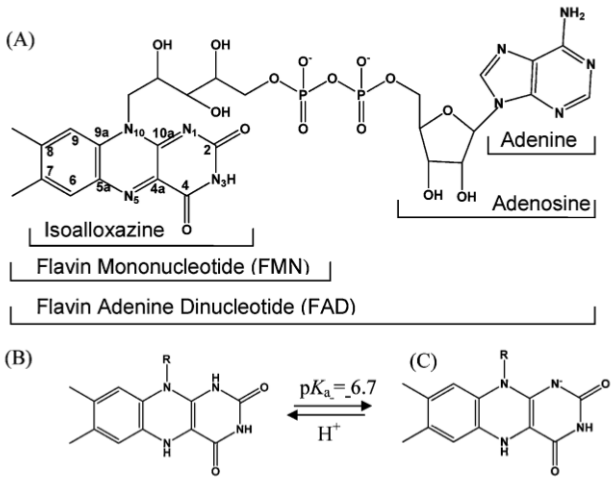

Figure 4.2: Chemical structures of flavoquinone (Oxidised) (A) and the two flavohydroquinones (Fully reduced forms) $FADH_2$ (B) and $FADH^-$ (C) (Only the isoalloxazine ring is shown for clarity) [20]

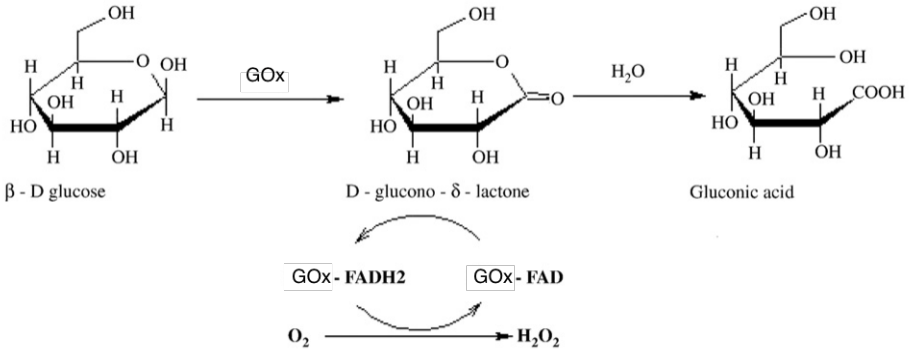

Figure 4.3: Representation of the GOx reaction [21].

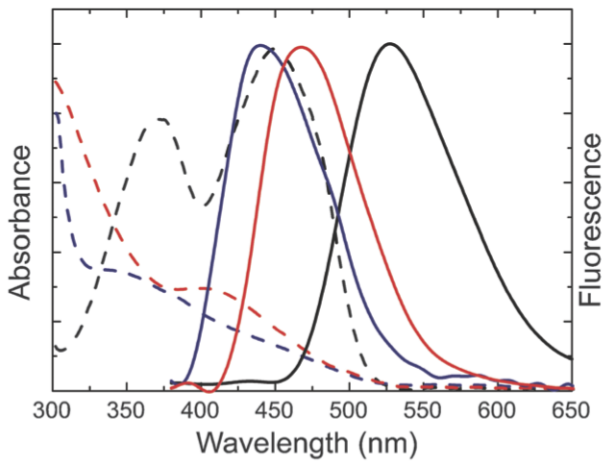

Figure 4.4: Electronic absorption (dash lines) and emission (solid lines) spectra for FAD_{OX} (Black) and its reduced forms $FADH^-$ (blue) $FADH_2$ (red). Emission spectra were recorded following excitation at 400 nm (FAD_{OX}) or 360 nm (reduced forms) [20].

Chapter 5

Materials and methods

5.1 Chemicals

Quantum dots

The quantum dots used in this project are supplied by Sigma Aldrich (Lumidots®). They are CdSe/ZnS core shell quantum dots, with a diameter of 6.3 nm and an emission peak of 640 nm (<40 nm FWHM). They are stabilized with a mixture of hexadecylamine (HDA) and trioctylphosphine (TOPO) ligands in toluene. Typical absorbance and fluorescence spectra are shown in Fig. 5.1a.

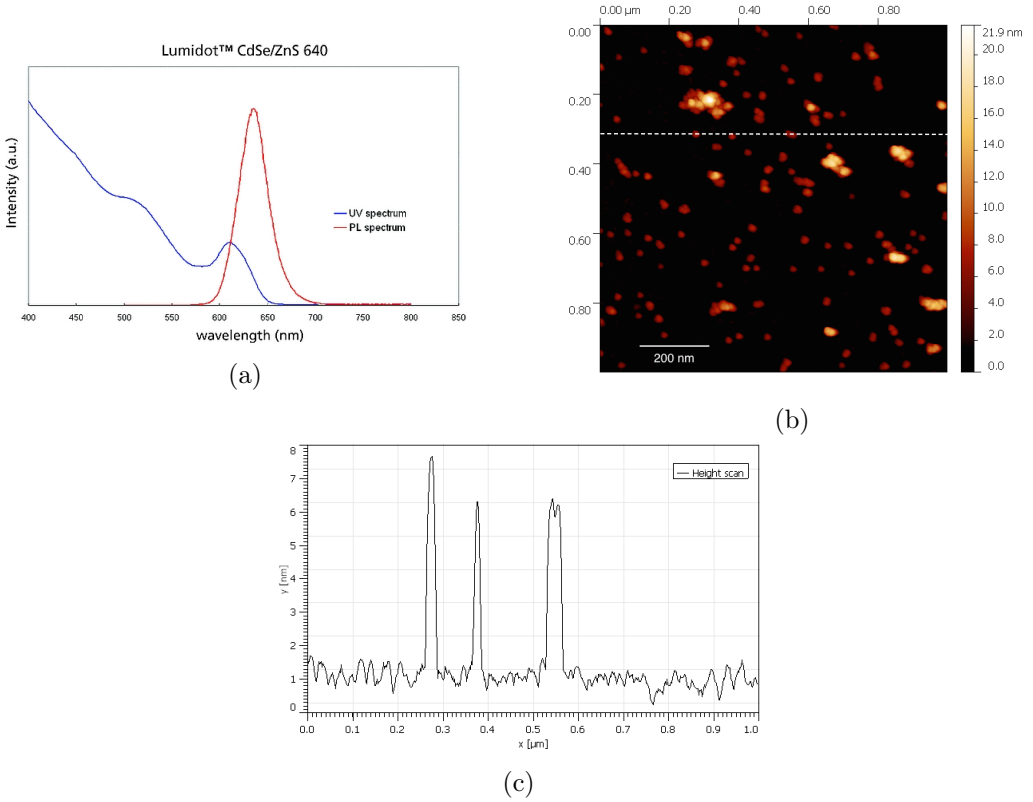

Figure 5.1: (a) Absorbance and fluorescence spectra of Sigma Aldrich Lumidots (from particle data sheet); (b) AFM image of micellized quantum dots; (c) Height scan of AFM image along the dashed line in (b).

Quatum rods

We used CAN's *CANdots series A plus* quantum rods. They are CdSe/CdS core shell quantum dot-in-rod, with an emission length of 560 nm or 590 nm (both types have been used), <35 nm FWHM, stabilized with organic ligands in toluene. Optical characteristics and image are shown in Fig. 5.2.

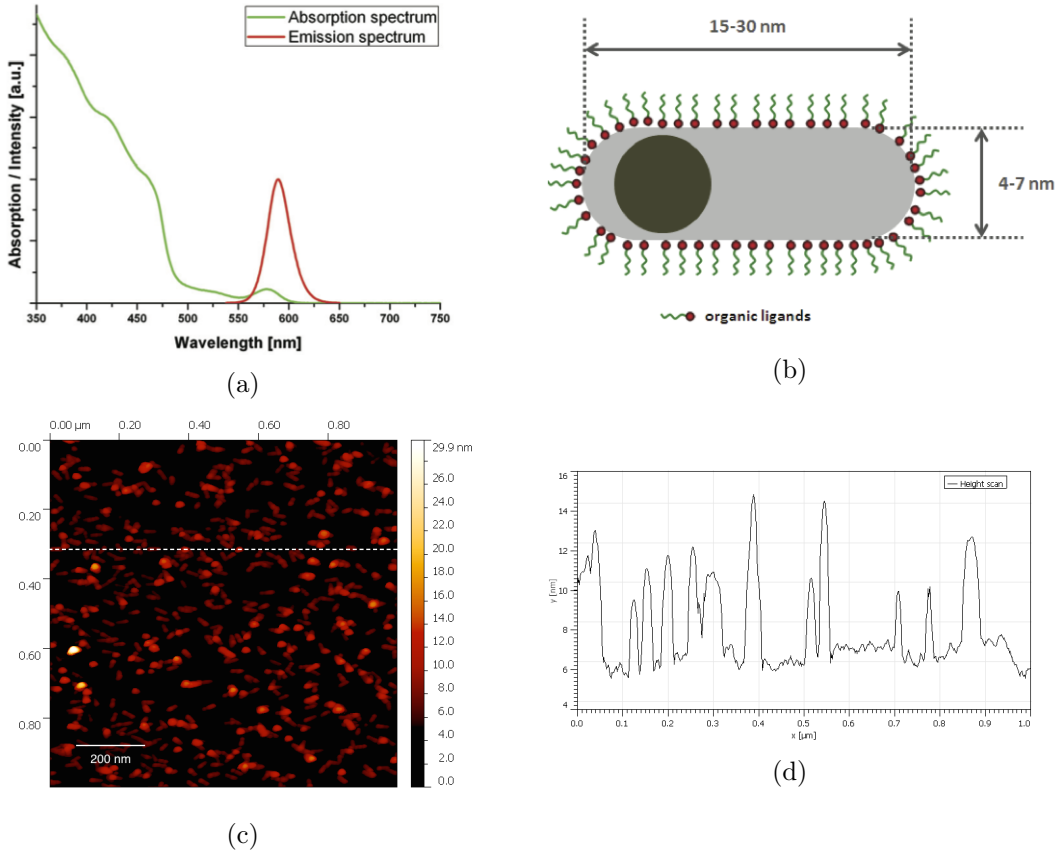

Figure 5.2: (a) Absorbance and emission spectra of 590nm quantum rods (from particle data sheet); (b) Sketch of a core-shell quantum dot-in-rod (provided by supplier); (c) AFM image of micellized quantum rods; (d) Height scan of AFM image along the dashed line in (c).

PSMA

Poly(styrene-*co*-maleic anhydride) terminated with cumene (PSMA, averaged molecular weight ∼1700 g/mol) was purchased from Sigma Aldrich. The molecular representation of the polymer is given in Fig.5.3

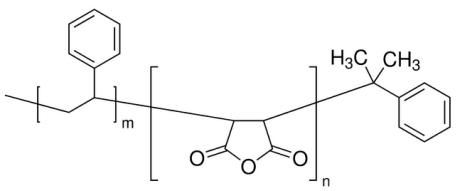

Figure 5.3: Molecular representation of PSMA

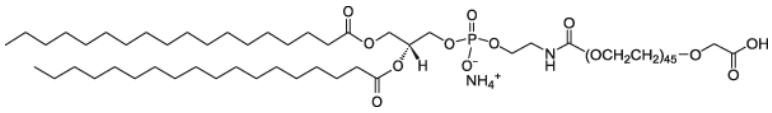

DSPE-PEG(2000)

Two types of polyethylene glycol (PEG)-lipid conjugates were purchased by Avanti polar lipids and used for nanocrystal encapsulation:

- DSPE-PEG(2000) Carboxylic Acid, product name 1,2-distearoyl-sn-glycero-3-phosphoethanolamine-N-[carboxy(polyethylene glycol)-2000] (ammonium salt), molecular weight 2849.507 (Figure 5.4a);
- DSPE-PEG(2000) Carboxylic Acid, product name 1,2-distearoyl-sn-glycero-3-phosphoethanolamine-N-[methoxy(polyethylene glycol)-2000] (ammonium salt), molecular weight 2805.497 (Figure (5.4b)

(a) DSPE-PEG(2000) Carboxylic Acid

(b) DSPE-PEG(2000) Methoxy

Figure 5.4: DSPE-PEG(2000) phospholipids

Other chemicals

Ultrapure water (18.2 $\mathrm{M\Omega\cdot cm}$) was obtained from a Sartorius Stedim Arium Pro UF system.
EDC or 1-Ethyl-3-(3-dimethylaminopropyl)carbodiimide is a water soluble carbodiimide, molecular weight 155.24 g mol^{-1}.
NHS or N-Hydroxysuccinimide, molecular weight 115.09 g mol^{-1}.
All other chemicals were purchased from Sigma Aldrich.

pH measurements

A Mettler Toledo *S220 SevenCompact pH/Ion* pH-meter was used to measure the pH of buffers, solutions and samples. The sensivity used for the pH measurments was 0.01.

5.2 Phase transfer

In order to transfer quantum dots/rods from toluene to water, two different techniques have been used: polymer coating and micelle encapsulation.

5.2.1 Polymer coating

Quantum dots (rods) were transferred to water through polymer encapsulation following a method reported in literature [22]. QDs in toluene (200 μL) were dried with N_2 and dissolved again in 1 mL $CHCl_3$ containing 17mg/mL PSMA, in order to give an excess of polymer. The reaction mixture was shaken at room temperature (RT) for 3

h. A 2 mL portion of aqueous solution containing 20 μL Ethanolamine (EA, 99.5%) was added to the QDs/PSMA $CHCl_3$ solution and shaken for 30 min at RT. After that the QDs were transferred into the water phase with ∼100% efficiency. The sample was centrifuged in order to speed up the separation of the chloroform and the water phases. A schematic diagram of protocol is given in Fig.5.5.

The protocol used for the coating of the quantum rods was the same as before, however the efficiency of the transfer was worse, since many rods were still in the chloroform phase. In order to try to avoid this problem, other two batches of rods were prepared with 1.7 mg/mL and 85 mg/mL PSMA in chloroform, however any evidence of improvement was found.

Quantum dots/rods in water were centrifuged in PALL Nanosep 10kDa molecular weight cutoff ultrafiltration tubes to remove excess polymer and EA and to exchange water with the desired buffer for further use.

Figure 5.5: Scheme showing the steps involved in the preparation of water-soluble QDs using poly(styrene-co-maleic anhydride) (PSMA). PSMA was added to CdSe/ZnS QDs capped with hydrophobic ligands in chloroform. An amine-terminated ligand, ethanolamine (EA), was added to PSMA capped QDs in chloroform to ring open the maleic anhydride groups and generate the amphiphilic polymer coating. The resulting QDs coated with amphiphilic PSMA are soluble in aqueous media [22].

5.2.2 Micelle encapsulation

Protocol for quantum dots

500 μL of acetone/methanol (50:50) solution were added to 500 μL quantum dots in toluene. The solution was then centrifuged at 6000 rpm for 4 minutes to pelletize the quantum dots. Supernatant were discarded and quantum dots were then redissolved in 500 μL chloroform containing 5 mg/mL 50:50 DSPE-PEG-Methoxy/DSPE-PEG-COOH phospholipids. The solution was shaken in a dark ambient over night. Quantum dots were then dried with N_2 and redispersed in water. The protocol is schematized in Fig.5.6.

Quantum dots in water were centrifuged in a 10kDa ultrafiltration tubes in order to remove excess phospholipids and to exchange the water with the desired buffer for further use.

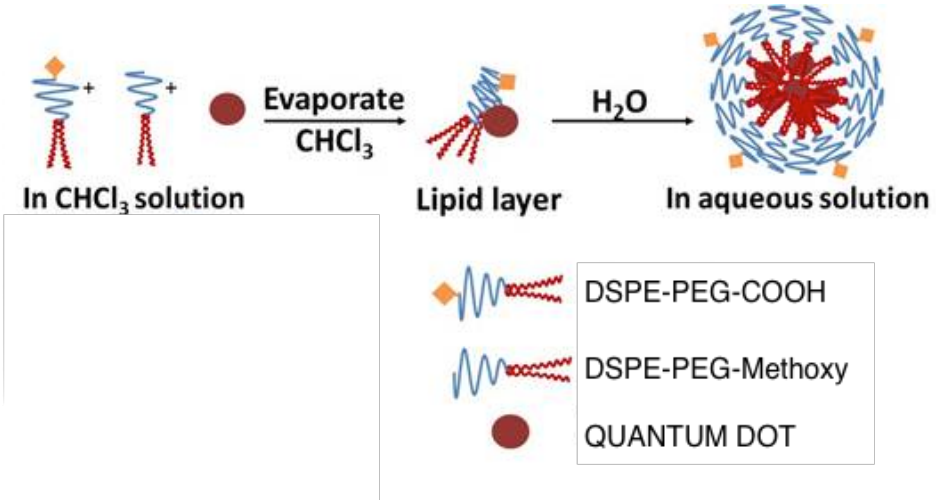

Figure 5.6: Scheme showing micelle encapsulation of quantum dots with PEGylated phospholipids [23]

Protocol for quantum rods

100 μL of acetone/methanol (50:50) solution was added to 200 μL of quantum rods in hexane. The solution was then centrifuged at 6000 rpm for 4 minutes in order to palletize the quantum rods. The supernatant was discarded and the quantum rods were then redissolved in 200 μL hexane and purified again. Dried quantum rods were dissolved in 1000 μL chloroform containing 5 mg/mL of DSPE-PEG-COOH phospholipids. The solution was shaken in a dark ambient over night. Quantum dots were then dried with N_2 and redispersed in water.

Quantum dots in water were centrifuged in a 10kDa ultrafiltration tubes in order to remove excess phospholipids and to exchange the water with the desired buffer for further use.

5.3 Functionalization

Carboxylates (-COOH) may react with a carbodiimide such as EDC in the presence of NHS, resulting in a semi-stable NHS ester, which may then react with primary amines (-NH_2) forming amide crosslinks (Figure 5.7). Although prepared NHS esters are sufficiently stable in order to process in a two-step reaction scheme, both groups will hydrolyze within hours or minutes, depending on water-content and pH of the reaction solution (NHS esters have a half-life of 4-5 hours at pH 7, 1 hour at pH 8 and only 10 minutes at pH 8.6). The activation reaction with EDC shows the maximum efficiency at pH 4.5-7.2, and EDC reactions are often performed in MES buffer at pH 4.7-6.0. For best results in two-step reactions, the first reaction is performed in MES buffer at pH 5-6, then the pH is raised to 7.2-7.5 with the phosphate buffer immediately before the reaction with the amine-containing molecule.

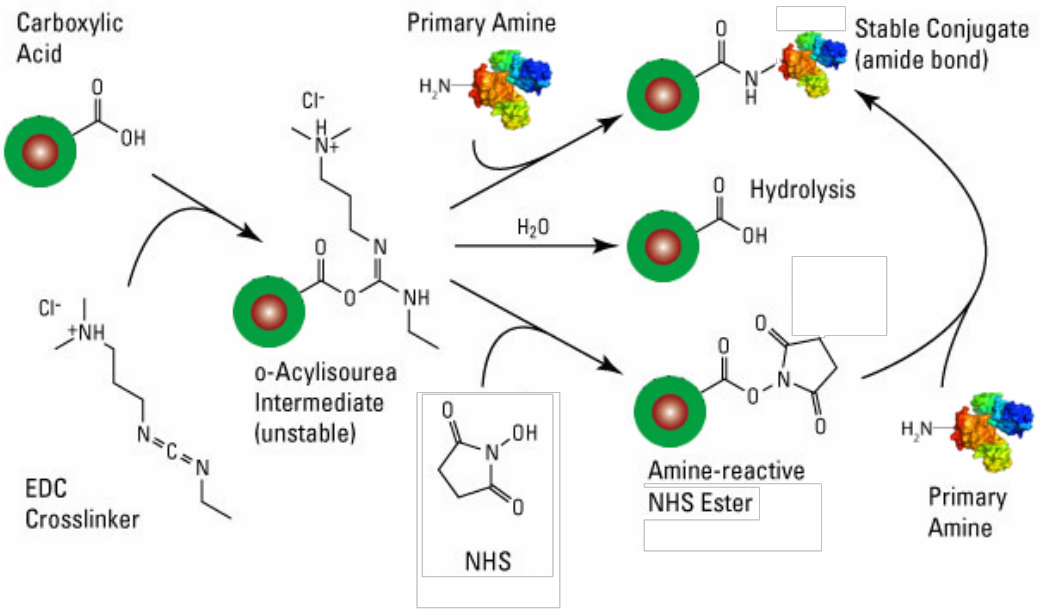

Figure 5.7: Common conjugation reaction for particles with carboxylic acid function: the water-soluble carbodiimide EDC forms an unstable intermediate, the so-called 'activated' carboxylic group. This group can either hydrolyse or react with a primary amino group, leading to the formation of a stable amide bond. Optionally, it can react with NHS or sulpho-NHS. The active ester has an extended half-life and reacts also with primary amines.

Additional materials required

- ◇ Activation Buffer: 0.1M MES (2-[morpholino]ethanesulfonic acid), 0.5M NaCl, pH 6.0
- ◇ Phosphate-buffered Saline (PBS): 0.1M sodium phosphate, 0.15M NaCl, pH 7.2-7.5
- ◇ QDs/QRods: Prepare QDs/QRods in activation buffer
- ◇ Enzyme: dissolved in a 10-fold molar excess relatively to QDs/QRods in PBS buffer
- ◇ EDC (1-ethyl-3-[3-dimethylaminopropyl]carbodiimide).

NHS-ester activation

- ◇ Add EDC (final concentration 5mM [24]) directly to QDs/QRods solution
- ◇ Add NHS (final concentration 5mM [24])
- ◇ Mix reaction components well and react for 20 minutes at room temperature.

Amine reaction

- ◇ Increase buffer pH above 7.0 using concentrated sodium bicarbonate
- ◇ Add Enzyme to the solution containing activated QDs/QRods

- ◇ Mix the solution well and then allow the reaction to proceed for 2 hours at room temperature in a dark ambient
- ◇ After the reaction is complete, filter the solution with ultrafiltration centrifuge tubes and redisperse in PBS buffer.

5.4 UV-visible absorbance and fluorescence measurements

5.4.1 Absorbance measurements

A GE Healthcare Ultrospec 2100 pro UV/Visible spectrophotometer was used to acquire absorbance measurements.

Absorbance spectra of quantum nanoparticles (NPs) were acquired at different steps of the process: as purchased, after they were transferred to water and after they were functionalized. A spectrum of concentrated glucose oxidase (2 mg/mL) in water was also acquired. This can give a first peace of information about the samples: comparing quantum dots in organic solvents with the same quantum dots transferred into water gives information about the aggregation, especially when looking at wavelengths longer than the first excitonic peak. Quantum particles as purchased do not absorb at these wavelengths, while in the presence of aggregated particles or empty micelles, absorption is observable.

An important quantity that can be calculated from absorbance spectra is the concentration of quantum dots/rods, given by:

$$[c] = \frac{A}{\epsilon l} \tag{5.4.1}$$

where $[c]$ is the concentration in molar (M), ϵ is the molar absorptivity at the first excitonic peak and l=1 cm is the length of the couvette. For the quantum dots the value of ϵ is given by the supplier ($\epsilon = 5.9 \cdot 10^5\, cm^{-1}M^{-1}$), while for the quantum rods no molar absorptivity is given. Since an estimation of the concentration is needed in the functionalization process, a value of $\epsilon = 6 \cdot 10^5\, cm^{-1}M^{-1}$ was assumed for the quantum rods.

Because of the different concentrations of the samples, a direct comparison between spectra is not possible. Instead, it was done a relative comparison between the two different steps of the functionalization protocol.

5.4.2 Fluorescence measurements

A Tecan Infinite 200 PRO plate-reader was used to measure the fluorescence of samples in a polystyrene well plate.

Fluorescence measurements were used in order to characterize the emission of the functionalized nano particles and to measure the effect of the enzyme activity. Each fluorescence spectrum was taken from a 200 μL aliquot solutions.

In order to study the emission properties, solutions containing nano particles were excited at the absorbance peak wavelengths of quantum dots/rods and glucose oxidase. Emission spectra were compared with two reference solutions: one with just nano particles transferred in water and the other with nano particles and enzyme mixed but not bound to each other. The quantities used to prepare the two reference solutions

	Conjugated nano particles	Unbound mixture	Nanoparticles
Polymer coated QDs	200 μL NPs-enzyme sol.	80 μL NPs sol. 80 μL 1 mg/mL GOx sol. 40 μL buffer sol.	80 μL NPs sol. 120 μL buffer sol.
Micelle encap. QDs	200 μL NPs-enzyme sol.	95 μL NPs sol. 95 μL 1 mg/mL GOx sol. 10 μL buffer sol.	95 μL NPs sol. 105 μL buffer sol.
Polymer coated QRods	200 μL NPs-enzyme sol.	95 μL NPs sol. 19 μL 1 mg/mL GOx sol. 86 μL buffer sol.	95 μL NPs sol. 105 μL buffer sol.
Micelle encap. QRods	200 μL NPs-enzyme sol.	45 μL NPs sol. 15 μL 1 mg/mL GOx sol. 140 μL buffer sol.	45 μL NPs sol. 155 μL buffer sol.

Table 5.1: Compositions of aliquots for fluorescence properties measurements. All solutes were dissolved in a 0.1M PBS 0.15M NaCl pH 7.4 buffer solution.

were calculated in order to obtain the same concentration of solute that was present in the functionalized nanoparticles solutions. (Table 5.1).

In order to measure the effect of enzyme activities on nanoparticles, 100 μL of conjugated nanoparticle-enzyme solutions in a 0.1M PBS 0.15M NaCl pH 7.4 buffer were mixed with 100 μL of glucose solutions in 0.1M PBS 0.15M NaCl pH 7.4 buffer at different concentrations (100 μM, 1 mM and 10 mM + one without glucose as reference). After that, they were immediately analyzed using the plate reader, by acquiring a spectrum every 5 minutes for 2 hours. An excitation wavelenght of 450 nm was obtained/measured.

Two reference solution were also analyzed: the first one consisted of 100 μL of nanoparticle solutions in a 0.1M PBS 0.15M NaCl pH 7.4 buffer mixed with 100 μL of 1 mM hydrogen peroxide 0.1M PBS 0.15M NaCl pH 7.4 solution, and the second one consisted of 100 μL of nanoparticle solutions in a 0.1M PBS 0.15M NaCl pH 7.4 buffer mixed with 100 μL of 10 mM glucose 0.1M PBS 0.15M NaCl pH 7.4 solution.

Chapter 6

Results and discussion

The aim of this thesis is to study the behavior of semiconductor nanoparticles (NPs) conjugated with glucose oxidase (GOx), in particular focusing on how the working enzymes and the reaction products influence the luminescence properties of the NPs. Two different types of nano crystals were used: CdSe/ZnS core/shell quantum dots and CdSe/CdS quantum dot-in-rods.

Since NPs were purchased in organic solvent, they were transferred into water before functionalization. It is well known that functionalization changes the surface properties of nano crystals and it defines properties such as aggregation, bleaching, quantum yield and surface etching. To have a better comprehension of the involved phenomena, both quantum dots and dot-in-rod were transferred into water with two different protocols, namely polymer coating and phospholipid micelle encapsulation.

In order to characterize each one of the four sample that were prepared, a three-step analysis protocol has been developed. First, an absorbance measurement was performed at each step of the protocol, from the water transfer to the enzyme functionalization, in order to determine the possible aggregation or changing in absorption. Then a fluorescence scan was performed, while exciting the samples at different wavelengths in order to find possible FRET emission peaks or other behavior besides reported emission of nano crystals. Finally, in order to find the effect of the working enzyme on the NPs, emission spectra of conjugated quantum dots/dot-in-rods were acquired for 2 hours, with 5 minutes steps, when they were dissolved in water-based solutions containing fixed glucose concentrations.

6.1 Absorbance measurements

The comparison of NPs absorbance at the different steps of the water-transfer protocol is illustrated in Fig. 6.1. NPs are transferred from toluene to water with the protocols previously illustrated.

Absorbance spectra before and after the phase transfer for polymer coated QDs and for both QRods do not show any significant difference, proving that with this protocol the aggregation is avoided, as also it is reported in literature[22]. The differences in the absorbance height are due to different analyzed concentrations.

Contrariwise, for micellized QDs a broad peak and higher absorption is present, even at wavelength longer than the main excitonic peak. This could be due either to the aggregation of quantum dots with multiple nanocrystals per micelle or to the presence of empty micelles that scatter light.

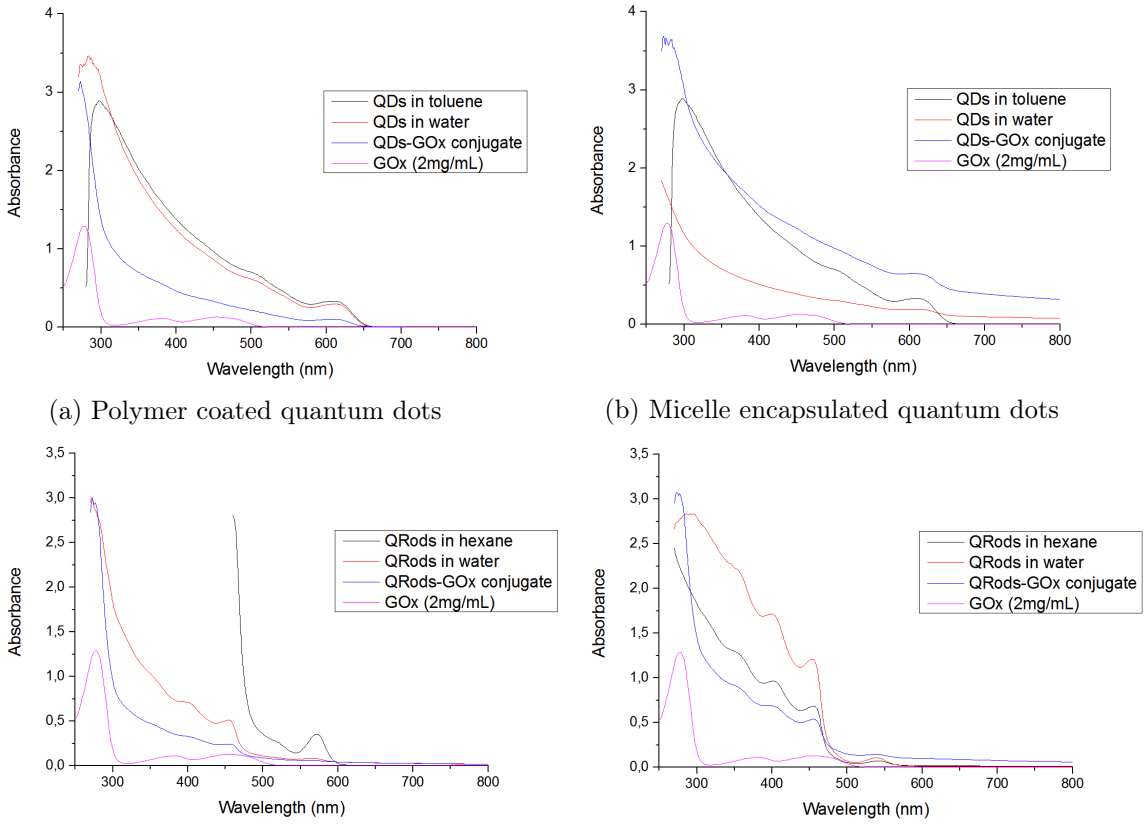

(a) Polymer coated quantum dots

(b) Micelle encapsulated quantum dots

(c) Polymer coated quantum rods

(d) Micelle encapsulated quantum rods

Figure 6.1: Absorbance of NPs in organic solvent (as purchased) compared with water-transferred NPs before and after functionalization. Glucose oxidase absorbance spectrum is also reported.

Absorption spectra are formed by quantum transition peaks with a background due to the continuous absorption of NPs and level splitting (see Chapter 2) [25, 26]. Because of this, the first excitonic peak is always well recognizable, while other exciton peaks result in small bumps on the increasing shoulder of absorbance (while going to shorter wavelengths).

For quantum dot-in-rods, secondary excitonic peaks are more visible. As it can be seen in Fig.5.2d, quantum dot-in-rods consist of a CdSe spherical core, which is preferentially situated at one end of the CdS elongated shell wurtzite structure. The weak absorption peak at longer wavelengths can be attributed to the first excitonic transition of the CdSe core, and it correlates with the fluorescence emission which is related to the band edge transitions. The strong absorption at wavelengths lower than 500 nm can be assigned to CdS shell transitions. This large disparity in absorption intensity is due to the significantly larger CdS shell volume compared to that of the CdSe core [27, 28].

Absorption peaks are summarized in Table 6.1.

In Figure 6.1 glucose oxidase absorbance is reported too. It has three absorption peaks: the main one is at 280 nm and the other two, which have a nearly identical magnitude, are situated at ∼380 nm and ∼450 nm. The spectra were acquired at high concentration (2 mg/mL) due to the optical weak extinction coefficient of the enzyme

QDs absorption peaks [nm]	QRods absorption peaks* [nm]	QRods absorption peaks†[nm]
620, 510, 455	570 (core), 455, 390, 350 (shell)	540 (core), 455, 400, 355 (shell)

Table 6.1: Absoption peaks measured from spectra; *QRods used with polymer coating protocol; †QRods used with micelle encapsulation protocol.

in this region.

After functionalization, NPs change the absorption spectra. A direct comparison of peaks is not possible due to the differences in concentration. However, when looking at the ratio between absorption at 280 nm and the first excitonic peak, an increase of the ratio can be observed, which means that probably functionalization occurred.

6.2 Fluorescence properties

After conjugation with enzymes, fluorescence spectra were acquired. To measure each fluorescence spectrum, 200 μL aliquot of water-based solution containing conjugated NPs was transferred to a well plate and analyzed with the plate reader. Also two reference solutions were analyzed, as previously described in Chapter 5. Solutions were excited at different wavelengths corresponding to absorption peaks of NPs and/or GOx.

Polymer coated QDs

The wavelength chosen were 280 nm, 325 nm, 360 nm, 450 nm, 500 nm and 520 nm. Fluorescence spectra are shown in Fig.6.2.

It is immediately observable that the fluorescence spectra display more than one peak with relative height that changes with excitation. Figure 6.3 shows the peak position for QDs emission calculated with multiple gaussian peak fit. The peak at the highest wavelength ($\sim$635 nm) is the expected fluorescence peak of the quantum dots used (as reported in Sigma Aldrich data sheet, Fig.5.1a).

The peak at the lowest wavelength that appears in the QDs-GOx conjugate solution spectra (Fig.6.2c and 6.2d) matches the fluorescence peak of GOx as shown in Figure 4.4 with a peak wavelength of $\sim$530 nm.

In literature, no evidence is given of fluorescence emission from higher energy quantum dots transitions, but only from the ground level $1S_{3/2}$-$1S_e$. Therefore to understand the nature of the second emission peak at $\sim$ 585 nm and why fluorescence peak of GOx appears with such high intensity only for bio-conjugated QDs and only with low intensity in simple mixtures, fluorescence spectra of glucose oxidase solution and PSMA solution in water were acquired. Glucose oxidase solution was prepared at the same concentration as in mixture and bio-conjugated samples (80 μL 1 mg/mL GOx solution in 0.1M PBS 0.15M NaCl pH 7.4 buffer + 120 μL 0.1M PBS 0.15M NaCl pH 7.4 buffer). The PSMA solution was prepared by transferring the polymer in water starting from 17 mg/mL PSMA dissolved in chloroform and following the same protocol as for QDs. Fluorescence data were acquired with the same gain as for previous fluorescence spectra in order to compare directly the results.

As seen in Fig.6.4, PSMA has no fluorescence peaks in the region investigated, while glucose oxidase at this concentration exhibits weak fluorescence when excited at 360

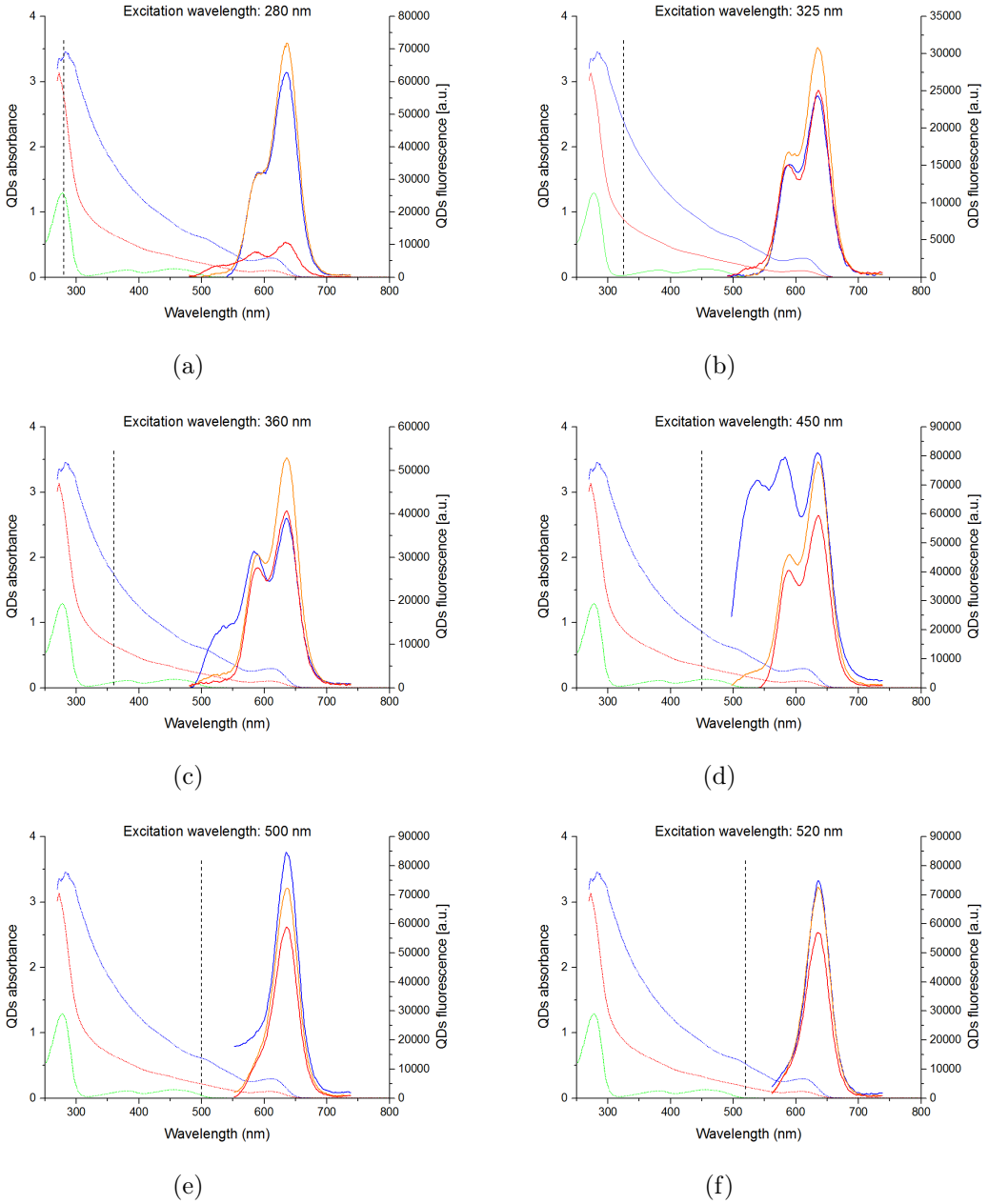

Figure 6.2: Fluorescence of PSMA coated quantum dots at different excitation wavelengths. Legend: QDs-GOx conjugate absorbance (.....) and fluorescence (——); PSMA coated QDs absorbance (.....) and fluorescence (——); 2 mg/mL GOx solution absorbance (.....); QDs and GOx mixture fluorescence (——); excitation wavelength (vertical - - -).

and 450 nm (6.4c and 6.4d). An alternative explanation was found.

Lees *et al.* [22] transferred QDs in water using polymer encapsulation with an increase in quantum yield (QY) up to 125%, while the sample prepared saw its QY drop to less than 1%. This can be explained with the formation of trap sites. Briefly, transfer of charge carriers from the quantum dot core to surface or external trap states via Auger ionization and tunneling are responsible for non the fluorescent dark fractions in the QD population. Ionization makes the QD core charged and non-fluorescent for long periods due to Auger recombination of subsequent electron-hole excitations, a

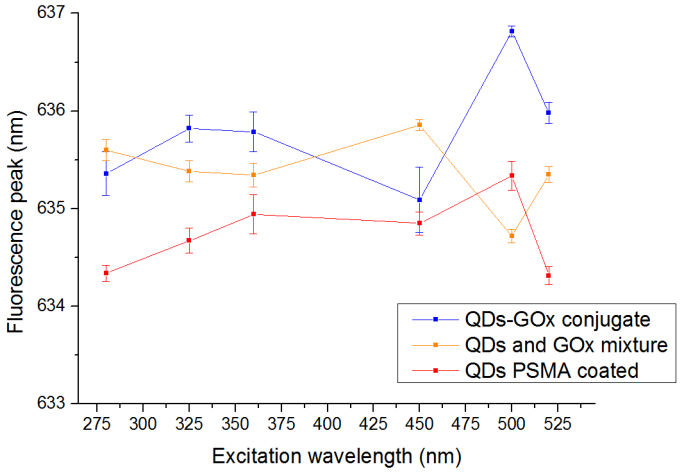

Figure 6.3: Fluorescence peak position in function of different excitation wavelengths for emission peak at longer wavelength.

process made efficient by the high density of states to which the existing (third) carrier can be promoted. The QD switches-on follows neutralization of the core by detrapping and returning of the ionized charge or through the migration of the core charge to the surface capping layer [29]. These phenomena have wide-ranging kinetics and can last for seconds or minutes, which is an exceptionally long time compared to normal fluorescence lifetimes (nanoseconds to microseconds) [30]. Fluorescent emission from surface trap sites of energy higher than the usual fluorescence peak have been reported for CdSe/ZnS core-shell quantum dots [31, 32]. In Fig.6.5 an example scheme of energy surface traps is sketched. The peak at ∼585 nm (2.12 eV) is compatible with the range of energy of these defects, nevertheless further investigation are required.

GOx emission observations agree with the fluorescence of simple mixtures because GOx emits mainly when excited at 450 nm, but with intensity much lower than quantum dots. High intensity GOx emissions (comparable with the QDs one) found in bio-conjugated samples need deeper explanation.

Föster Resonance Energy Transfer (FRET) cannot explain this phenomenon because it needs overlap between donor emission and acceptor absorption and this is not the case. As previously explained, the possible presence of high energy surface traps may lead to energy transfer to the enzyme via non radiative relaxation. Also here, further investigations are required because this type of mechanisms has never been reported in literature.

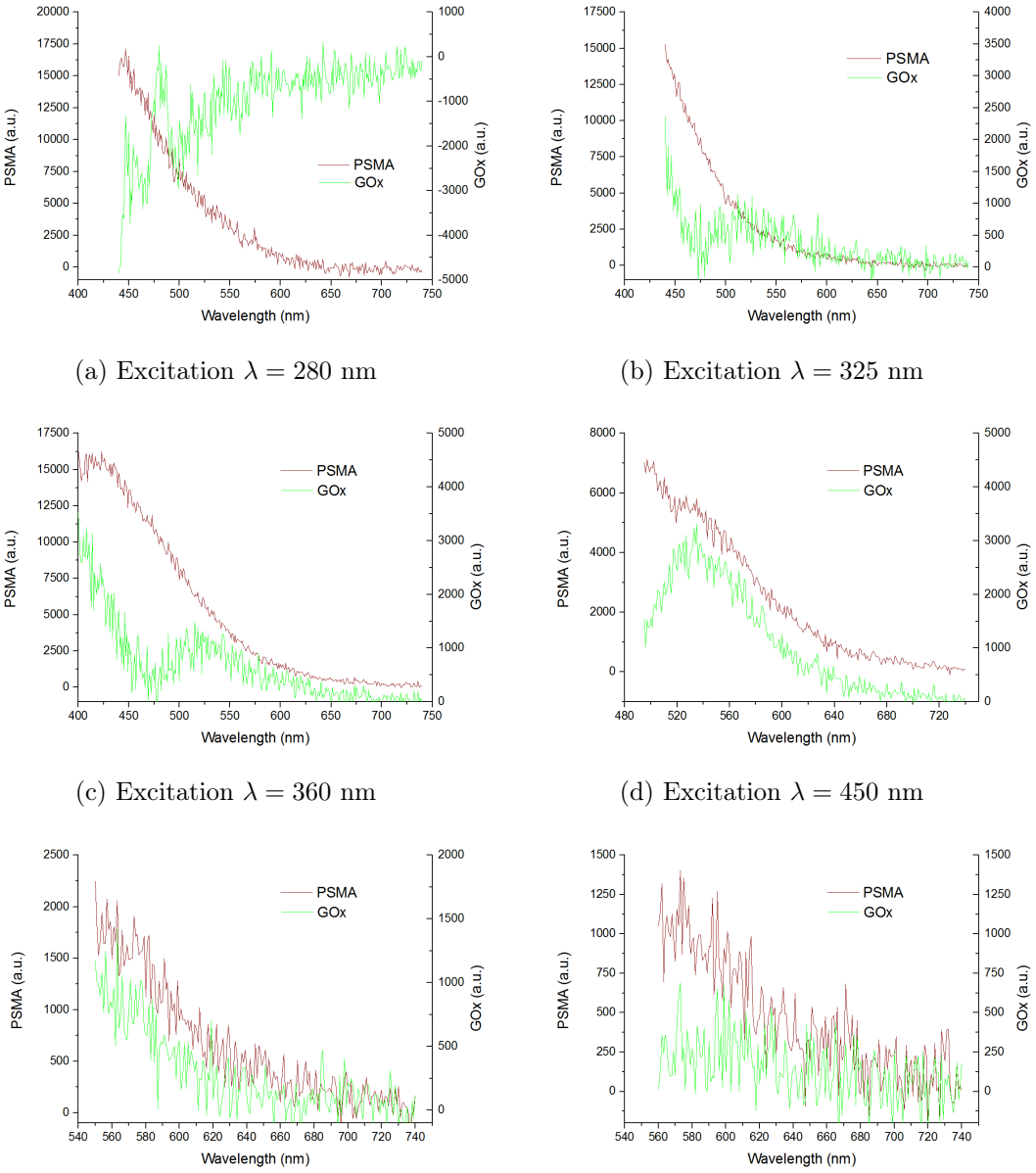

(a) Excitation $\lambda = 280$ nm

(b) Excitation $\lambda = 325$ nm

(c) Excitation $\lambda = 360$ nm

(d) Excitation $\lambda = 450$ nm

(e) Excitation $\lambda = 500$ nm

(f) Excitation $\lambda = 520$ nm

Figure 6.4: Fluorescence of PSMA and GOx solutions in water at different excitation wavelengths.

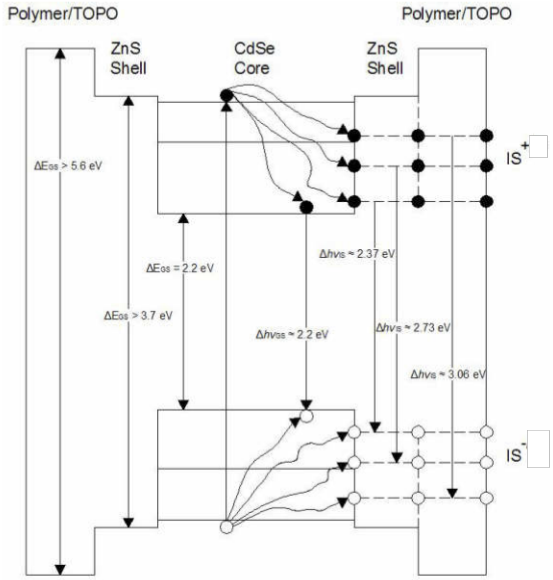

Figure 6.5: The energy diagram of CdSe/ZnS core/shell QDs. Symbols IS^+ and IS^- represent the charge of donor-like and acceptor-like interface states, respectively. Dashed lines show the ways of carrier tunneling from the CdSe/ZnS interface toward the ZnS/TOPO/polymer interface [32].

Micelle encapsulated QDs

Excitation wavelengths chosen were 280 nm, 325 nm, 360 nm, 450 nm, 500 nm and 520 nm. Neither second emission peak nor enzyme emission peak were found.

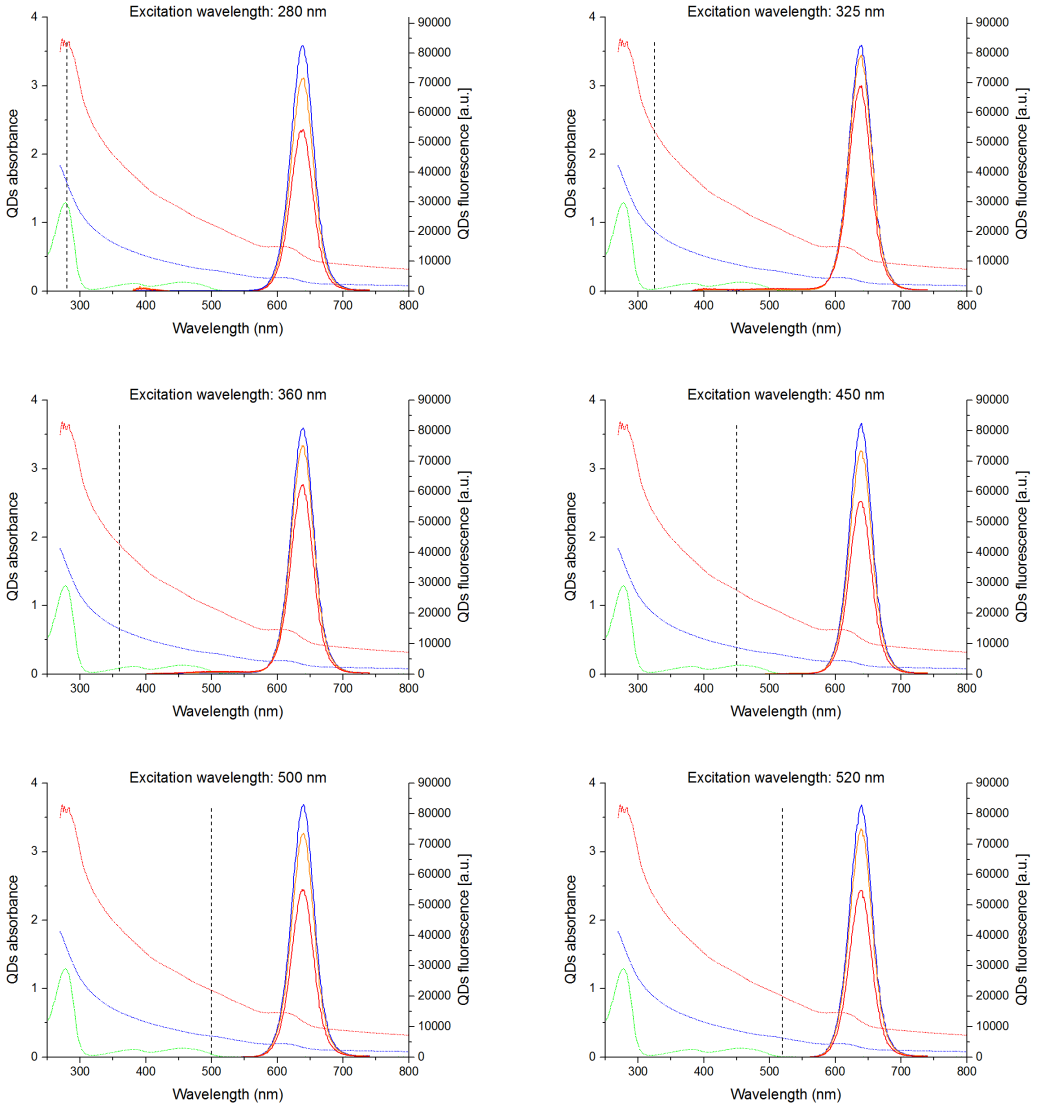

Figure 6.6: Fluorescence of DSPE-PEG-COOH encapsulated quantum dots at different excitation wavelengths. Legend: QDs-GOx conjugate absorbance (.....) and fluorescence (——); DSPE-PEG-COOH encapsulated QDs absorbance (.....) and fluorescence (——); 2 mg/mL GOx solution absorbance (.....); QDs and GOx mixture fluorescence (——); excitation wavelength (vertical - - -).

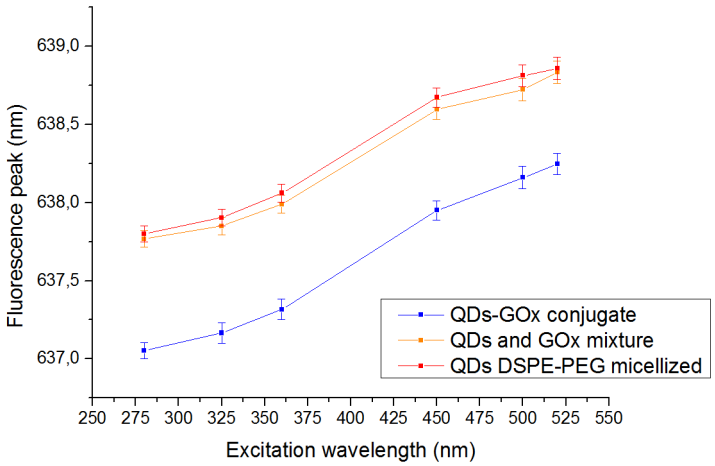

Figure 6.7: Fluorescence peak position at different excitation wavelengths.

Polymer coated QRods

Samples were excited at 280 nm, 325 nm, 360 nm and 455 nm.

CdSe/CdS dot-in-rod structures have a type-I band offset for both electrons and holes to be confined inside the core, however these particles may exhibit a type-II behavior, caused by a spatial charge separation of excited carriers within the particle. This intriguing duality can be attributed to the small conduction band offset between CdSe and CdS, and to quantum size effects which are governed by the system's dimensions. For example, in systems with very small core diameters, due to the quantum size effect the energy of the first electronic state of the CdSe core can go over the conduction band offset and into the CdS conduction band. This leads to the formation of a combined CdSe/CdS electronic state, in which the electron wave function spreads along the rod, while the hole is confined to the core, as shown in Figure 6.10. The generally reported energy gap between conduction band for type-I dot-in-rod is $\Delta E \simeq 0.3eV$, while for quasi type-II it's $\Delta E \simeq 0eV$ [33, 27, 34].

As a result, despite their type-I potential profile, such nanoparticles will exhibit an effective charge separation and type-II behaviour, and thus are often referred to as quasi type-II particles. According to previous studies, the CdSe/CdS dot-in-rod system exhibits type-I behaviour when the core size is larger than ~ 2.8 nm [33]; otherwise, it behaves like a quasi type-II quantum dot. However, the exact point for the cross over between the two behaviours can be strongly influenced by the rod dimensions and also by the synthesis parameters. Indeed, quasi type-II behaviors have been observed for 4 nm diameter core dot-in-rod [34].

Particles used have a core size of 4-4.3 nm diameter, therefore behaviour of the system should be type-I.

To extract the peak positions, curves were fitted with skewed (asymmetric) gaussians represented by the equation (6.2.1)

$$f(x) = \frac{2}{\omega}\phi\left(\frac{x-\xi}{\omega}\right)\Phi\left(\alpha\frac{x-\xi}{\omega}\right) \tag{6.2.1}$$

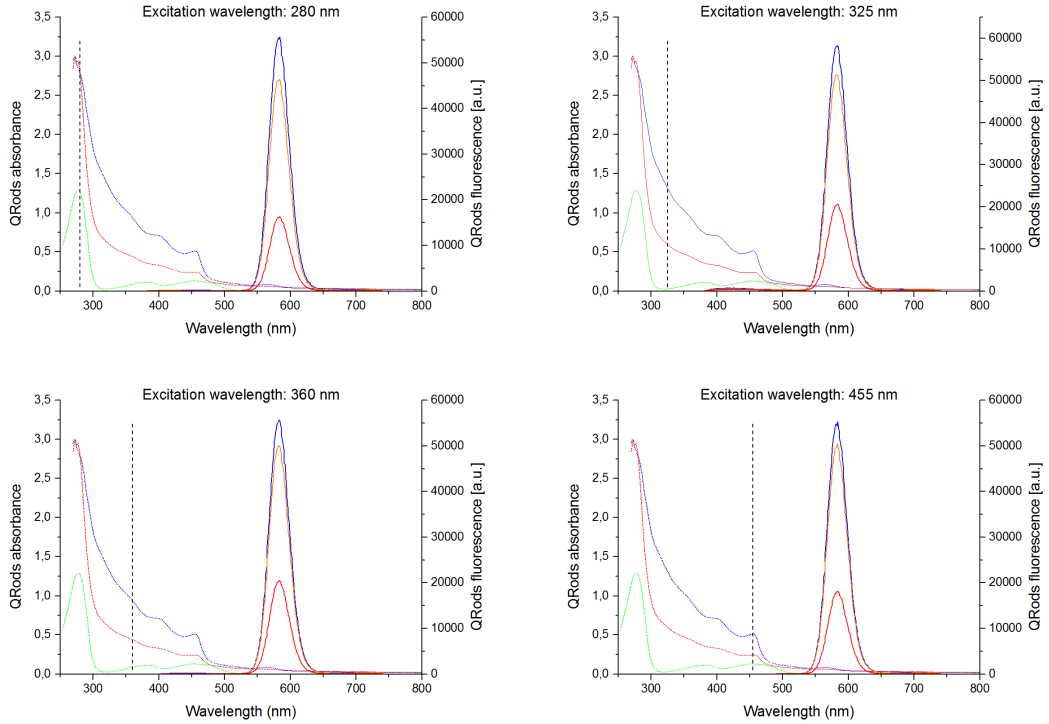

Figure 6.8: Fluorescence of PSMA coated quantum rods at different excitation wavelengths. Legend: QRods-GOx conjugate absorbance (.....) and fluorescence (——); PSMA coated QRods absorbance (.....) and fluorescence (——); 2 mg/mL GOx solution absorbance (.....); QRods and GOx mixture fluorescence (——); excitation wavelength (vertical - - -).

where

$$\phi(x) = \frac{1}{\sqrt{2\pi}} e^{-\frac{x^2}{2}} \tag{6.2.2}$$

is the normal distribution and

$$\Phi(x) = \int_{-\infty}^{x} \phi(t)dt = \frac{1}{2}\left[1 + \text{erf}\left(\frac{x}{\sqrt{2}}\right)\right] \tag{6.2.3}$$

is the cumulative distribution function, and erf is the error function. In (6.2.1) α determines the shape of the gaussian: the distribution is right skewed if $\alpha > 0$ and left skewed if $\alpha < 0$; the normal distribution is recovered when $\alpha = 0$. ξ is called location while ω is the scale.

From fit parameters we can then estimate the emission mean and variance as:

$$\text{Mean} = \xi + \omega\delta\sqrt{\frac{2}{\pi}} \text{ where } \delta = \frac{\alpha}{\sqrt{1+\alpha^2}} \tag{6.2.4}$$

$$\text{Variance} = \omega^2\left(1 - \frac{2\delta^2}{\pi}\right) \tag{6.2.5}$$

The origin of this asymmetry towards red wavelengths of emission spectra can be due to Quantum Confined Stark Effect (QCSE). The location of surface charges on the elongated particles defines the electron-hole wave functions overlap through the quantum confined Stark effect (QCSE) and it leads to a shift of the fluorescence peak position. Spatial oscillations of surface charges give rise to spectral line broadening

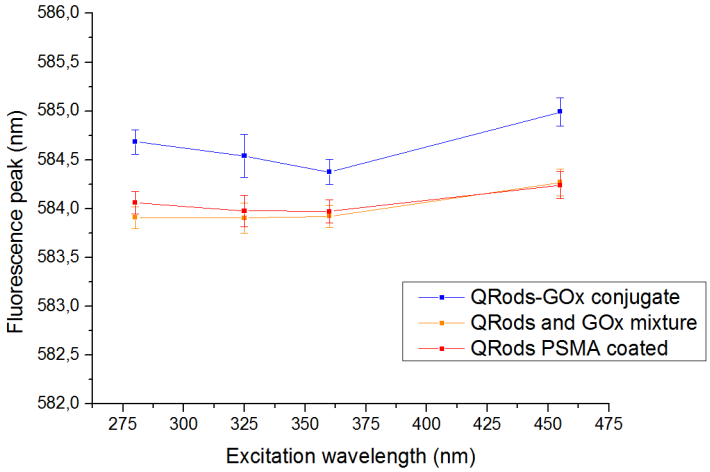

Figure 6.9: Fluorescence peak position at different excitation wavelengths.

strongly dependent on the spatial position of charges on the NC surface. Müller and co-workers [35] found a redshift of the emission peak of about 2.5 nm and a broadening of the FWHM when a negative charge (trapped on the surface of CdS shell) oscillates in close proximity of the core, compared to their values in fluorescent spectra when the same charge oscillates on the opposite end of the rod. Effective electric field is reciprocal to the charge motion, therefore the QCSE shift is nonlinear in charge position. Assuming an uniform distribution of charges on the rod surface, they causes different redshift in emission. For this reason the emission peak width is wider for red-shifted wavelengths.

Only one emission peak was found, with constant emission wavelength (Fig. 6.9).

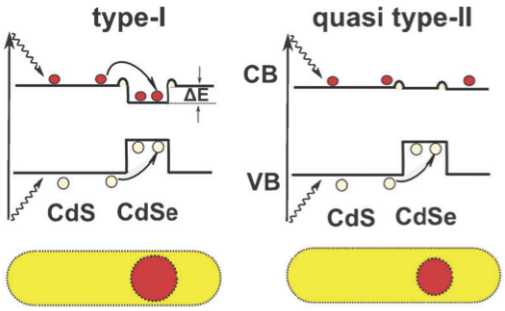

Figure 6.10: Energy band alignment of CdSe/CdS dot-in-rod with type-I and quasi type-II structures. In type-I both electrons and holes are confined inside the core. In quasi type-II electron wave function spreads along the rod while the hole is mostly confined to the core. The electron delocalization typically decreases wave function overlapping of electron and hole [27].

Micelle encapsulated QRods

Fluorescence measurements were obtained by exciting rods at 280 nm, 325 nm, 360 nm, 410 nm and 455 nm. The quantum dot-in-rods used have a core diameter of 3-3.5

nm, therefore the behaviour of the system is more in between type-I and quasi type-II.

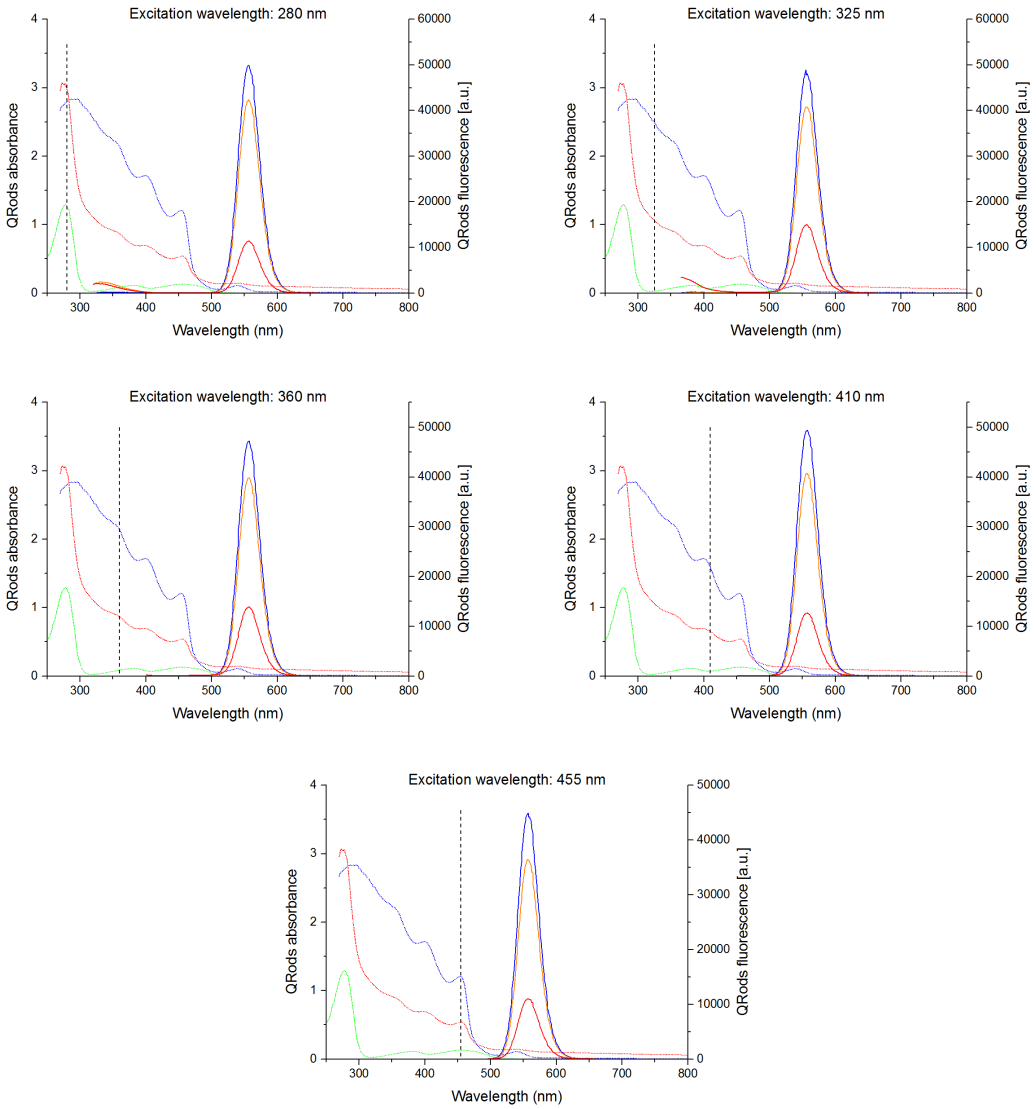

Figure 6.11: Fluorescence of DSPE-PEG-COOH encapsulated quantum rods at different excitation wavelengths. Legend: QRods-GOx conjugate absorbance (.....) and fluorescence (——); PSMA coated QRods absorbance (.....) and fluorescence (——); 2 mg/mL GOx solution absorbance (.....); QRods and GOx mixture fluorescence (——); excitation wavelength (vertical - - -).

Peak wavelength is almost stable for different excitation wavelengths (Fig.6.12).

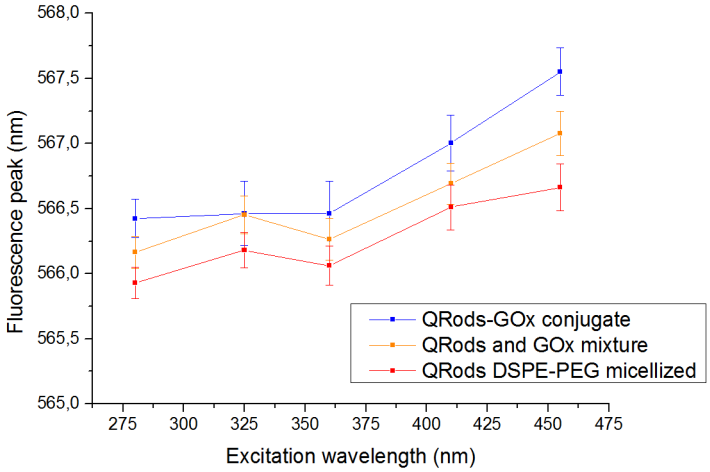

Figure 6.12: Fluorescence emission peak varying excitation wavelengths.

6.3 Effects of enzyme activity

The main effect of the enzymatic activity is the quenching of photoluminescence (Fig: 6.15, 6.17, 6.19 and 6.20). As previously described in Chapter 4, glucose oxidase catalyzes the oxidation of glucose and releases H_2O_2 and gluconolactone. The latter is then rapidly hydrolyzed to form D-gluconic acid and, as a consequence, lowers the pH of the solution. The catalytic reactions can be summarized below as:

$$\begin{aligned} &\text{D-glucose} + O_2 \xrightarrow{\text{GOx}} \text{D-gluconolactone} + H_2O_2 \\ &\text{D-gluconolactone} + H_2O \rightarrow \text{D-gluconic acid.} \end{aligned} \tag{6.3.1}$$

As reported by Cao *et al.* for CdTe QDs [36], by Wu *et al.* for Mn-dopped ZnS QDs [37] and by Cavaliere-Jaricot *et al.* [38], the mechanism that stimulates the decrease in the fluorescence of QDs-GOx is based on an electron-transfer reaction that occurs on the surface of quantum dots. When H_2O_2 gets to the surface of the QDs, a chemical oxidation of sulfur atoms occurs:

$$S^{2-}_{\text{surface}} + H_2O_2 \rightarrow S^{-\bullet}_{\text{surface}} + OH^{\bullet} + OH^{-} \tag{6.3.2}$$

The formed $OH^{\bullet}$ radical is able to inject a hole (6.3.3) in the $1S_h$ quantum-confined orbital of the CdSe core [39]:

$$OH^{\bullet} + \text{CdSe/ZnS} \rightarrow OH^{-} + \text{CdSe}(h^{+}_{1S_h})/\text{ZnS}. \tag{6.3.3}$$

Through this charge carrier injection, very fast non radiative Auger channels for any excited electron-hole pair are generated. As a result, while these charges are present, radiative luminescence is quenched.

Alternatively, the $OH^{\bullet}$ radical can react with an H_2O_2 molecule yielding a superoxide ion:

$$OH^{\bullet} + H_2O_2 \rightarrow H_2O + HO^{\bullet}_2 \tag{6.3.4}$$

$$HO^{\bullet}_2 + OH^{-} \rightarrow O^{-}_2 + H_2O \tag{6.3.5}$$

The superoxide ions are quite stable in aqueous solution, especially at high pH, and their lifetime is approximately 1 min. They can easily donate one electron in the

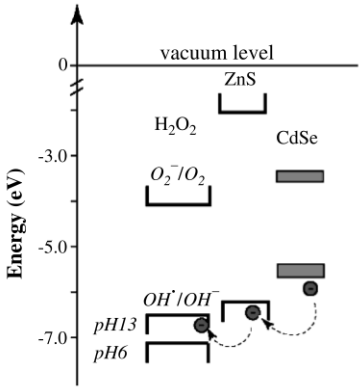

Figure 6.13: Energy level diagram for CdSe/ZnS quantum dots and H_2O_2 [38].

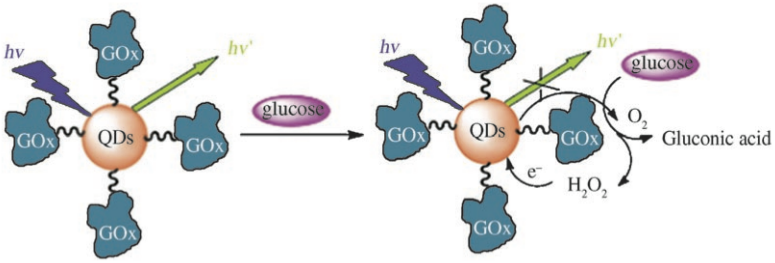

Figure 6.14: A schematic illustration of QDs-GOx complex glucose sensing principles.

reaction $O_2^- \rightarrow O_2 + e$ and inject an electron from the superoxide ion in a surface or core hole of the excited quantum dot via non-radiative recombination (6.3.6). This avoids the recombination and leads to the formation of a non-fluorescent QD anion.

$$O_2^- + \text{CdSe/ZnS} \rightarrow \text{CdSe}(e^-_{1S_e})/\text{ZnS} + O_2 \tag{6.3.6}$$

The energy levels for the described reaction are schetched in Fig 6.13

The O_2 produced can participate further in the reaction catalyzed by GOx, forming a cyclic mechanism of glucose oxidation, which is favorable for the whole reaction system (Fig 6.14).

In order to study the effect of enzymatic activity on nanoparticles, aliquot solutions containing quantum dots/rods were mixed with glucose solutions. To prove that hydrogen peroxide is actually the fluorescence quencher, unconjugated particles were mixed with H_2O_2 and glucose. For more details see Chapter 5.

The excitation wavelength used was 450 nm. Spectra were acquired for 2 hours every 5 minutes.

Polymer coated QDs

In the samples prepared during this project, a stronger quenching at higher concentrations of glucose is obtained, which means a higher production of hydrogen peroxide. Moreover, in Fig.6.15a a strong quenching of non functionalized quantum dots photoluminescence in 1mM H_2O_2 solution can be observed at the initial time. This confirms that hydrogen peroxide is the quenching agent. For non functionalized quantum dots

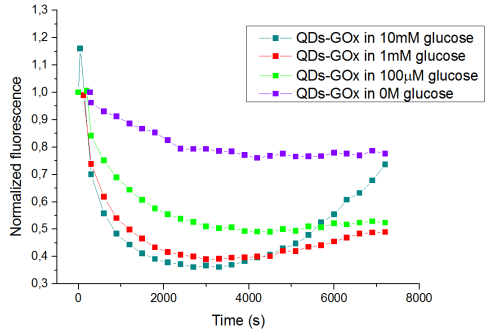

(a) Quenching with enzymatic activity

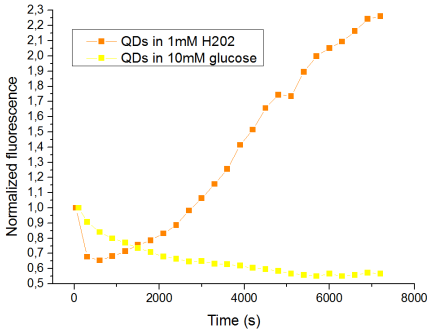

(b) Quenching with reference solutions

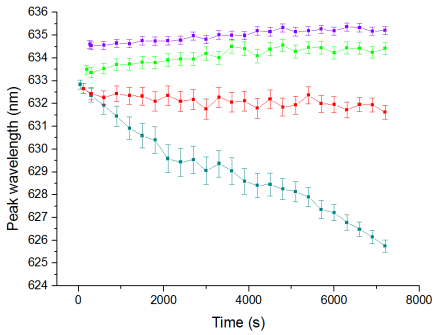

(c) Wavelength shift

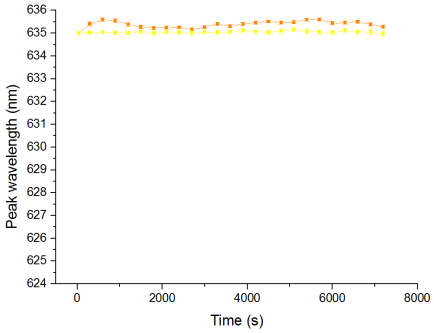

(d) Wavelength shift with reference solutions

Figure 6.15: Fluorescence intensity and wavelength for QDs peak with different glucose concentrations (a,c) and for reference solutions (b,d).

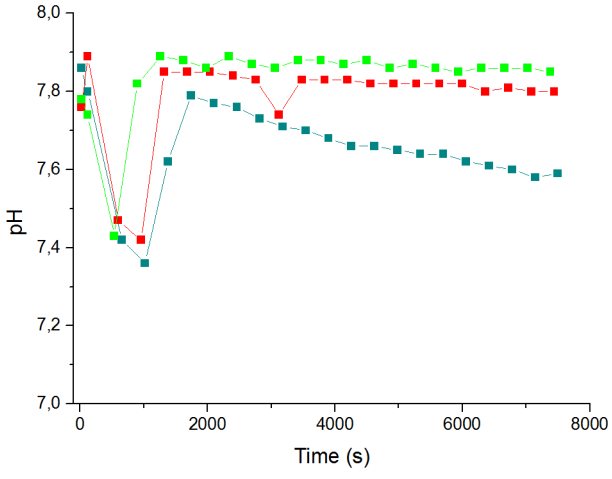

Figure 6.16: pH of QDs-GOx conjugate in glucose solutions 10mM(—■—), 1mM (—■—) and 100 μM (—■—).

in 10mM glucose solution (Fig.6.15a) we can see an unusual quenching, with final intensity of $\sim$ 60% of the initial value, while for QDs-GOx without glucose (Fig.6.15b)

we obtain a final intensity of $\sim 80\%$. Since glucose is reported to be neutral to the presence of quantum dots, this behaviour needs further investigations.

Two other phenomena are involved in quantum dot photoluminescence: photo bleaching and photo brightening. Experiments performed by van Stark and co-workers [40, 41, 42] showed fast photobleaching of QDs under O_2 flow while slower decay in photoluminescence was observed under N_2 flow. Photo-induced oxidation and production of $CdSeO_2$ and $CdSeO_3$ at the CdSe core have been reported [29] and this causes the formation of quenching states.The formation of surface quenching states causes a decrease in the number of photons emitted. However, photooxidation causes also a reduction of the core size and a consequent blue-shift of the wavelength. Regarding our samples, photobleaching occurs without a change in emission wavelengths as seen in Fig. 6.15a for QDs-GOx conjugate in solution without glucose and in Fig. 6.15b for QDs in H_2O_2 and glucose solutions. As reported by van Stark *et al.* quantum dots bleaching is also observed in nitrogen, where blue-shift is absent. It is therefore more likely that the intensity decrease and bleaching are caused by the formation of lattice defects in the QDs, thereby creating additional non-radiative recombination pathways. The nature of these photo-induced quenching states is not clear. Possibly a high-energy biexciton state in a single dot has enough energy to rearrange or break bond at the CdSe/ZnS interface, which gives rise to additional non radiative recombination channels [42].

Photo brightening is related to photo bleaching because it involves the same processeses and it is caused by the same factors. Brightening has been studied for CdSe and CdSe/ZnS quantum dots by Jones *et al.* [43] and Zhelev and co-workers [44]. The effect of irradiation on the photoluminescence intensity of QDs could be due to a multitude of factors: (1) improvement of surface passivation and/or changes in the structure of crystal lattice (process that competes with defects formation due to energy deposition, as explained before), (2) dark dots may be induced to start fluorescing again via thermalization of trapped electron-hole back to a fluorescent state, (3) oxygen passivation of nanocrystal surface [45]. The authors have supposed that the formation of surface oxides passivates the surface states that are not blocked by the capping agent, which results in emission enhancement. We observed a brightening of luminescence for QDs exposed to hydrogen peroxide and acid environment. As described above, the degradation of H_2O_2 causes a production of O_2 directly on the QDs surface. This can passivate better the surfaces and, in collaboration with light remove, it can trapped electrons and holes caused by H_2O_2 quenching mechanism and restore part of the fluorescence. We have to take into account also the effect of pH which, as described later, etches the surface of quantum dots and can remove dislocation and lattice mismatch. Nevertheless, these explanations are rather speculative and further verifications are required.

Another factor that strongly influences quantum dots emission peak and intensity is pH. In literature we can find many studies conducted on different types of quantum dots. Different QD behavior have been reported when lowering the solution's pH: decreasing of photoluminescence and blueshift for CdSe/ZnS QDs [46, 47] and for CdSe/ZnSe/ZnS core/shell/shell QDs [48], lowering in photoluminescence without blue shifting for the same type of core/shell QDs [49], decreasing in fluorescence with redshift for CdTe/ZnS core/shell [50], CdTe/CdSe core/shell [51] and for CdTe quantum dots [52]. Our samples present blueshift of the QDs-GOx conjugate emission peak, with stronger lowering of emission wavelength for higher glucose concentrations (Fig. 6.15c). The pH of the solutions (Fig. 6.16), as expected, lowers for higher glucose concentrations. By com-

paring the observation on the pH with the solution emission peak (Fig. 6.15d), it is clear that the blue-shift is due to gluconic acid production rather to the presence of H_2O_2.

It is safe to assume that the passivating layer of the QDs can be easily penetrated by H^+ and O_2. ZnS is strangley thermodynamically stable under normal conditions; the dissociation of ZnS directly into Zn^{2+} and S^{2-} has a $\Delta G = +139.4\,kJ\,mol^{-1}$. However, in the presence of acid and oxygen, the reaction [49]

$$ZnS_{(s)} + 2H^+_{(aq)} + \frac{1}{2}O_{2(aq)} \rightarrow S_{(s)} + ZnS^{2+}_{(aq)} + H_2O_{(l)} \tag{6.3.7}$$

has a $\Delta G = -81\,kJ\,mol^{-1}$, and a relatively low activation energy, $E_a = 25\,kJ\,mol^{-1}$. Also oxidation of $S_{(s)}$ to $SO_{2(g)}$ is thermodynamically allowed ($\Delta G_f(SO_2) = -300.1\,kJ\,mol^{-1}$) however it is very slow and may eventually dissolve in water to form bisulfite and sulfite following the reactions:

$$S_{(s)} + O_{2(aq)} \rightarrow SO_{2(g)} \tag{6.3.8}$$

$$SO_{2(g)} + H_2O_{(l)} \rightarrow HSO^-_{3(aq)} + H^+_{(aq)} \overset{pK_a\ 7.0}{\Longleftrightarrow} SO^{2-}_{3(aq)} + 2H^+_{(aq)} \tag{6.3.9}$$

Thus, over extended periods of time, sections of the shell can decompose in the presence of acid and oxygen. Furthermore, the rates of all these reactions will be accelerated under illumination.

Durisic *et al.* postulated that the ZnS shell may be exposed to slow decomposition with the reaction showed above, exposing the CdSe core in regions where the shell is particularly thin. This exposes the core to etching and/or photooxidation, which reduces core size and shifts emission peak to bigger energy.

Dissociated Zn^{2+} and H^+ ions interaction with shell surface can also play a role in the trapping of charge carriers, inhibiting fluorescence. Quenching of QDs-GOx conjugates photoluminescence in glucose solution cannot be attributed only to hydrogen peroxide, and probably also pH plays an important role on it.

Micelle encapsulated QDs

As can be seen in Fig. 6.17a, micellized QDs present low photobleaching (for QDs-GOx conjugate in solution without glucose, luminescence after 2h is more than 90% of the initial value), and quenching of luminescence due to enzyme works as expected (more quenching for 10 mM glucose solution, then 1 mM glucose and last 100 μM). Only for conjugated quantum dots in 10 mM glucose solution a recovery in fluorescence happened during the 4000 seconds after the glucose injection.

Reference solutions (Fig. 6.17b) showed quenching in fluorescence in the presence of hydrogen peroxide solution (demonstrating again that it is one of the quenching agent of the system), while almost no fluorescence inhibition was observed for QDs in the presence of glucose.

By analysing emission wavelength shift (Fig. 6.17c), we can see a higher shift for QDs-GOx conjugate in the presence of a higher glucose concentration solution, confirming the etching effect of acid/hydrogen peroxide. For this type of QDs, a shift in the emission wavelength is also reported upon addition of hydrogen peroxide (Fig. 6.17d).

The pH of solutions of the conjugate and of QDs reference solutions is displayed in Fig. 6.18 for comparison. As for PSMA coated quantum dots (Fig. 6.16) we can see more decrease in pH in the presence of more glucose, which means that more gluconic acid is produced. For these QDs (not conjugated) the pH of the reference solution

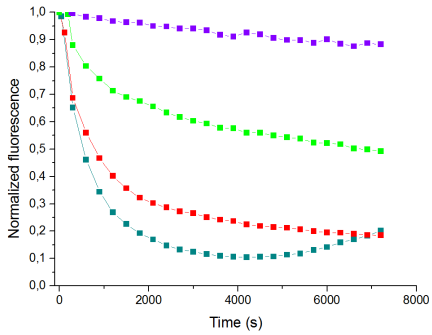

(a) Quenching with enzymatic activity

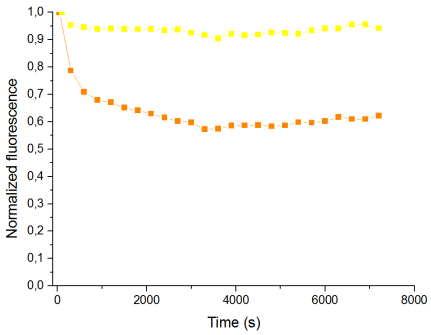

(b) Quenching with reference solutions

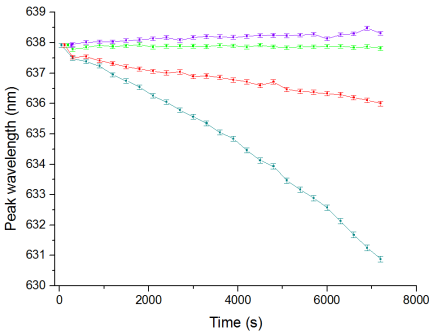

(c) Wavelength shift

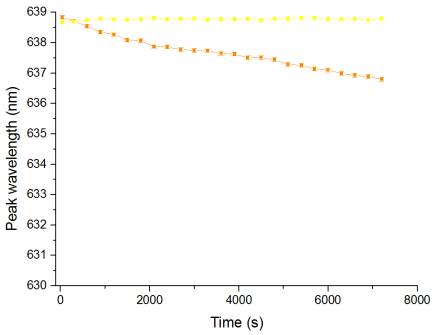

(d) Wavelength shift with reference solutions

Figure 6.17: Fluorescence intensity and wavelength for QD peak with different glucose concentrations (a,c) and for reference solution (b,d). Legend: QDs-GOx conjugate glucose solution 10 mM (—■—), 1 mM (—■—), 100 μM (—■—) and 0 M (—■—); micellized unconjugated QDs in 1 mM H_2O_2 (—■—) and in 10 mM glucose solution (—■—)

was measured, revealing, after an initial fast decreasing and recovery, present also in conjugate data, stability over 2 hours of measurments.

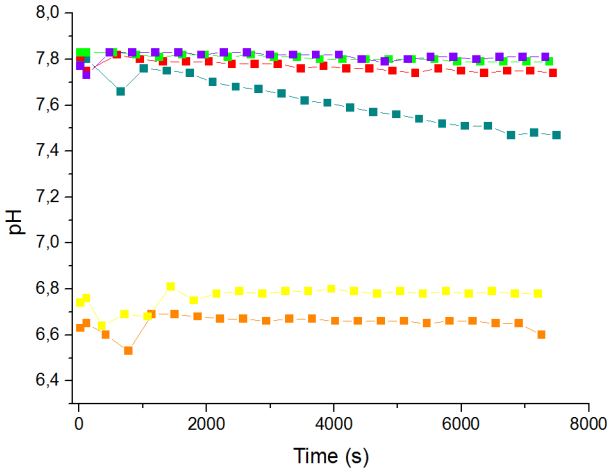

Figure 6.18: pH of QDs-GOx conjugates in glucose solutions 10 mM (—■—), 1 mM (—■—), 100 μM (—■—) and 0 M (—■—); micellized QDs not conjugate in 1 mM H_2O_2 (—■—) and in 10 mM glucose solution (—■—)

Polymer coated QRods

As seen for quantum dots, the complex behaviour emerging from the dependence of the fluorescence intensity is governed by several different mechanisms of carrier relaxation. These mechanisms include radiative recombination, Auger nonradiative scattering, thermal escape from the dot as well as trapping in surface states and/or defect states. Upon absorption of incident photons at 450 nm by the CdS rod, hot carriers are generated and quickly relax to lower band-edge states. In the radiative decay path, the photo-generated carriers then diffuse to the CdSe dot, where the exciton recombines to emit a photon. The overall fluorescence intensity depends on the number of the carriers captured in the dot.

For elongated shell dot-in-rod the photo-generated carriers can diffuse inside the CdS rod (especially for quasi type-II), they can be trapped by surface/defect states in the rod and could recombine nonradiatively, resulting in a decrease in the intensity. For type-I dot-in-rod with ~0.3 eV potential barrier (*i.e.* structure with core size >2.8 nm, like for used nano crystals) Wen *et al.* [27] estimated a potential barrier of 556.7 ± 68 meV for electrons to escape from the core and nonradiatively recombine in traps. If we consider an energy gap between excitation energy ($\lambda_{ex} = 450\,nm \equiv 2.755\,eV$) and emission peak ($\lambda_{em} = 585\,nm \equiv 2.120\,eV$) of 655 meV, electrons have enough energy to overcome the activation barrier and diffuse in the shell.

This piece of information can be used to explain the results presented in Figure 6.19a, *i.e.* a higher photobleaching and no distinction between 10 mM and 1 mM glucose solutions. Indeed, rod-shape shell have a higher surface exposed to the external environment and a higher volume as compared to the spherical ZnS shell of quantum dots: this may result in higher trap number and interaction probability.

The redshift plotted in figure 6.19c and 6.19d can be explained with the increasing number of charges trapped on the surface that can enhance the quantum confined Stark effect.

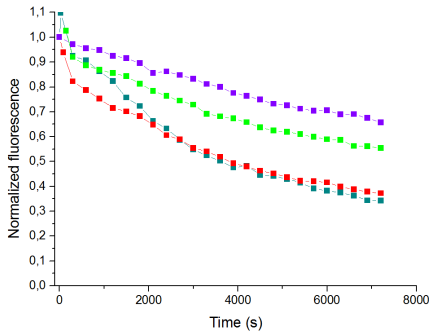

(a) Quenching with enzymatic activity

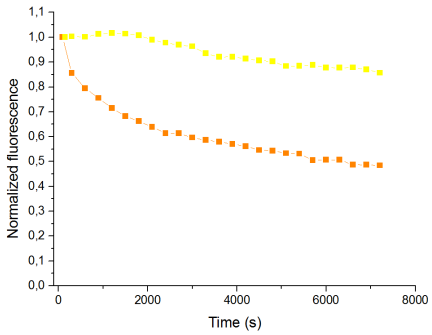

(b) Quenching with reference solutions

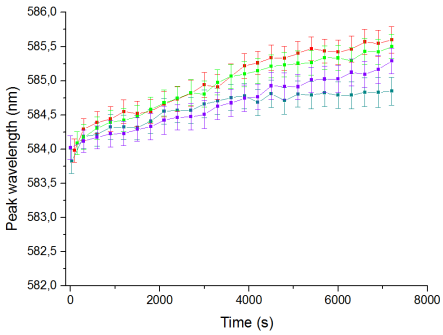

(c) Wavelength shift

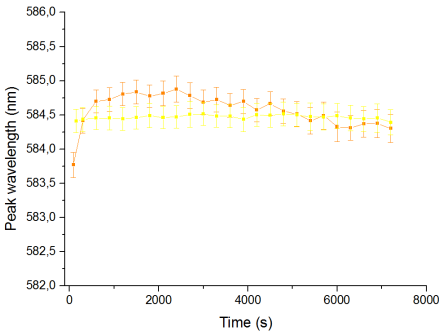

(d) Wavelength shift with reference solutions

Figure 6.19: Fluorescence intensity and wavelength for QRods peak with different glucose concentrations (a,c) and for reference solutions (b,d). Legend: QDs-GOx conjugate glucose solution 10 mM (—■—), 1 mM (—■—), 100 μM (—■—) and 0 M (—■—); micellized QDs not congugate in 1 mM H_2O_2 (—■—) and in 10 mM glucose solution (—■—)

Micelle encapsulated QRods

Quenching of photoluminescence is strong, and makes impossible to distinguish between the effect of different glucose concentrations (Fig.6.20a).

Wavelength shift has the same small blueshift present also for PSMA coated dot-in-rod (Fig.6.20c and 6.20d)

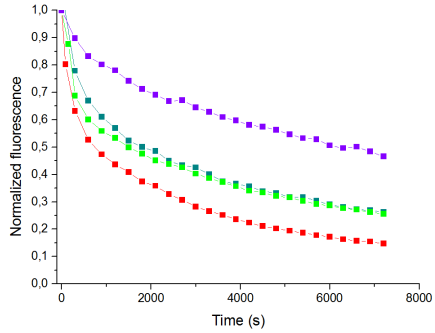

(a) Quenching with enzymatic activity

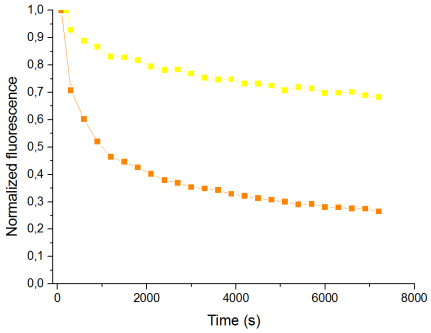

(b) Quenching with reference solutions

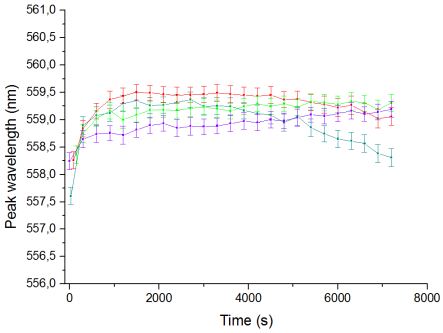

(c) Wavelength shift

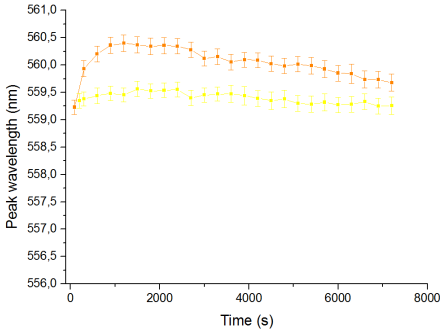

(d) Wavelength shift with reference solutions

Figure 6.20: Fluorescence intensity and wavelength for QRods peak with different glucose concentrations (a,c) and for reference solutions (b,d). Legend: QDs-GOx conjugate glucose solution 10 mM (—■—), 1 mM (—■—), 100 μM (—■—) and 0 M (—■—); micellized QDs not congugate in 1 mM H_2O_2 (—■—) and in 10 mM glucose solution (—■—)

6.4 Enzymatic activity

An important parameter than can be estimated for processes involving enzymes is the enzymatic activity.

Kinetic activity of enzymes is described by the Michaelis-Menten theory. It takes the form of an equation describing the rate of enzymatic reactions, by relating reaction rate v to $[S]$, which represents the concentration of a substrate S (glucose in our experiments). Its formula is the following:

$$v = \frac{d[P]}{dt} = \frac{V_{max}[S]}{K_m + [S]} \tag{6.4.1}$$

where $[P]$ is the product concentration, V_{max} represents the maximum rate achieved by the system, at maximum (saturating) substrate concentrations. The Michaelis constant K_m is the substrate concentration at which the reaction rate is half of V_{max}; the smaller value of K_m indicates the increased affinity of enzyme for the substrate.

Michaelis-Menten kinetic parameters are estimated using Lineweaver-Burk plot, which is the graph of the inverse of enzyme activity (quenching in fluorescence) versus the inverse of glucose concentration:

$$\frac{1}{v} = \frac{K_m}{V_{max}}\frac{1}{[S]} + \frac{1}{V_{max}} \tag{6.4.2}$$

Nanomaterials	Detection scheme	K_m (mM)	Detection range (mM)	Refs
AuNPs	spectrophotometry	3.74		[53]
CdSe/ZnS QDs	fluorescence		0.2 - 30	[46]
SiO_2@CdSe/ZnS QDs	fluorescence		0.5 - 3	[38]
AuNPs-SiO_2@QDs	cyclic voltagrams		2 - 25	[38]
CdTe QDs	fluorescence	0.45	0.005 - 1	[36]
CdTe QDs-benzyme	fluorescence		0.001 - 1	[54]
Mn-dopped ZnS QDs	phosphorescence	0.7	0.01 - 10	[37]
CdSe/ZnS QDs	fluorescence	0.18	<1	this work
Free GOx		5.85		[53]

Table 6.2: Comparison of the performance of various nanosystem for glucose sensing

The enzymatic activity of GOx assembled on nanoparticles was investigated by monitoring the decrease in fluorescence intensity during oxidation of glucose. Since GOx catalyzes the oxidation of glucose and produces H_2O_2, it is expected that for a given enzymatic activity, the rate of H_2O_2 production would increase as the glucose concentration increases. So the extent of fluorescence quenching embodies the changes of GOx enzymatic activity. In addition, as the biocatalytic reaction proceeds, the luminescence quenching of QDs/QRods-GOx is enhanced, in accordance with the theory proposed previously. In the experiment, enzymatic activities are estimated for a fixed reaction time of fifteen minutes.

As previously reported, QRods did not display a good sensibility to glucose, *i.e.* more quenching in fluorescence for MPs mixed with higher concentration glucose solutions. For this reason, enzymatic parameters were calculated only for quantum dots.

QD samples enzymatic-substrate affinity estimation using Lineweaver-Burk fit gives $K_m = 0.088 \pm 0.007$ mM for polymer coated and $K_m = 0.18 \pm 0.01$ mM for micelle encapsulated QDs. In Table 6.2 our results are compared with results reported in literature, showing a significant increase in the enzyme substrate affinity due to the functionalization process. However, more significant results could be obtained with more points, *i.e.* analyzing quenching effects with more glucose solutions.

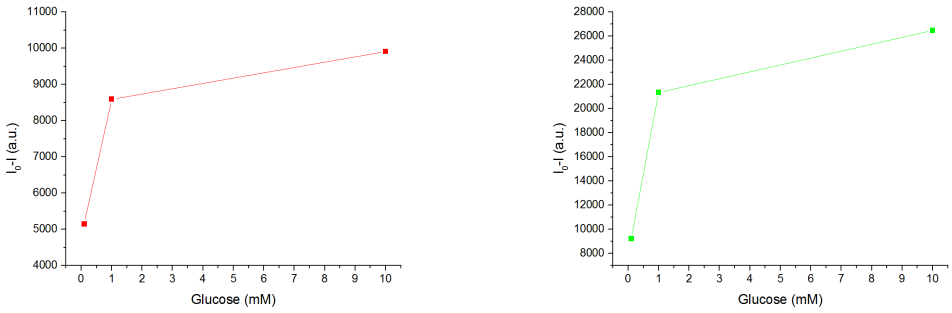

(a) Polymer coated QDs

(b) Micelle encapsulated QDs

Figure 6.21: Michaelis-Menten enzyme kinetics

6.5 Glucose sensing

A direct consequence of the studied phenomena is the possibility to build a glucose sensors using fluorescence quenching.

Normalized fluorescence quenching with glucose were calculated as a function of time as $(I_0(t) - I(t))/I_0(t)$ where $I(t)$ is the intensity measured at time t and $I_0(t)$ is the intensity of particles fluorescence in solution without glucose at time t. $I_0(t)$ was used instead of the initial fluorescence because with continuous measurments nano particles intensity decreases also for bleaching and not only for the desired quenching. In this way we tried to avoid the bleaching effect.

After comparing different samples quenching in Figure 6.22, we decided to calculate sensibility of solutions at time $t = 3000$ s, where QDs reach the maximum quenching.

Quenching of different nano particles at $t = 3000$ s are plotted in Fig.6.23.

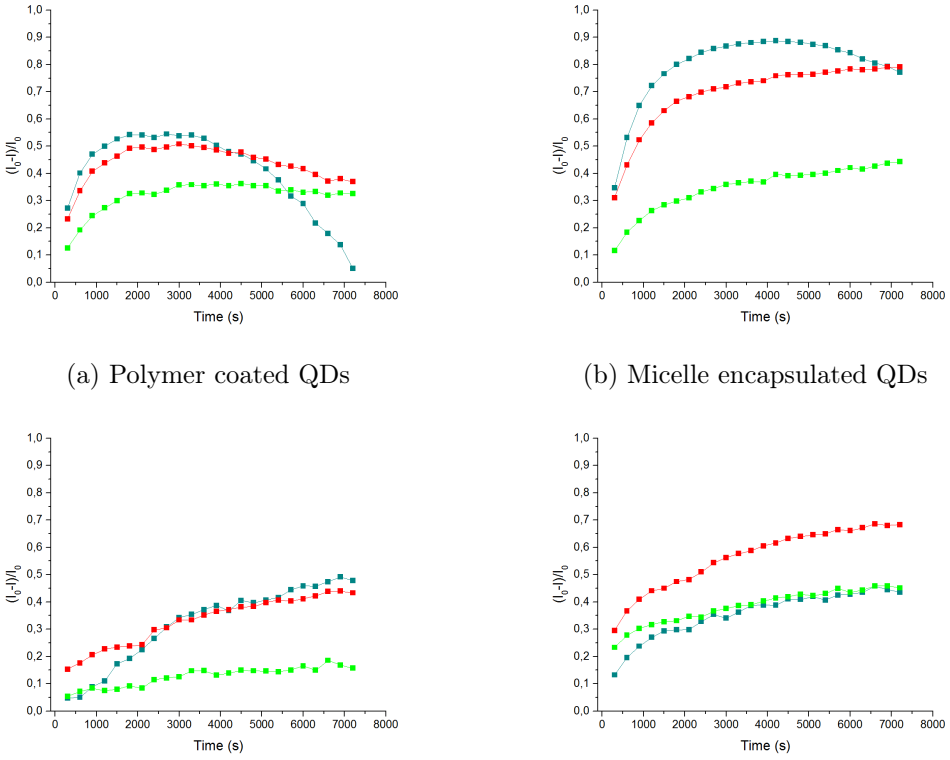

(a) Polymer coated QDs

(b) Micelle encapsulated QDs

(c) Polymer coated QRods

(d) Micelle encapsulated QRods

Figure 6.22: Relative intensity changing in time for conjugate in 10 mM (—■—), 1 mM (—■—) and 100μM (—■—) glucose solutions.

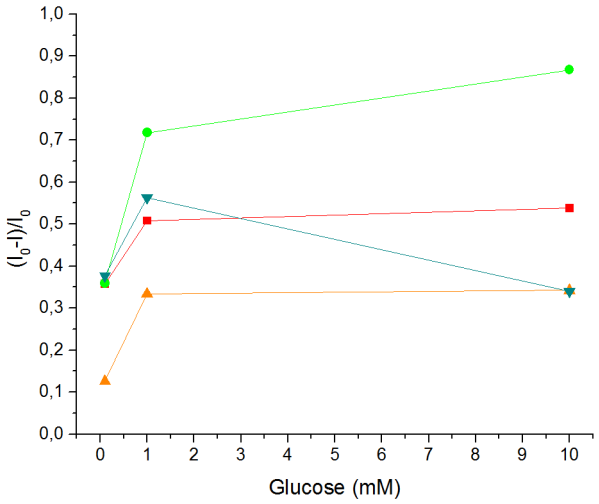

Figure 6.23: Relative intensity quenching after $t = 3000$ s for glucose concentrations. Legend: polymer coated QDs (—■—), micelle encapsulated QDs (—■—), polymer coated QRods (—■—) and micelle encapsulated QRods (—■—).

Table 6.3 shows the slope of the segment connecting two following point in Fig.6.23. The higher the value, the more accurate is the sensitivity of conjugated nanoparticles to glucose.

In general the sensitevity of all 4 systems is higher for glucose concentration <1 mM. The best in both ranges are micellized QDs.

Quantum dot-in-rods do not shows the expected behaviour (especially polymer coated), probably due to the higher sensitivity to external environment. Therefore these materials should not be used for sensing glucose in the mM range present in blood.

Range (mM)	QDs pol.coat.	QDs micell.	QRods pol.coat.	QRods micell.
0.1 - 1	0.167	0.398	0.231	.207
1 - 10	0.003	0.017	0.0009	-0.02

Table 6.3: Sensitivity of NPs solution to glucose in two glucose concentration ranges.

Conclusions and outlooks

This project was focused on how enzymes influence semiconductor NPs. Two main important results were achieved.

First, the multiple fluorescence peaks after the transfer of the CdSe/ZnS core/shell quantum dots into water were observed. The transfer protocol was supposed to give a high quantum yield (QY) to polymer coated QDs. On the contrary measured QY was really low (less than 1%). Generally, loss in emission efficiency of quantum dots is explained with the formation of trap sites thant relax through non-radiative pathways. Following this interpretation, the double peak in polymer coated QDs fluorescence that was observed in our measurements was completely unexpected. Our observation could instead be explained as an emission from trap states located at the boundary between core and shell, whiuch has previously been e observed in literature by Torchynska *et al.*

As a consequence of the presence of the trap sitesit was possible to observe emission from glucose oxidase attached on the surface. The observed fluorescence was greater than the one for isolated glucose oxidase at the same concentration, therefore new mechanisms of excitation are probably involved. One of these mechanisms could be energy transfer between quantum dots and enzymes' energy levels, which could be promoted by the thinness of the polymer coating. However, this interpretation is not completely clear, and it needs further investigations.

The second important result was achieved in the measurements of the enzyme effect on quantum dots. Quenching of hydrogen peroxide was proved. An explanation of the phenomena involving both conduction electrons and valence holes, not completely reported in literature yet, was proposed. Quantum dots do not only quenche luminescence due to hydrogen peroxide, but are also influenced by the external environment. Blueshift in emission and brightening of NPs was also observed. Blueshift was explained with the decrement of the size (through etching or oxidation) of the QDs core caused by the presence of acid and oxygen and by photooxidation. Photobrightening was supposed to have similar causes, in accordance with what was already reported in literature.

Since the NPs have a high surface-to-volume ratio, their interaction with the external environment is maximized, and this fact adds complexity to the already complicated behaviour of the NPs. Surfaces have lots of active sites and they are very reactive to unbound atoms. This fact makes the quantum dots extreamely useful, however it also increases their instability and gives rise to strange and not *a priori* understandable behaviour

One of the main outlooks of this research project is the possibility to build glucose sensors based on fluorescence quenching. A small comparison between quantum dots and dot-in-rods was performed, showing QDs good sensitivity in the glucose concen-

tration range 100 μM - 1 mM, while less sensitivity was found from 1 mM to 10 mM. A poorer sensitivity was found for dot-in-rods, due to the even higher surface-to-volume ratio and to the delocalization of the electrons in all the shell volumes. This facilitates the trap sites to capture the electrons and to inhibit the flourescence. In the presence of 1 mM and 10 mM glucose concentrations, conjugated quantum dot-in-rods fluorescence was strongly inhibited, with an unpredictable ongoing quenching in function of the glucose concentrations.

An increase in the enzymatic activity compared to free GOx was also found. This suggests means that enzymes work better on surfaces of quantum dots. Therefore it can be concluded that quantum dots-enzyme bio-conjugation is a good technique to build sensors to improve the analytic capability of enzymes and exploit the properties of synthetic nanostructures.

Bibliography

[1] Sergey V Gaponenko. *Introduction to nanophotonics*. Cambridge University Press, 2010.

[2] Charles Kittel. *Introduction to solid state physics*. Wiley, Hoboken NJ, 8th ed. edition, 2005.

[3] J.S. Blakemore. *Solid state physics*. Cambridge University Press, Cambridge, Great Britain, 2nd edition, 1985.

[4] O. Madelung. *Semiconductors: Data Handbook*. Data in science and technology. Springer Berlin Heidelberg, 2004.

[5] Louis E Brus. Electron-electron and electron-hole interactions in small semiconductor crystallites: The size dependence of the lowest excited electronic state. *The Journal of chemical physics*, 80(9):4403–4409, 1984.

[6] Yosuke Kayanuma. Quantum-size effects of interacting electrons and holes in semiconductor microcrystals with spherical shape. *Physical Review B*, 38(14):9797, 1988.

[7] HM Schmidt and H Weller. Quantum size effects in semiconductor crystallites: calculation of the energy spectrum for the confined exciton. *Chemical physics letters*, 129(6):615–618, 1986.

[8] Y Kayanuma. Wannier exciton in microcrystals. *Solid state communications*, 59(6):405–408, 1986.

[9] Andries Meijerink. *Exciton dynamics and energy transfer processes in semiconductor nanocrystals*. Springer, 2008.

[10] Brian L Wehrenberg, Congjun Wang, and Philippe Guyot-Sionnest. Interband and intraband optical studies of PbSe colloidal quantum dots. *The Journal of Physical Chemistry B*, 106(41):10634–10640, 2002.

[11] Mary D Archer and Arthur J Nozik. *Nanostructured and photoelectrochemical systems for solar photon conversion*. World Scientific, 2008.

[12] DJ Norris, A Sacra, CB Murray, and MG Bawendi. Measurement of the size dependent hole spectrum in CdSe quantum dots. *Physical review letters*, 72(16):2612, 1994.

[13] Christopher B Murray, CR Kagan, and MG Bawendi. Synthesis and characterization of monodisperse nanocrystals and close-packed nanocrystal assemblies. *Annual Review of Materials Science*, 30(1):545–610, 2000.

[14] AD Yoffe. Semiconductor quantum dots and related systems: electronic, optical, luminescence and related properties of low dimensional systems. *Advances in Physics*, 50(1):1–208, 2001.

[15] Andrew M Smith and Shuming Nie. Semiconductor nanocrystals: structure, properties, and band gap engineering. *Accounts of chemical research*, 43(2):190–200, 2009.

[16] BO Dabbousi, J Rodriguez-Viejo, Frederic V Mikulec, JR Heine, Hedi Mattoussi, R Ober, KF Jensen, and MG Bawendi. (CdSe) ZnS core-shell quantum dots: synthesis and characterization of a size series of highly luminescent nanocrystallites. *The Journal of Physical Chemistry B*, 101(46):9463–9475, 1997.

[17] Sungjee Kim, Brent Fisher, Hans-Jürgen Eisler, and Moungi Bawendi. Type-II quantum dots: CdTe/CdSe (core/shell) and CdSe/ZnTe (core/shell) heterostructures. *Journal of the American Chemical Society*, 125(38):11466–11467, 2003.

[18] Andrew M Smith, Hongwei Duan, Matthew N Rhyner, Gang Ruan, and Shuming Nie. A systematic examination of surface coatings on the optical and chemical properties of semiconductor quantum dots. *Physical Chemistry Chemical Physics*, 8(33):3895–3903, 2006.

[19] RA Sperling and WJ Parak. Surface modification, functionalization and bioconjugation of colloidal inorganic nanoparticles. *Philosophical Transactions of the Royal Society A: Mathematical, Physical and Engineering Sciences*, 368(1915):1333–1383, 2010.

[20] Rui-Kun Zhao, Andras Lukacs, Allison Haigney, Richard Brust, Gregory M Greetham, Michael Towrie, Peter J Tonge, and Stephen R Meech. Ultrafast transient mid IR to visible spectroscopy of fully reduced flavins. *Physical Chemistry Chemical Physics*, 13(39):17642–17648, 2011.

[21] Sandip B Bankar, Mahesh V Bule, Rekha S Singhal, and Laxmi Ananthanarayan. Glucose oxidase—an overview. *Biotechnology advances*, 27(4):489–501, 2009.

[22] Emma E Lees, Tich-Lam Nguyen, Andrew HA Clayton, and Paul Mulvaney. The preparation of colloidally stable, water-soluble, biocompatible, semiconductor nanocrystals with a small hydrodynamic diameter. *Acs Nano*, 3(5):1121–1128, 2009.

[23] Rui Hu, Wing-Cheung Law, Guimiao Lin, Ling Ye, Jianwei Liu, Jing Liu, Jessica L Reynolds, and Ken-Tye Yong. PEGylated phospholipid micelle-encapsulated near-infrared PbS quantum dots for in vitro and in vivo bioimaging. *Theranostics*, 2(7):723, 2012.

[24] S Sam, L Touahir, J Salvador Andresa, P Allongue, J-N Chazalviel, AC Gouget-Laemmel, C Henry de Villeneuve, A Moraillon, F Ozanam, N Gabouze, et al. Semiquantitative study of the EDC/NHS activation of acid terminal groups at modified porous silicon surfaces. *Langmuir*, 26(2):809–814, 2009.

[25] DJ Norris and MG Bawendi. Measurement and assignment of the size-dependent optical spectrum in CdSe quantum dots. *Physical Review B*, 53(24):16338, 1996.

[26] CA Leatherdale, W-K Woo, FV Mikulec, and MG Bawendi. On the absorption cross section of CdSe nanocrystal quantum dots. *The Journal of Physical Chemistry B*, 106(31):7619–7622, 2002.

[27] Xiaoming Wen, Amit Sitt, Pyng Yu, Yon-Rui Toh, and Jau Tang. Temperature dependent spectral properties of type-I and quasi type-II CdSe/CdS dot-in-rod nanocrystals. *Physical Chemistry Chemical Physics*, 14(10):3505–3512, 2012.

[28] Xiaoming Wen, Amit Sitt, Pyng Yu, Hsien-chen Ko, Yon-Rui Toh, and Jau Tang. Studies of the photostability of CdSe/CdS dot-in-rod nanoparticles. *Journal of Nanoparticle Research*, 14(12):1–13, 2012.

[29] Steven F Lee and Mark A Osborne. Brightening, blinking, bluing and bleaching in the life of a quantum dot: friend or foe? *ChemPhysChem*, 10(13):2174–2191, 2009.

[30] Pavel Frantsuzov, Masaru Kuno, Boldizsar Janko, and Rudolph A Marcus. Universal emission intermittency in quantum dots, nanorods and nanowires. *Nature Physics*, 4(7):519–522, 2008.

[31] T Torchynska and Yu Vorobiev. Semiconductor II-VI quantum dots with interface states and their biomedical applications. *Advanced Biomedical Engineering*, pages 143–183, 2011.

[32] LG Macotela, J Douda, TV Torchynska, R Peña Sierra, and L Shcherbyna. Transformation of photoluminescence spectra at the bioconjugation of core-shell CdSe/ZnS quantum dots. *physica status solidi (c)*, 7(3-4):724–727, 2010.

[33] Gabriele Rainò, Thilo Stöferle, Iwan Moreels, Raquel Gomes, John S Kamal, Zeger Hens, and Rainer F Mahrt. Probing the wave function delocalization in CdSe/CdS dot-in-rod nanocrystals by time-and temperature-resolved spectroscopy. *ACS nano*, 5(5):4031–4036, 2011.

[34] J Müller, JM Lupton, PG Lagoudakis, F Schindler, R Koeppe, AL Rogach, J Feldmann, DV Talapin, and H Weller. Wave function engineering in elongated semiconductor nanocrystals with heterogeneous carrier confinement. *Nano letters*, 5(10):2044–2049, 2005.

[35] J Müller, JM Lupton, AL Rogach, J Feldmann, DV Talapin, and H Weller. Monitoring surface charge movement in single elongated semiconductor nanocrystals. *Physical review letters*, 93(16):167402, 2004.

[36] Lihua Cao, Jian Ye, Lili Tong, and Bo Tang. A new route to the considerable enhancement of glucose oxidase (GOx) activity: the simple assembly of a complex from cdte quantum dots and gox, and its glucose sensing. *Chemistry-A European Journal*, 14(31):9633–9640, 2008.

[37] Peng Wu, Yu He, He-Fang Wang, and Xiu-Ping Yan. Conjugation of glucose oxidase onto Mn-doped ZnS quantum dots for phosphorescent sensing of glucose in biological fluids. *Analytical chemistry*, 82(4):1427–1433, 2010.

[38] Sara Cavaliere-Jaricot, Masih Darbandi, Erol Kucur, and Thomas Nann. Silica coated quantum dots: a new tool for electrochemical and optical glucose detection. *Microchimica Acta*, 160(3):375–383, 2008.

[39] Sergey K Poznyak, Dmitri V Talapin, Elena V Shevchenko, and Horst Weller. Quantum dot chemiluminescence. *Nano Letters*, 4(4):693–698, 2004.

[40] WGJHM van Sark, PLTM Frederix, DJ Van den Heuvel, AA Bol, JNJ van Lingen, C de Mello Donega, HC Gerritsen, and A Meijerink. Time-resolved fluorescence spectroscopy study on the photophysical behavior of quantum dots. *Journal of Fluorescence*, 12(1):69–76, 2002.

[41] Wilfried GJHM van Sark, Patrick LTM Frederix, Dave J Van den Heuvel, Hans C Gerritsen, Ageeth A Bol, Joost NJ van Lingen, Celso de Mello Donega, and Andries Meijerink. Photooxidation and photobleaching of single CdSe/ZnS quantum dots probed by room-temperature time-resolved spectroscopy. *The Journal of Physical Chemistry B*, 105(35):8281–8284, 2001.

[42] Wilfried GJHM van Sark, Patrick LTM Frederix, Ageeth A Bol, Hans C Gerritsen, and Andries Meijerink. Blueing, bleaching, and blinking of single CdSe/ZnS quantum dots. *ChemPhysChem*, 3(10):871–879, 2002.

[43] Marcus Jones, Jovan Nedeljkovic, Randy J Ellingson, Arthur J Nozik, and Garry Rumbles. Photoenhancement of luminescence in colloidal CdSe quantum dot solutions. *The Journal of Physical Chemistry B*, 107(41):11346–11352, 2003.

[44] Zhivko Zhelev, Rajan Jose, Toshimi Nagase, Hideki Ohba, Rumiana Bakalova, Mitsuru Ishikawa, and Yoshinobu Baba. Enhancement of the photoluminescence of CdSe quantum dots during long-term UV-irradiation: privilege or fault in life science research? *Journal of Photochemistry and Photobiology B: Biology*, 75(1):99–105, 2004.

[45] Noseung Myung, Yoonjung Bae, and Allen J Bard. Enhancement of the photoluminescence of CdSe nanocrystals dispersed in $CHCl_3$ by oxygen passivation of surface states. *Nano letters*, 3(6):747–749, 2003.

[46] Chin-Ping Huang, Shu-Wei Liu, Teng-Ming Chen, and Yaw-Kuen Li. A new approach for quantitative determination of glucose by using CdSe/ZnS quantum dots. *Sensors and Actuators B: Chemical*, 130(1):338–342, 2008.

[47] Xiaohu Gao, Warren CW Chan, and Shuming Nie. Quantum-dot nanocrystals for ultrasensitive biological labeling and multicolor optical encoding. *Journal of biomedical optics*, 7(4):532–537, 2002.

[48] Yu-San Liu, Yinghua Sun, P Thomas Vernier, Chi-Hui Liang, Suet Ying Christin Chong, and Martin A Gundersen. pH-sensitive photoluminescence of CdSe/ZnSe/ZnS quantum dots in human ovarian cancer cells. *The Journal of Physical Chemistry C*, 111(7):2872–2878, 2007.

[49] Nela Durisic, Antoine G Godin, Derrel Walters, Peter Gru tter, Paul W Wiseman, and Colin D Heyes. Probing the dark fraction of core-shell quantum dots by ensemble and single particle ph-dependent spectroscopy. *ACS nano*, 5(11):9062–9073, 2011.

[50] Dahai Yu, Zhi Wang, Yan Liu, Li Jin, Yueming Cheng, Jianguang Zhou, and Shugui Cao. Quantum dot-based pH probe for quick study of enzyme reaction kinetics. *Enzyme and microbial technology*, 41(1):127–132, 2007.

[51] Shan-Shan Yang, Cui-Ling Ren, Zhen-Yang Zhang, Jun-Jie Hao, Qin Hu, and Xing-Guo Chen. Aqueous synthesis of CdTe/CdSe core/shell quantum dots as pH-sensitive fluorescence probe for the determination of ascorbic acid. *Journal of fluorescence*, 21(3):1123–1129, 2011.

[52] César Maule, Helena Gonçalves, Conceição Mendonça, Paula Sampaio, Joaquim CG Esteves da Silva, and Pedro Jorge. Wavelength encoded analytical imaging and fiber optic sensing with pH sensitive CdTe quantum dots. *Talanta*, 80(5):1932–1938, 2010.

[53] Pratibha Pandey, Surinder P Singh, Sunil K Arya, Vinay Gupta, Monika Datta, Sukhvir Singh, and Bansi D Malhotra. Application of thiolated gold nanoparticles for the enhancement of glucose oxidase activity. *Langmuir*, 23(6):3333–3337, 2007.

[54] Jipei Yuan, Weiwei Guo, and Erkang Wang. Quantum dots–bienzyme hybrid system for the sensitive determination of glucose. *Biosensors and Bioelectronics*, 23(10):1567–1571, 2008.

[55] Ron Gill, Maya Zayats, and Itamar Willner. Semiconductor quantum dots for bioanalysis. *Angewandte Chemie International Edition*, 47(40):7602–7625, 2008.

[56] Wenjing Wang, Lei Bao, Jianping Lei, Wenwen Tu, and Huangxian Ju. Visible light induced photoelectrochemical biosensing based on oxygen-sensitive quantum dots. *Analytica chimica acta*, 744:33–38, 2012.

[57] Kwang-Soo Shin, Hong-Duk Youn, Young-Hoon Han, Sa-Ouk Kang, and Yung Chil Han. Purification and characterisation of D-glucose oxidase from white-rot fungus pleurotus ostreatus. *European journal of biochemistry*, 215(3):747–752, 1993.

[58] Peter Reiss, Myriam Protiere, and Liang Li. Core/shell semiconductor nanocrystals. *small*, 5(2):154–168, 2009.

[59] Xin Ji, Goutam Palui, Tommaso Avellini, Hyon Bin Na, Chongyue Yi, Kenneth L Knappenberger Jr, and Hedi Mattoussi. On the pH-dependent quenching of quantum dot photoluminescence by redox active dopamine. *Journal of the American Chemical Society*, 134(13):6006–6017, 2012.

[60] J Justin Gooding, Manihar Situmorang, Paul Erokhin, and D Brynn Hibbert. An assay for the determination of the amount of glucose oxidase immobilised in an enzyme electrode. *Analytical Communications*, 36(6):225–228, 1999.

[61] Wei Ma, Li-Xia Qin, Feng-Tao Liu, Zhen Gu, Jian Wang, Zhi Gang Pan, Tony D James, and Yi-Tao Long. Ubiquinone-quantum dot bioconjugates for in vitro and intracellular complex I sensing. *Scientific reports*, 3, 2013.

[62] Itamar Willner, Ronan Baron, and Bilha Willner. Integrated nanoparticle–biomolecule systems for biosensing and bioelectronics. *Biosensors and Bioelectronics*, 22(9):1841–1852, 2007.

[63] M Nirmal, CB Murray, and MG Bawendi. Fluorescence-line narrowing in CdSe quantum dots: Surface localization of the photogenerated exciton. *Physical Review B*, 50(4):2293, 1994.

[64] Hai-Yan Xie, Jian-Gong Liang, Zhi-Ling Zhang, Yi Liu, Zhi-Ke He, and Dai-Wen Pang. Luminescent CdSe-ZnS quantum dots as selective Cu^{2+} probe. *Spectrochimica Acta Part A: Molecular and Biomolecular Spectroscopy*, 60(11):2527–2530, 2004.